ION AND MOLECULE TRANSPORT IN NANOCHANNELS

by

Li-Jing Cheng

A dissertation submitted in partial fulfillment
of the requirements for the degree of
Doctor of Philosophy
Electrical Engineering and Computer Science
in The University of Michigan
2008

Doctoral Committee:

Associate Professor Lingjie Jay Guo, Chair
Associate Professor Alan J. Hunt
Associate Professor Katsuo Kurabayashi
Assistant Professor Michael Mayer

Table of Contents

List of Figures

List of Tables

Table of Appendices

Abstract

Transport of ions and molecules through nanochannels has been of interest due to the desire to understand the activity of biological ion channels and the prospect of exploiting the property in biomedical and chemical applications, such as molecular delivery and sensing. Nanochannels with critical dimensions comparable to Debye length exhibit surface charge-governed ion transport which is not accessible in microfluidic devices. To look into this unique phenomenon, we present our experimental and theoretical studies of the electrokinetic ion transport through sub-20 nm thick nanochannels.

First we demonstrated ion current rectification in homogeneous silica nanochannels with ion concentration gradients. We explained this effect in terms of the asymmetric electrostatic impact of the surface charges on the ions at the two ends of channel. Depending on the polarity of the applied electric field, the uneven ion flux from the two ends can accumulate or deplete the ions in the nanochannel and results in different and asymmetric ionic conductances. Based on theoretical calculations and a unified model we developed, we attribute the ionic rectification to the asymmetric cation-anion ratios at

two ends of channel. This original approach of understanding the role of the asymmetric cation-anion ratios provides an explicit, unified explanation about the function of the ionic rectification observed in a number of devices. Specifically it elucidates the essential physics for the similar rectification effects reported previously in conical nanopores and nanofluidic diodes. Prior to this unified model, the mechanisms of the ion rectifying effect in different nanofluidic devices were treated on the individual bases.

In addition, we developed heterogeneous nanofluidic devices for the control of ion flow with well-defined and robust surface charge distribution. By patterning alumina and silica thin film, we can produce positive and negative surface charges in the same nanochannel without conventional surface chemistry modification, providing a way to modify ion transport behavior. Nanofluidic diodes were successfully fabricated by this method and demonstrated rectifying factor greater than 300 which is the highest reported to date. The high rectification behavior may be implemented as a switching device for the control of ion flow. It was also found the different surface charge polarity inside and outside the nanochannel works as a parasitic diode and can affect ion transport. The experimental verification of the surface charge effect outside nanochannel provides a new view of the nanofluidics: the nano-/microchannel interface should be taken into account in interpreting the physics of ion transport in nanochannels.

Apart from electrostatic interaction with charged species, nanochannels possess steric confinement to molecules. We demonstrated a directional, active molecule transport by utilizing the kinesin motor proteins, which were selectively immobilized in the opened 350 nm wide nanochannels, to propel microtubules along the orientation of nanochannels. Due to the physical confinement of the nanochannel walls, microtubules can glide over a long distance without detaching from the surface. Functioning as a carrier, the microtubules can be chemically modified to carry and transport specific kinds of molecules and chemicals. This demonstration opens up the possibility of utilizing the biological molecules, i.e. motor protein and cytoskeletons, and artificial nanostructures to carry out several desired functions, e.g. chemical delivery or molecule concentration.

Chapter 1

Introduction

Transport of ions and molecules through nanoscale geometries has attracted broad interest in various fields. The interest stems from the pivotal role that transport phenomena through protein ion channels play in many physiological processes in living organisms.[1] Nanochannels and nanopores having dimensions comparable to the size of biomolecules such as proteins and DNAs have also started to be used in contemporary biotechnology since many separation[2,3] and sensing processes[4,5,6,7] requires pores with nanometer openings. α-hemolysin, one type of biological nanopores, for instance, has been demonstrated to provide single molecule sensitivity[8]. However, the drawback is that it is unstable and difficult to handle. On the contrary, artificial inorganic nanochannels fabricated by lithography on solid substrates are robust and provide more flexibility and precise control in terms of channel geometry. Moreover, by applying micro- / nano-fabrication technology, it is possible to integrate individual nanochannels into functional systems.

The characteristic height of the nanochannels considered here is about the Debye length (λ_D) for the ions. For the rest of the thesis, the nanochannel height is used interchangeably with the nanochannel size. Depending on the bulk ion concentration, n_b, the Debye length, λ_D, proportional to $n_b^{-1/2}$, ranges from few nanometers to few hundred nanometers. The transport phenomena studied in this thesis is in nanochannels with a height of about 20 nm or smaller at which the electric double layers (EDL) from the two channel surfaces are overlapped. It has been well known that surface charges induce electrostatic ion screening[9],[10] and electrokinetic effects, including electrophoresis and electroosmosis. In microfluidic devices, electroosmotic flow is studied and widely used to drive the fluid flow for pumping but not ionic current control. When the channel size is comparable to Debye length, the surface charge of nanochannel governs the polarity and concentration of ions inside the nanochannel and hence controls its ionic conductance. Unlike the electroosmotic flow in microfluidic channels, the surface charge in nanochannel plays a more important role in controlling the ion flows as opposed to the flow of fluid body[11,12.]

The objective of the thesis is to investigate the ion transport phenomena in nanochannel as well as to develop technologies to fabricate nanochannels in a controlled fashion capable of integration into conventional microfluidic channels. DC current-

potential measurements were performed to characterize the ion conductance of nanochannels. The influence of ion concentration and concentration gradient on the channel conductance was investigated. A nanofluidic diode was also demonstrated in heterogeneous nanochannels which were made of the combination of SiO_2 and Al_2O_3 The rectification phenomena may be useful for charged molecule separation.

1.1 Background of the electrostatic interaction in solid-fluid system

A solid surface will acquire a surface electric charge when brought into contact with aqueous media due to the ionized surface group or adsorbed ions. Due to electrostatic interaction, the charged surface in an electrolyte solution will influence the distribution of nearby ions in the solution.[13] Ions of opposite charge to that of the surface (counter-ions) are attracted to the surface while ions of like charge (co-ions) are repelled from the surface as illustrated in Figure 1.1. Combining with the mixing tendency resulting from the random thermal motion of ions, the attraction and repulsion leads to the formation of electric double layer (EDL). The EDL consists of a layer of immobile surface charge and a layer of mobile ions where an excess of counter-ions over co-ions exists to neutralize the surface charge. These ions can diffuse near the solid-liquid interface.

Several models have been introduced to describe EDL. The Helmholtz model describes the EDL as two charged layer separated by a fixed distance. The Gouy-Chapman model illustrates the EDL as a surface charge and a charged layer in the fluid in which the shielding ions are diffused, named diffuse double layer. Another classical model is Gouy-Chapman-Stern model which combine the previous two models. Apart from the shielding ions in the fluid, an inner layer called Stern layer is added in the model. This inner part of the EDL is introduced to take into account the finite size of ions which limits the thickness of the inner boundary of the diffuse part of the EDL since the center of an ion can only approach the surface to within its hydrated radius. As indicated in Fig 1-1, the potential at the Stern plane defined as the center plane of the Stern layer is close to the electrokinetic potential or the zeta potential at solid-liquid interface.

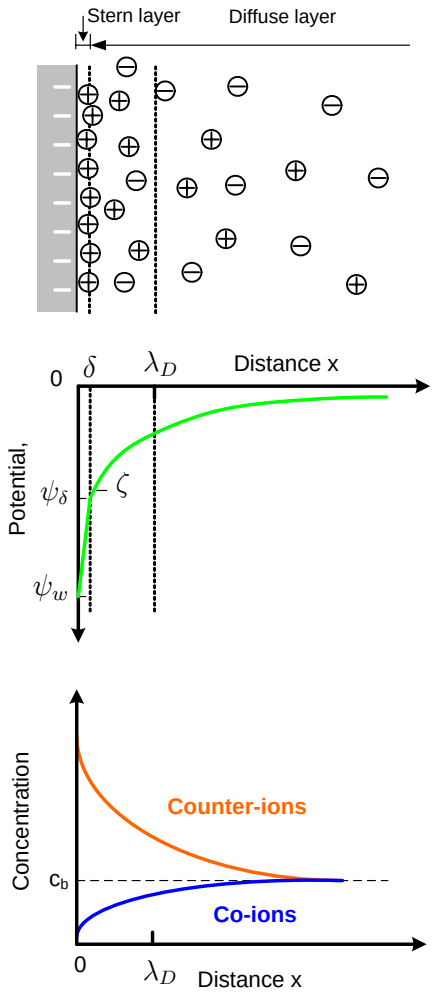

Figure 1.1 Structure of electric double layer

It may be observed that there would be only as many counter-ions in the EDL as needed to balance the charge on the solid surface if there were no thermal motion. In reality, however, because of the random thermal motion of ions at a given temperature and their energy distribution, there are ions that have enough thermal energy to overcome the electrostatic energy to escape from the EDL. Hence, the edge of the EDL is at the

position where the potential energy of the ions is about equal to the kinetic energy of the counter-ions, *i.e.* kT/2 for each degree of freedom. The definition of the edge leads to a characteristic distance known as Debye screening length, or in short, Debye length, $\lambda_{D,}$ which is expressed as, for a 1:1 electrolyte,

$$\lambda_D = \sqrt{\frac{\epsilon_0 \epsilon_r kT}{2z^2 qF c_b}} \tag{1.1}$$

For an aqueous solution of symmetric electrolyte (equal concentration of positive and negative ions) at 300K,

$$\lambda_D = \frac{9.61}{z\sqrt{c_b}} \tag{1.2}$$

with λ_D in nanometers and bulk concentration c_b in mM. For a univalent electrolyte the Debye length is about 10 nm for a concentration of 1mM and 1nm for 100mM. From (1.1) it can be seen that λ_D decreases inversely as the square root of the concentration. The Debye length depends solely on the properties of the liquid and not on any property of the surface such as its charge or potential.

1.2 Electrostatic interaction in nanochannels

Debye length typically ranges from 1 to 100 nm in aqueous solution depending on

the bulk ion concentration. At high bulk ion concentration, at which the Debye length, λ_D, is much smaller than channel size, h (Figure 1.2(a)), the ion concentration in nanochannel is the same as that outside in reservoirs. The electric potential remains zero in most part of the channel. On the contrary, at low bulk ion concentration at which $\lambda_D << h$, as depicted in Figure 1.2 (b) the electric potential inside the nanochannel is altered. Also, the counter-ions are accumulated while co-ions excluded from the channel resulting in a unipolar solution in the nanochannel. The average concentration is determined by the surface charge density, σ_s. In a slab-type nanochannel, where a nanochannel created between two charged surfaces separated by a distance h, the average ion concentration is simply given by $n_{ch}=2|\sigma_s|/(qh)$ derived from the requirement of electroneutrality. This indicates that the electrostatic effect arising form surface charge can influence throughout the channels having the size of about Debye length. Channel size aside, the surface charge density must be high enough to effectively control the ion concentration and the polarity in nanochannels and in turn affect its conductance. If the surface is negatively charged, the nanochannel will be rich in cations. On the contrary, positively charged surface will yield the accumulation of anions inside the channel. Such effect is not observed in microfluidic channel because of its smaller surface-to-volume ratio. Consequently, the effect of surface charge on the ionic composition and transport in

nanochannels leads to various unique phenomena that cannot be achieved in microfluidic channels.

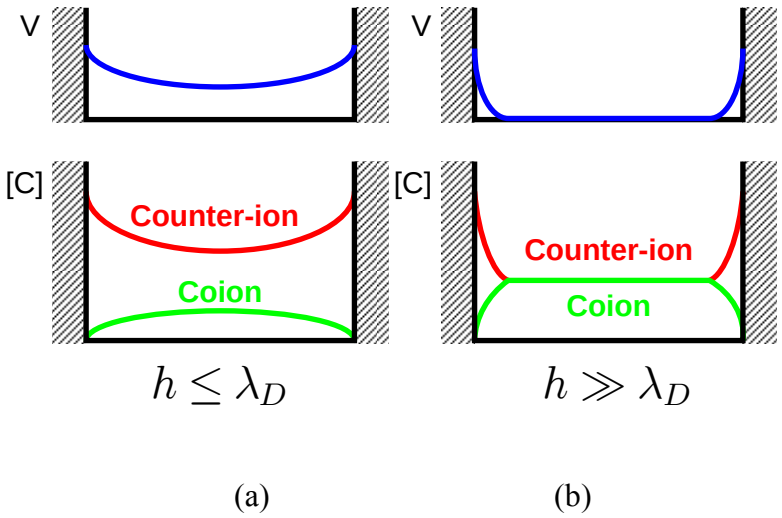

Figure 1.2 Surface charge effect on electric potential and ion concentrations in channels of different sizes. (a) In microchannel or at high ion concentration, h >> λ_D, the electric potential and ion concentration at the channel are not affected by surface charge. (b) In nanochannel or at low ion concentration, h << λ_D, surface charge raises the electric potential in the channel. The counter-ions are accumulated while co-ions, excluded.

1.3 Resemblance between nanofluidic devices and semiconductor devices

Reiss[14],Vijh[15] and Shockley[16] pointed out that electrons and holes in semiconductors have a strong similarity to the excess and deficiency of protons in water corresponding to acidic and basic solutions. Ions and electrons resemble each other in many ways. From the aspect of transport kinetics, both ions and electrons can be treated using the Drude

model which describes them in the context of kinetic theory for a neutral dilute gas and, hence, accounts for their Ohmic behaviors. Also, they both flow by diffusion and drift mechanisms. The Einstein relations can be applied to both the ions in a dilute electrolyte solution and the electrons in most of the materials except degenerately doped semiconductors because they obey Maxwell- Boltzmann statistics. Likewise, the Debye-Hückel theory can handle both in terms of the screening effect of the electric field from the individual charge particles. Additionally, the thermal generation of electrons and holes in a semiconductor is analogous to the thermal dissociation of water molecules, weak acid or base in an aqueous solution. From material point of view, it is known that electrons as majority carriers are found chiefly in an n-type semiconductor where they neutralize the positively charged donors, and holes are similarly found in p-type semiconductor. In nanochannels, the positively and negatively charged channel surfaces play similar roles as the donor and acceptor doping in n-type and p-type semiconductor materials, respectively. The nanochannels with negative surface charges have enhanced cations concentrations, while those containing positive surface charges have anions as majority charge carriers. When the two nanochannels with different surface charge polarities connect, the majority counter-ions from both sides diffuse across the junction and leave fixed surface charge behind. The exposed surface charges generate a Donnan

potential, which is equivalent to the built-in potential in semiconductor system. They describe the same physics--they are established so as to suppress the diffusion of mobile ions until equilibrium condition is reached. The ions at the nano-/micro-channel interface behave the same way at equilibrium. Such equilibrium characterized by an unequal distribution of diffusible ions between the two phases is specifically called Donnan Equilibrium.

While the semiconductor and nanofluidic systems share some similar attributes, they are also different in several aspects. First and foremost, majority of the cations and anions of interest do not recombine as electrons and holes do in semiconductors or even as proton and hydroxyl ions do in aqueous solutions. In addition, the mobilities of ions in solutions are very small (10^{-4} $cm^2/V{\cdot}s$) as compared to the corresponding values for electrons and holes (few hundreds or thousands $cm^2/V{\cdot}s$) in typical semiconductors. The doping level in semiconductor material is usually high enough and dopants completely ionized so that it is appropriate to assume equal concentrations of the fixed charge and the majority carriers, which could be several orders of magnitude greater than that of minority carrier. However, in nanochannels the fixed charges are located on the channel walls only; the concentration ratio of counter-ions to co-ion is not solely determined by the surface charge density on the channel walls. The geometry and the bulk concentration

of the solutions outside the nanochannels involve as well. On the other hand, these two factors can also provide alternative ways to create asymmetry in ionic flow and hence generate rectifying effects. This aspect will be discussed in more detail in this thesis.

Table 1.1 Comparison of ionic and electronic systems

	Ionic-nanofluidic devices	**Electronic-semiconductor devices**
Mobile charges	Cations, anions, H^+, OH^-	Electrons and holes
Recombination of charges	No (cation and anion) Yes (H^+ and OH^-)	Yes
Charge dissociation at equilibrium	$H_2O \leftrightarrow H^+ + OH^-$ $[H^+]\,[OH^-] = K_w$	Bond $\leftrightarrow e^- + h^+$ $n\,p = n_i^2$
Charge dissociation at non-equilibrium	Water splitting. E-field dependent (Second Wien effect)	e-h pair generation. E-field independent except breakdown
Charge distribution at low concentration	$n = n_b \exp(-zq(\phi-\phi_b)/kT)$ Boltzmann relation	$n = n_i \exp((E_F - E_i)/kT)$ $p = n_i \exp((E_i - E_F)/kT)$ Boltzmann relation
Charge distribution at high concentration	Modified Boltzmann distribution considering steric effect	Fermi-Dirac distribution
Charge diffusion length	Short (H^+ and OH^-)	Long
Charge mobility	$< 10^{-4}$ cm^2/Vs	Few hundreds to thousands cm^2/Vs
p-type material (majority carrier)	Negative surface charge-Cation nanochannel (Cation or H^+)	Acceptor-doped semiconductor (Hole)
n-type material (majority carrier)	Positive surface charge-Anion nanochannel (Anion or OH^-)	Donor-doped semiconductor (Electron)

1.4 Recent development in nanochannel devices

Since a membrane with nanopores is virtually an assemble of nanochannels, it is obvious that membrane science and nanofluidic science share common fundamental principles. While the conventional membrane science has been studied for decades, the recent advance in nanofabrication technology allows us to look into the transport phenomena in a single nanochannel with well-controlled geometry. Most of the nanochannels proposed or reported were either obtained directly from biological channel protein or artificially made by using track etching, inorganic tube synthesis or lithography. Following is the review of these technologies.

Biological nanopores

Kasianowicz et al.[4] in 1996 demonstrated the detection of DNA translocation through a protein channel, hemolysin pore, by monitoring the change of ionic current through the pore with the size of about 2.6 nm. As a DNA molecule passes through the small pore, it blocks the opening of the pore resulting in a transient decrease in the ion current through the pore. The technology shown in Figure 1.3 was then improved by Vercoutere et al.[8] who were able to sense DNA with single nucleotide resolution.

Artificial pores made by ion track etching

Nanoscale pores can also be drilled by high energy beams. Nishizawa et al.[9] used ion track etch to create the nanopores and shrink the pore size by gold plating. It was shown that the pore size can be precisely controlled by the gold plating time. Furthermore, they also demonstrated the capability of altering the potential on channel surface to let through only ions of desired polarity. (Figure 1.4) This field-effect fluidic channel is useful for separation of molecules with respect to their charges.

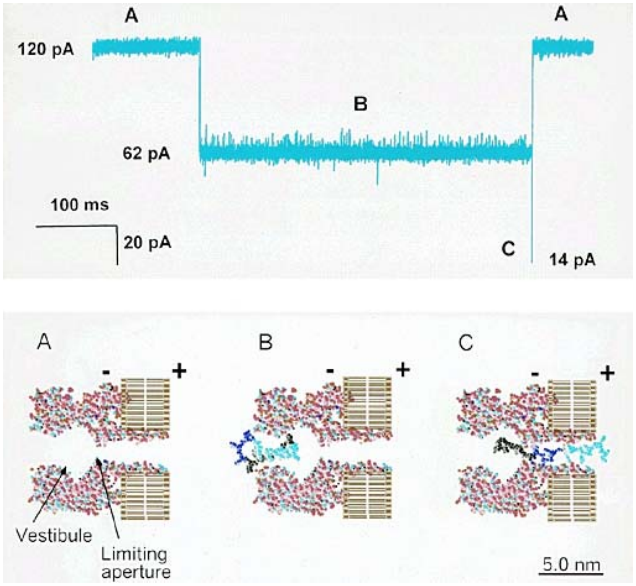

Figure 1.3 Detection of individual DNA haipin molecules at single nucleotide resolution. Upper panel shows a current trace caused by translocation of DNA hairpin through the α-hemolysin. The lower panel shows the molecular model of this event. Reproduced from Vercoutere et al.[8]

Nanochannels made by lithography and bonding

Plecis et al.[17] used lithography and wafer bonding technology to make nanoslits. As shown in Figure 1.5, the size of nanochannel was defined by a 50 nm thick gap between two glass substrates separated by an amorphous silicon layer. The nanoslit device connecting between two microchannels was used to study the diffusion of molecules.

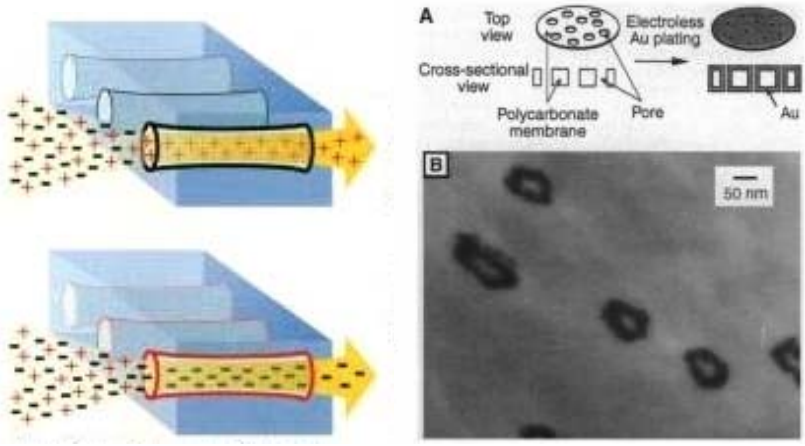

(a) (b)

Figure 1.4 A gold plated membrane or equivalently an array of nanochannels allows control of ion transport by applying electrical potential. (a) Illustrations show that with a negative potential, the membrane lets through only positive ions. With a positive potential, the situation is reversed. (b) SEM image of such membrane. The size of the pores on the membrane can be as small as few nanometers. Reproduced from Nishizawa et al.[9]

Nanochannel made of silica nanotubes

In Figure 1.6, a nanofluidic device made of single silica nanotube was proposed by Fan et al.[18] to perform transistor function. The silica nanotube was obtained by partially oxidize the silicon nanotubes produced by catalytic synthesis and removing the remaining silicon core by XeF_2 etching[19]. The inner diameter of the silica nanotube is about 40 to 50

nm.

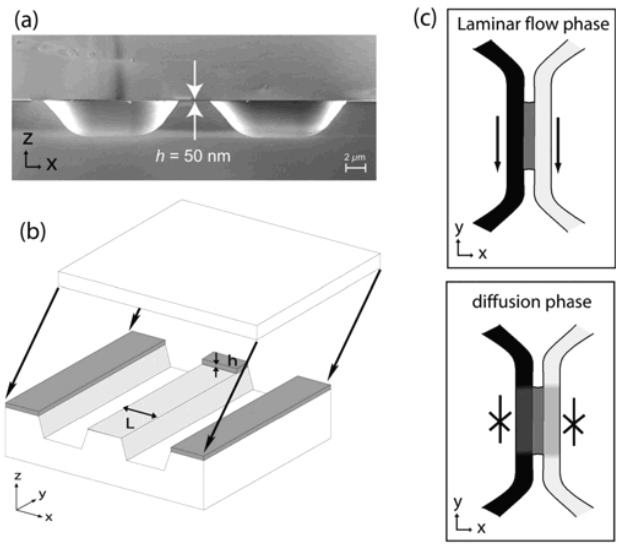

Figure 1.5 A nanoslit connecting between microchannels was fabricated by selective etching of a thin a-Si layer followed by anodic wafer bonding. The device was used to study diffusion of molecules in different pH environments. Produced from Plecis et al.[17]

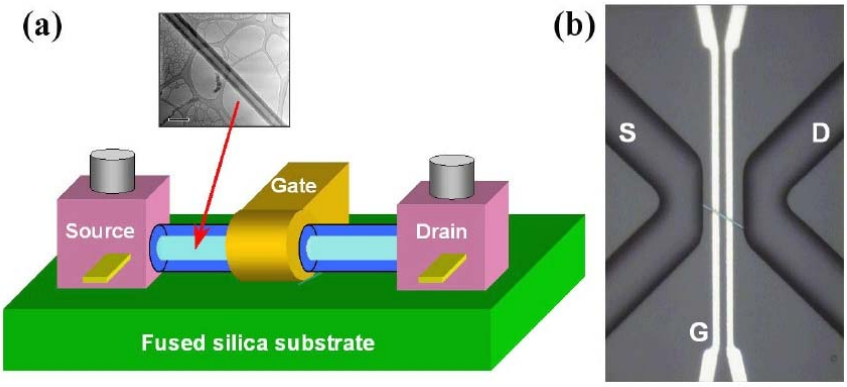

Figure 1.6 (a) Schematics of a single nanotube-based nanofluidic transistor. Inset is a TEM image of a silica nanotube. (b) An optical image of the device structure. Reproduced from Fan et al.[18]

1.5 Conclusion

The manipulation of fluids, ions or species in miniaturized channesl has the potential to influence areas from biological analysis to chemical synthesis. The small volume offers the advantages of short process time and reduced sample consumption. When the channel shrinks to the size of Debye length, new transport phenomena occur due stemming from the electrostatic interaction. Such new effect opens up the possibility of using electric field to control the flow of charged species or the fluid in the channel. In this work, the heterogeneous oxide surface nanochannels were developed to demonstrate the asymmetric ion current. The mechanism of nonlinear ion transport was investigated through experimental observation and theoretical calculation. Apart from the transport induced by electric field, we also demonstrated the active molecular transport by using motor proteins and nanoscale confinement. The combination of biological device and man-made device leads to a new concept in device integration as well.

The rest of the thesis is organized as follows. Chapter 2 presents the theoretical description and the experimental observation of surface-charge governed ion transport in nanochannels. Chapter 3 describes the heterogeneous nanochannels developed. Chapter 4 presents the ion rectifying effect in the nanofluidic diode fabricated by using

heterogeneous solid oxide material to produce different surface charge. The effect of bath side-wall surface charge on ion transport in heterogeneous nanochannels is delineated in chapter 5. Chapter 6 describes the active molecule transport by immobilized motor proteins. Finally, conclusion and future outlook are described in chapter 7.

REFERENCES

[1] Hille, B., *Ionic channels of Excitable Membranes*, 3nd ed., Sinauer Association, Sunderland, MA **2001**.

[2] Han, J.; Craighead, H. G., *Science* **2000,** 288, (5468), 1026-1029.

[3] Foquet, M.; Korlach, J.; Zipfel, W.; Webb, W. W.; Craighead, H. G., *Analytical Chemistry* **2002,** 74, (6), 1415-1422.

[4] Kasianowicz, J. J.; Brandin, E.; Branton, D.; Deamer, D. W., *Proceedings of the National Academy of Sciences of the United States of America* **1996,** 93, (24), 13770-13773.

[5] Li, J.; Stein, D.; McMullan, C.; Branton, D.; Aziz, M. J.; Golovchenko, J. A., *Nature* **2001,** 412, (6843), 166-169.

[6] Saleh, O. A.; Sohn, L. L., *Nano Letters* **2003,** 3, (1), 37-38.

[7] Chang, H.; Kosari, F.; Andreadakis, G.; Alam, M. A.; Vasmatzis, G.; Bashir, R., *Nano Letters* **2004,** 4, (8), 1551-1556.

[8] Vercoutere, W.; Winters-Hilt, S.; Olsen, H.; Deamer, D.; Haussler, D.; Akeson, M., *Nature Biotechnology* **2001,** 19, (3), 248-252.

[9] Nishizawa, M.; Menon, V. P.; Martin, C. R., *Science* **1995,** 268, (5211), 700-702.

[10] Martin, C. R.; Nishizawa, M.; Jirage, K.; Kang, M. S.; Lee, S. B., *Advanced Materials* **2001,** 13, (18), 1351-1362

[11] Stein, D.; Kruithof, M.; Dekker, C., *Physical Review Letters* **2004,** 93, (3), 4.

[12] Pu, Q. S.; Yun, J. S.; Temkin, H.; Liu, S. R., *Nano Letters* **2004,** 4, (6), 1099-1103.

[13] Israelachvili, J., *Intermolecular and surface forces*, 2nd ed.; Academic Press: London, **2003**.

[14] Reiss, H., *Journal of Chemical Physics* **1953,** 21, (7), 1209-1217

[15] Vijh, A. K., *Journal of Materials Science* **1975**, 10, (1), 123-135.

[16] Shockley W., Transistor technology evokes new physics, *Nobel Lecture*, Dec 11, **1956**. http://nobelprize.org/nobel_prizes/physics/laureates/1956/shockley-lecture.html

[17] Plecis, A.; Schoch, R. B.; Renaud, P., I. *Nano Letters* **2005,** 5, (6), 1147-1155.

[18] Fan, R.; Yue, M.; Karnik, R.; Majumdar, A.; Yang, P. D., *Physical Review Letters* **2005,** 95, (8), 4.

[19] Fan, R.; Wu, Y. Y.; Li, D. Y.; Yue, M.; Majumdar, A.; Yang, P. D., *Journal of the American Chemical Society* **2003,** 125, (18), 5254-5255.

Chapter 2

Homogeneous Nanochannels – Theory and Experiments

2.1 Introduction

In this chapter the surface charge-governed ion transport in nanochannels are studied through theory and experiments. The devices with about 20 nm channel size fabricated by standard microfabrication technology were characterized to observe the surface charge effect. The device we focused on in this chapter is a homogeneous nanochannel made of silica.

When the nanochannel is filled with an electrolyte solution, counter-ions pile up near the charged channel walls and co-ions excluded from the channel due to electrostatic interactions between the surface charges and the ions. Such nanochannel – electrolyte system can be analyzed by a combination of electrostatics, mass balance and momentum balance. There is considerable literature dealing with theoretical models to account for the effects of double layers on the transport of ions in long capillaries. Almost all of them are in the discipline of membrane science, soil science and colloid science. But

essentially the transport characteristics of membranes are given by the behavior of a single capillary or nanochannel. A membrane in those models is treated as a set of identical nanochannels. Therefore, the same model should also apply to analyzing ion transport in artificially fabricated nanochannels.

2.2 Theory of surface charge effect in nanochannels

The earliest and most complete publications were from Dresner[1] and from Gross[2] who assumed the Gouy-Chapman model for the EDL structure, the Nernst-Plank equation for ion fluxes and a modified Navier-Stokes equation for viscous flow of solutions. The assumption is made that the ions rigidly held inside Stern layer do not contribute to the ionic current. The Poisson equation accompanied with Nernst-Planck equation is general called Poisson-Nernst-Planck (PNP) equation. PNP theory is also widely used to deal with ion transport behavior in protein ion channel. These governing equations will be used to describe the transport behavior in nanochannel.

Figure 2.1 depicts the schematics of a nanofluidic device consisting of a nanochannel straddled by two reservoirs on either side. This corresponds to a typical experiment where an electrical potential is applied through a pair of Ag/AgCl electrodes connecting to the electrolyte solutions in the reservoirs. The governing

equations—Poisson equation (2.1), Nernst-Planck equation (2.2) and Navier-Stoke equation (2.3), are listed below:

$$-\nabla\epsilon_0\epsilon_r\nabla\psi = F\sum_i z_i c_i \tag{2.1}$$

$$\nabla\cdot(-D_i\nabla c_i - z_i\mu_i F c_i\nabla\psi) = -\mathbf{u}\nabla c_i \tag{2.2}$$

$$\begin{cases} \rho\left(\mathbf{u}\cdot\nabla\right)\mathbf{u} = -\nabla p + \eta\nabla^2\mathbf{u} - (\sum_i z_i F c_i)\nabla\psi \\ \nabla\cdot\mathbf{u} = 0 \end{cases} \tag{2.3}$$

where ψ is the electrostatic potential, c_i is the concentration of ion species i, p and **u** are the pressure and the velocity vector, respectively. The constants includes permittivity ($\varepsilon_0\varepsilon_r$), medium density ($\rho$), Faraday number (F), fluid viscosity (η) and valance number (z_i), diffusion coefficient (D_i), and mobility (μ_i) of ion species i. The calculation region is inside the channel and part of the reservoirs, *i.e.* the area enclosed by the dash line in Figure 2.1. The boundary conditions differ depending on the cases we study. In the case of ion conductance experiment, the boundary conditions at the channel walls, reservoir walls and the ends of reservoir are as follow:

At channel walls:

$$\hat{\mathbf{n}}\cdot\mathbf{D} = \sigma_s,\quad \hat{\mathbf{n}}\cdot(-D\nabla c_i - z_i\mu_i F c_i\nabla\psi) = 0,\quad \mathbf{u} = 0 \tag{2.4}$$

At reservoir walls:

$$\hat{\mathbf{n}}\cdot\mathbf{D} = 0,\quad \hat{\mathbf{n}}\cdot\nabla n_i = 0,\quad \hat{\mathbf{n}}\cdot\nabla p = 0 \tag{2.5}$$

At the ends of reservoirs:

$$\psi = \psi_b, \quad n_i = n_b, \quad p = p_b \tag{2.6}$$

where the subscript b denotes bulk and σ_s, surface charge density.

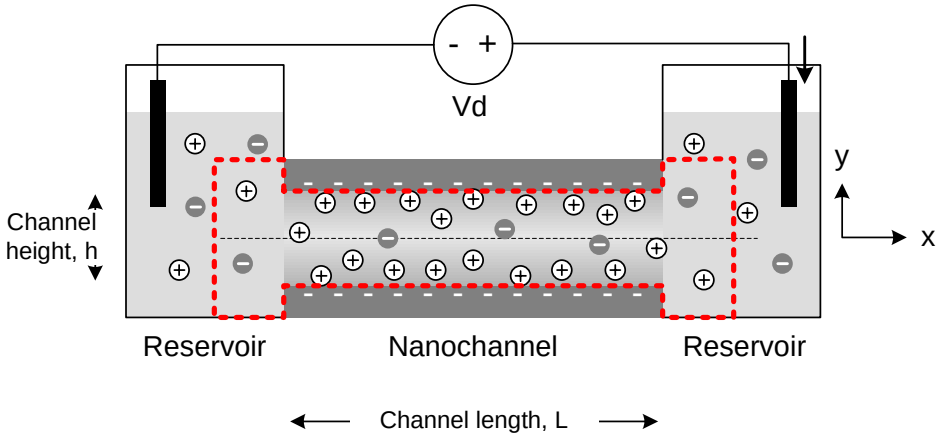

Figure 2.1 Schematic of a nanofluidic device consisting of a nanochannel and two reservoirs. The dash line encloses the region used in calculation.

When considering a nanochannel with high aspect ratio (L>>h, which agrees with the case of real nanochannels, *i.e.* 60 μm long, 3 μm wide and 20nm high), the electrical potential and ion distribution across the channel can be calculated by using PNP equation assuming no flow across y-direction of the nanochannel. The equations reduce to be a simple Poisson-Boltzmann (PB) equation

$$\frac{d^2\psi}{dy^2} = \frac{2zFc_b}{\epsilon_0\epsilon_r}\sinh\left(\frac{zF\psi}{RT}\right) \tag{2.7}$$

with boundary condition of $d\psi/dy = -\epsilon_0\epsilon_r\sigma_s$ at either side of channel walls (y = h/2 and y = -h/2). The resulting ion concentration profile can be used to calculate ionic

current. In nanochannels, only the current contributed by electrophoresis is considered while that by electroosmosis neglected. The simplification arises from the fact that when the channel height is comparable or smaller than the Debye length, the electrophoresis is dominant[3]. But if the surface charge increases, electroosmosis becomes more important although it is still smaller than electrophoresis. For this reason, the Navier-Stokes equation can be ignored.The calculated results give us some ideas about how the channel height h, ion concentration, c_b, and surface charge density, σ_s, affect the ion transport behavior in nanochannels. We now examine the effect of these three parameters:

Effect of channel height h

Consider the case that the surface charge density σ_s on the nanochannel wall is fixed to be -0.05 C/m^2 and the bulk ion concentration c_b= 1 mM, which yield a Debye length of about 10nm. As shown in the calculated results in Fig 3-2, when the channel size is large, the surface charge has no effect on the ions in the center of the channel, leaving electrical potential to zero. But when the two charged surfaces get closer, the electrostatic effect becomes more significant. The electrical potentials at the channel wall are identical for all cases since both ion concentration and surface charges are the same. The enhancement of counter- and the exclusion of co-ion appears when the channel size is about twice of

Debye length. The phenomena, summarized in Figure 2.3, by shrinking the channel size, it is possible to induce counter-ion concentration several order of magnitude higher than that outside the channel leaving a unipolar solution inside.

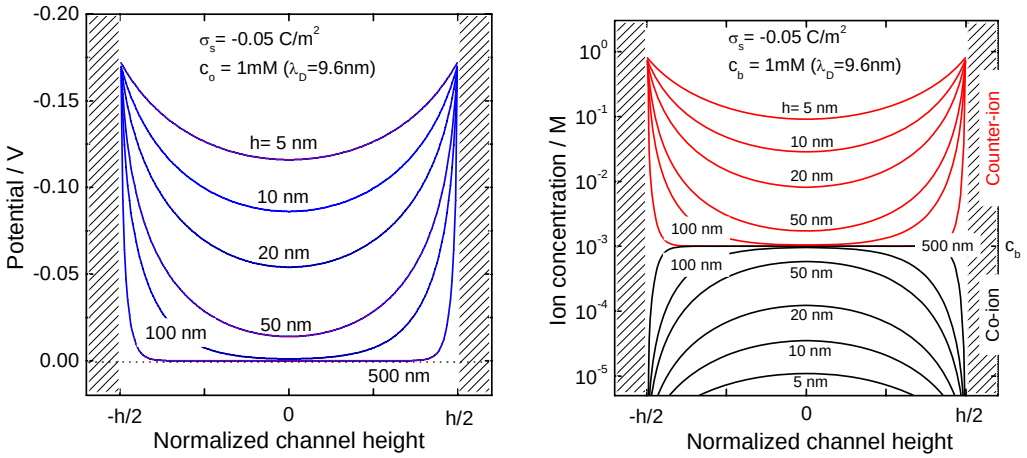

(a) (b)

Figure 2.2 (a) Calculated electrical potential profiles in a nanochannel with channel height ranging from 500nm to 5nm. The x-axis is the normalized channel height. (b) Ion concentration profiles across nanochannels of different sizes. The amount of counter-ions and co-ions becomes very different when λ_D is about or greater than h/2.

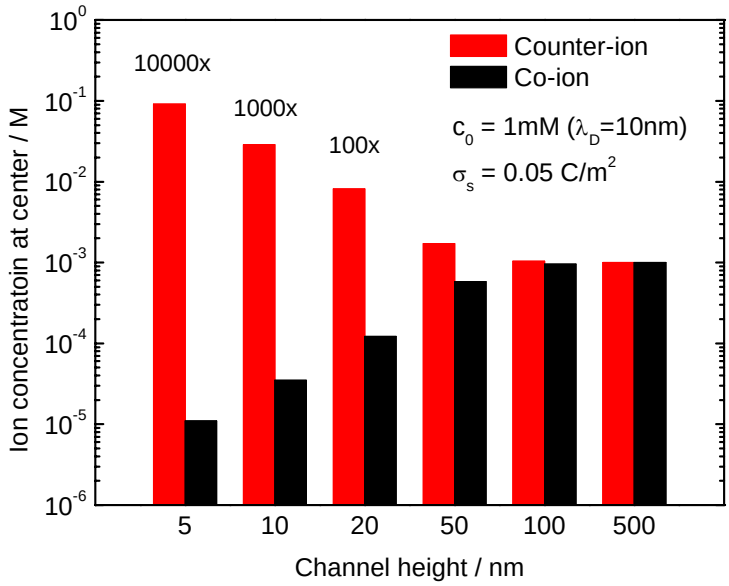

Figure 2.3 Comparison of the ion concentration in the channel of different size

Effect of bulk ion concentration c_b,

In this case, the surface charge density σ_s is still fixed to be -0.05C/m^2 and channel height h, 20 nm. From the calculated results, it can be seen that if the bulk ion concentration is higher the electrical potential is lower at walls and drops to zero in a short distance. The reason is that for higher concentration there are more ions available to effectively shield the charges on channel wall. The deficiency of ion at low concentration shows different behavior. The counter-ion is accumulated in the channel and keeps a certain concentration despite of the reduction in bulk concentration. Similar to the previous case, the effect comes out when the Debye length of the ion become greater than the channel size. As shown in Figure 2.4 (c) the counter-ion distribution profile holds even when the bulk

concentration is reduced to less than 1mM while the co-ions reduces steadily as they are repelled out of the nanochannel shown in Figure 2.4 (d).

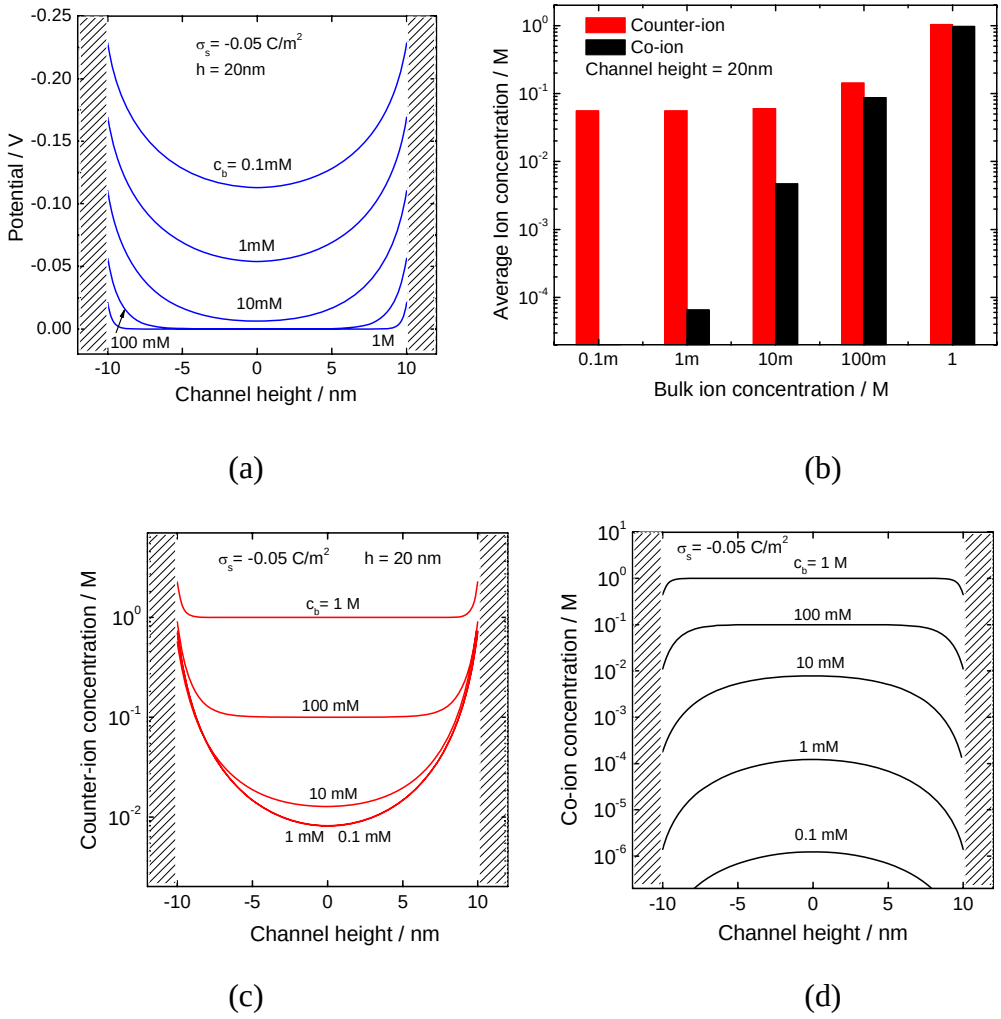

Figure 2.4 Electrical profiles (a) and ion distribution profiles, (c) and (d) for counter-ions and co-ions, respectively were calculated for different bulk ion concentration. The average ion concentration in nanochannel is summarized in (b).

Effect of surface charge density σ_s

All the unique behaviors of nanochannels stem from their surface charges. The surface

charge is contributed by the dissociation of chemical groups or the adsorption of ions. The surface charge can be altered by adjusting pH value of the solution or by applying electric bias. Here we consider the bulk ion concentration c_b = 1 mM and channel height h = 20 nm. It is proper to choose such size, since 20 nm is comparable to the Debye length (10nm) of a 1 mM KCl solution. As we can see in Figure 2.5, when the surface charge is increased the electrostatic potential also increases from zero due to the accumulation of positive counter-ions in the nanochannel. With higher surface charge density, both potential and concentration profile fall faster nearby the highly-charged wall and the Debye length, which indicates the 1/e decay distance for the potential, seems much shorter. This result does not contradict the basic knowledge that the Debye length depends only on balk ion concentrations, having nothing to do with surface charge density. However, it should be pointed out that the derivation of Debye length is based on Debye-Hückel approximation in which the small surface potential $\psi_w \ll RT/zF$ is assumed. Therefore, the quantity of the Debye length is no longer applicable to the case of high surface charge density. As summarized in Figure 2.6, the surface charge effect enhances the counter-ion concentration as well but it does not repel as much as co-ion as other effects mentioned previously do because the reduction of Debye length with increasing counter-ion concentration. Enhancement of counter-ions and exclusion of

co-ions are the key characteristics of nanochannels with charged surfaces. It is worthwhile to point out that the difference between the amount of those two ions in nanochannels should equal to $2\sigma_s/(qh)$ in equilibrium state to maintain electroneutrality.

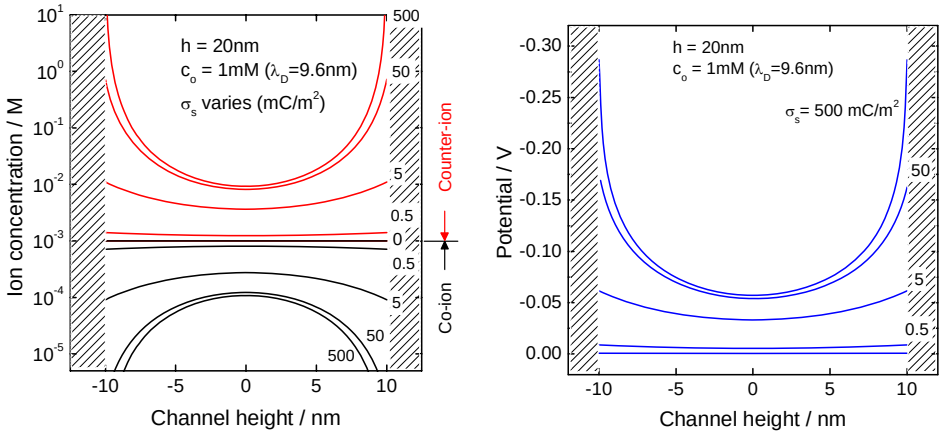

Figure 2.5 Electrical potential (a) and ion distribution (b) profiles for various surface charge densities.

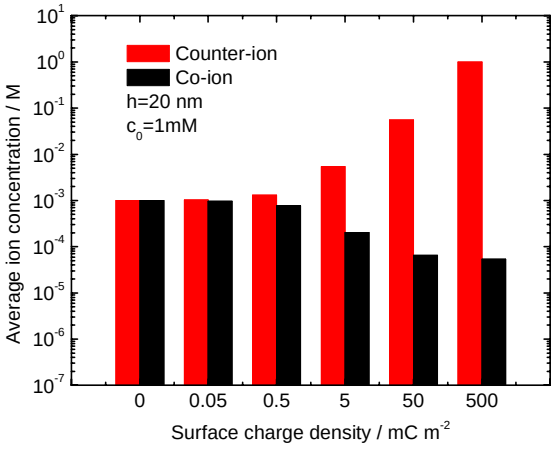

Figure 2.6 Summary of the relation between average ion concentrations and surface charge density in a 20 nm high nanochannel. The bulk ion concentration is 1 mM.

2.3 Fabrication of homogeneous silica nanochannels

The advances in microfabrication technology allow us to build microscale devices of diverse functions and to integrate many together on a same substrate. The down scaling of devices, to the exploitation of different physical phenomena and the capability of integration makes it possible to perform various functionalities on a single chip. It is also possible to fabricate microchannel networks, pumps and valves on one chip to function as a microfluidic system. It would be desirable to the do the same for nanofluidic channels. In this chapter, I will describe the fabrication technology developed to create nanofluidic devices and integrate them with microfluidic channels.

2.3.1 Fabrication of nanofluidic components

The first part of the device is nanofluidic channel. The nanochannels were fabricated on a 4-inch glass or oxidized silicon substrate. As shown in Figure 2.7, the process started with the deposition of a 20nm thick sacrificial layer (Cr or amorphous silicon) on the substrate by either evaporation (for Cr) or sputtering (for a-Si). The thickness of the sacrificial layer, easily controlled by the deposition time, will determine the height of the nanochannel. The sacrificial layer was then patterned by lithography and dry etching. Chromium was etched by Cl_2 reactive ion etching (RIE) (Cl_2 / O_2 gas flow = 20 / 8 sccm, pressure = 20 mTorr, power = 120W in a PlasmaTherm chamber) while silicon by SF_6

RIE (SF_6/Ar gas flow = 50 sccm / 10 sccm, pressure = 10 mTorr, DC power = 80 W, RF power = 500 W in Lam etch chamber). After photoresist was stripped, O_2 plasma (pressure = 250mTorr, power = 100W) was applied for 2 minutes to clean the sample. A 5 μm thick SiO_2 was then deposited on top to cap the sacrificial patterns by plasma-enhance chemical vapor deposition (PECVD) at 200 ^oC. Another lithography and RIE etch steps (C_2F_6 / Ar / He = 100 / 20 / 20 sccm, pressure = 10 mTorr, DC power = 100 W, RF power = 900 W in Lam etch chamber) were used to open the vias through the capped oxide and reach the sacrificial layer. The vias will be the interconnect between the nanochannels and the microchannels. After dicing, removing photoresist and oxygen plasma descum, the sacrificial layers were removed by wet etchant (CR-14 for Cr) or dry xenon difluoride (XeF_2) etch for a-Si. For XeF_2 etch, it was found necessary to treat the sample with high pressure C_2F_6 plasma beforehand to remove the native oxide formed on the exposed silicon surfaces during oxygen plasma treatment in order to obtain repeatable etch rate. After oxide etching, the sample was etched in Xectech for 30 minutes at 5 Torr XeF_2 in 120 sec-cycles. XeF_2 is a crystalline solid which sublimates at a pressure of 4.5 Torr at room temperature. The advantages of XeF_2 etching are fast etch rate and high selectivity with respect to oxide, photoresist and some metals, such as aluminum, chromium, nickel and noble metals. Such good etch selectivity is not observed in wet

etch process, and is essential in creating long but extremely thin nanochannels

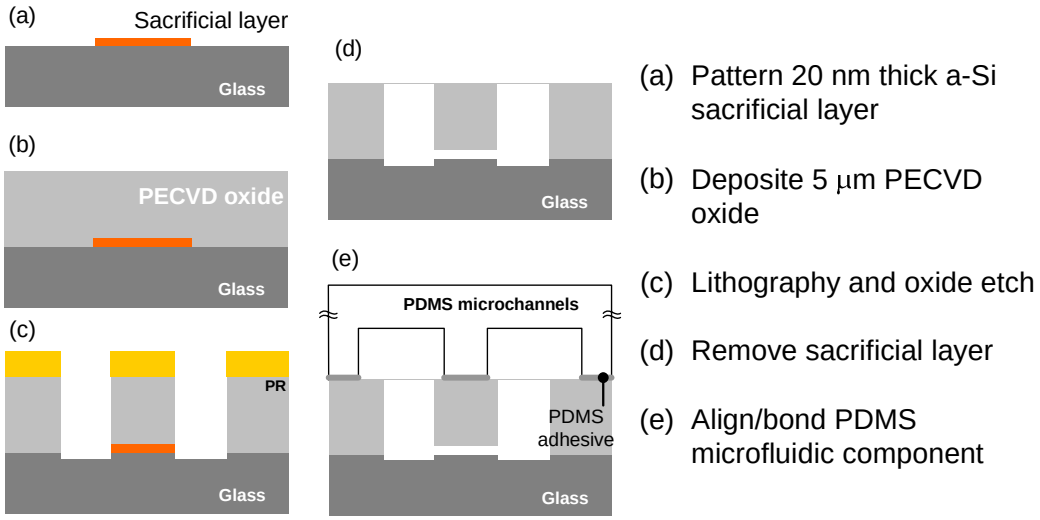

Figure 2.7 Fabrication sequence of a nanofluidic channel

2.3.2 Fabrication of microfluidic parts

The second part is a microfluidic chip which will be used to interface with nanofluidic channels. Microfluidic channels were made of poly-dimethyl siloxane (PDMS) elastomer a simple molding procedure. First, a hard mold for making the microchannels was formed by patterning a 30μm thick SU-8 photoresist on a silicon substrate using photolithography. To facilitate the demolding of cured PDMS, the hard mold was treated with a surfactant, perfluorodecyltrichlorosilane (Lancaster Synthesis, Windham, NH), after descumed in O_2 plasma to provide a low energy surface. To make a microfluidic structure, PDMS (Sylgard 184, Dow Corning) and curing agent mixture with the ratio of

10:1 were well-mixed and poured over the mold. After degased in a vacuum chamber, the sample was then cured at 65^{o}C for 4 hours. Finally, the PDMS microfluidic part was demolded. Several inlet holes were punched for tube connection in the experiment.

2.3.3 Assembly of nanofluidic and microfluidic parts

The glass nanofluidic channels and the PDMS microfluidic parts were assembled together by applying a newly developed alignment bonding process. To obtain better sealing, uncured PDMS was used serving as an adhesive layer between the nanofluidic and microfluidic interface. To make such a thin PDMS adhesive, a drop of PDMS-curing agent mixture (about 2 mL) was placed on a glass slide and spun at 7000 rpm for 1 minutes. The resulting PDMS thin film was scratched several times to make it even thinner. The reason to reduce its thickness is to avoid squeezing excessive PDMS out of the bonding surface which could possibly block the nanochannels. The PDMS microfluidic chip was then stamped on the adhesive thin film and lifted off, leading to a transfer of the uncured PDMS adhesive layer on the top surface of the chip. This microfluidic chip topped with adhesive was then aligned and bond on the nanofluidic chip to finish the final assembly. After bonding, the chips were treated with O_2 plasma and cured at 65 ^{o}C for 4 additional hours. The final step was to connect Tygon® tubings

and glass reservoirs to the chips. Figure 2.8 shows the final product of the nano-/micro-fluidic chip.

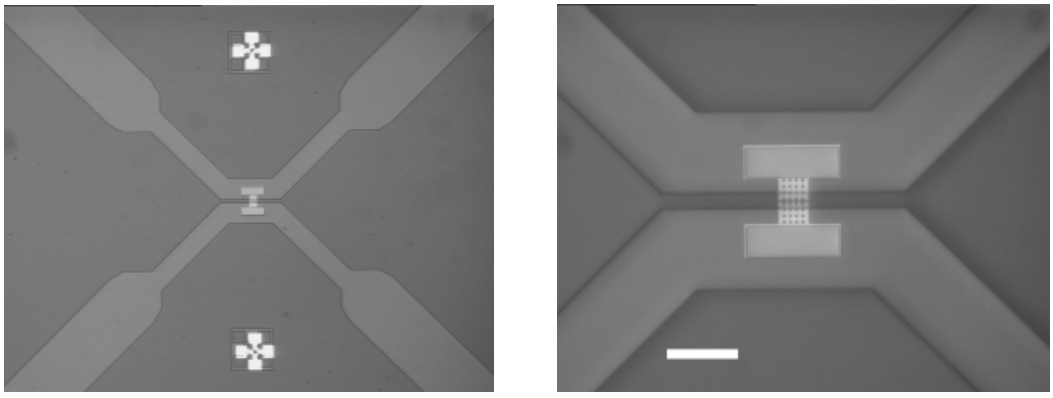

(a) (b)

Figure 2.8 An alignment-bonded chip. The scale bar in (b) is 100μm

2.4 Characterization of silica homogeneous nanochannels

Two nanofluidic devices fabricated by the method described above but with different channel heights were measured by using HP 4156 to obtain current-voltage characteristics. During the measurement, the devices under test were enclosed in a Faraday box to shield off electric noise from the ambient. The current resolution is 10 fA. The ionic solution is loaded from the two reservoir tubes and pumped into the microfluidic channel by peristaltic pump connecting on the other side through Tygon tubings. The aqueous solution was able to get into the nanochannel by capillary force. The microchannel was rinsed for 3 minutes before changing the solutions of different

ionic concentrations. In the electrochemical part, the electrodes connecting to ionic solution is a pair of home made Ag/AgCl electrodes. The electrodes were fabricated by applying a 2V bias on Ag electrode in a 0.1M KCl solution with reference to another counter electrode.

The DC ion conductance of the nanofluidic devices were measured by using HP 4156 Parameter Analyzer through a pair of Ag/AgCl electrodes The I-V curves were obtained by double scanning mode sweeping between -5 and 5 V with 500 mV step size and 3 sec delay time for each data point. We found that four seconds was sufficient for the devices under test to reach steady state. No pressure difference across the nanochannel was induced during the measurement.

The total channel conductance G can be expressed by a precise formula obtained by solving the PNP equation (2.1)-(2.3) coupled with Navier-Stokes equation (2.4),

$$G_{\mathrm{PNP}} = \frac{w}{L} F^2 c_b \int_{-h/2}^{h/2} \left(\mu_+ e^{-F\psi/RT} + \mu_- e^{F\psi/RT}\right) dy + \frac{w(\epsilon_0 \epsilon_r)^2}{L\eta} \int_{-h/2}^{h/2} \left(\frac{d\psi}{dy}\right)^2 dy \tag{2.8}$$

The first term is the conductance contributed by electrophoresis and the last term by electroosmosis. As mentioned before, in nanochannels the electroosmosis is usually much smaller and can be neglected. The potential ϕ, a function of position y, in (2.8) can be

obtained from Poisson-Boltzmann equation.

Because in nanochannels the fluidic flow is comparably small and is negligible, most of the current is contributed by ion migrations. Because the electroneutrality is assumed to preserve in the nanochannel, the conductance of nanochannel can be simplified to

$$G = q(\mu_K + \mu_{Cl})n_b\frac{wh}{L} + 2\mu_K\sigma_s\frac{w}{L} \tag{2.9}$$

where μ, n_b, σ_s are the ion mobility, bulk ion concentration and channel surface charge density, respectively; while w, h and L are the channel width, height and length; n_b is the ion density (m^{-3}) which is related to concentration c_b (M) by $n_b = c_b\ 10^3$ Na, where Na is Avogadro's number. The channel geometry, w and L can be well defined in the microfabrication process and quantified by optical microscopy. In equation (2.9) the first term of the conductance is due to bath ion concentration while the second term is contributed by the ions induced by the channel surfaced charge. At high c_b ($c_b > \sigma_s/(h\ q\ Na)$), the surface charges in nanochannel are shielded by the mobile ions and have negligible influence on ion concentration in the nanochannel. Hence, the ion conductance in the nanochannel is determined by bath concentration. On the contrary, at low concentration i.e. $c_b < \sigma_s/(h\ q\ Na)$, surface charge governs the ion concentration inside the nanochannel no matter how low the bath concentration is. Therefore, the ion conductance

is controlled by surface charge density.

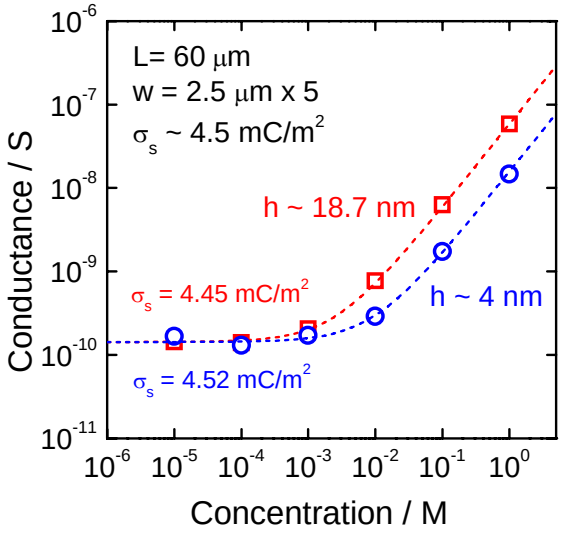

Figure 2.9 Measured ionic conductance of two nanochannel devices filled with different concentrations of KCl solutions. The experimental results match that from the theoretical calculation (dash lines). The channel heights are estimated to be 4 nm and 18.7 nm for these two devices.

Figure 2.9 presents the measured ionic conductance of two nanochannels at different KCl concentrations c_b (M). The experimental results conform to the theoretical calculation. Knowing the lithographically defined channel width w (=12.5 μm) and length L (= 60 μm), and mobilities of K and Cl ions, μ_K (= 7.619×10^{-8} $m^2/V\ s$) and μ_{Cl} (= 7.912×10^{-8} $m^2/V\ s$) both channel height h (m) and surface charge density σ_s (C/m^2) can be obtained by fitting the experimental data with the equation (2.9). The channel heights for the devices prepared by using two different sacrificial layer thicknesses were estimated to

be ~ 18.7 nm and 4 nm high, respectively, and their surface charge densities were about 4.5 mC/m^2.

As explained previously, a saturation of conductance is observed when the KCl concentration is less than a critical value, i.e. $c_b < \sigma_s/(h\ q\ Na)$, at which bath concentration c_b is lower than the fixed charge density in the nanochannel. In this regime the electric double layer (EDL) is comparable to one half of the channel height. In this case, for a 20 nm high nanochannel, the critical concentration is about 0.9 mM. In this region, the counter ion, K+ ion, concentration is enhanced to maintain the electroneutrality shielding the surface charge on channel walls. The channel conductance, hence, is determined by the surface charge in nanochannel. When the concentration exceeds this point, the channel conductance increases linearly with bath concentration. Because the two channels were made of the same material, they exhibit similar surface charge densities. The results also imply that in the surface charge governed regime, the size of the nanochannel does not affect the ion conductance.

2.5 Conclusion

In this chapter, we present the theory of electrokinetic transport in nanochannels.

The theory suggests that the ion conductance of nanochannel at low concentrations is governed by the surface charge inside nanochannels rather than their geometry and bath ion concentrations. The surface charge governed ion conduction effect was observed experimentally by measuring the conductance of two silica nanochannels with different channel height. The surface charge of the silica surface was estimated to be about 4.5 mC/m^2. In the next chapter, we will study how the surface charges in nanochannels affect the ion transport through ion concentration gradients.

REFERENCES

[1] Dresner, L., Electrokinetic phenomena in charged microcapillaries. *Journal of Physical Chemistry* **1963,** 67, (8), 1635-&.

[2] Gross, R. J.; Osterle, J. F., Membrane transport characteristics of ultrafine capillaries. *Journal of Chemical Physics* **1968,** 49, (1), 228-&.

[3] Daiguji, H.; Yang, P. D.; Majumdar, A., Ion transport in nanofluidic channels. *Nano Letters* **2004,** 4, (1), 137-142

Chapter 3

Ion Transport in Homogeneous Nanochannels with Concentration Gradients

3.1 Introduction

Transport of ions through nanoscale geometries has been widely studied due to the desire and interest to understand the activity of biological ion channels in physiological processes and the prospect of exploiting the property in biomedical and chemical applications, such as molecule delivery and sensing.[1] Fabricated on solid substrates, artificial nanochannels or nanopores provide robust and controllable means for more versatile applications[2, 3, 4] and can be easily integrated with microfluidic devices. The general benefit of small channel size is the capability of handling attoliter-scale samples, resulting in minimal usage of reagent, precise quantity control and efficient process. In addition to these benefits, nanochannels with proper channel size and reservoir bath concentrations offer selectivity to charged ions and molecules. The charge selectivity in such devices derives from the fact that when the size of nanochannels is reduced to or

smaller than the Debye length, λ_D, [5] the concentration of the counter-ions in nanochannels can be enhanced while that of co-ions diminished due to the electrostatic interaction between ions and charged channel walls.[6] In this regime, the electric-double layers (EDL) overlap and the ion conductance through the nanochannel is governed by the surface charge instead of the bath ion concentration in the reservoirs. Such unique properties open up the possibility to selectively deliver specific types and controllable amounts of molecules or ions through the nanochannels by electrokinetic transport.

Nanochannels serving as chemical delivery devices are usually placed between two ionic solutions of different concentrations.[2, 7] Flow of ions though the nanochannel in such circumstance was observed to occur more readily in one direction than in the other. Similar asymmetric effect has been observed in conical-shaped nanopores which have asymmetric channel geometry[8] and diode-like nanochannels with asymmetric surface charge distributions. [9, 10] In this chapter, we experimentally study the asymmetric ionic flux in structurally symmetric silica nanochannels with homogeneous surface charge density but placed between the asymmetric ion concentrations. We attribute the rectifying effect to the disparate ion concentration profiles produced under the applied potentials of different polarities. As illustrated in Figure 3.1, voltage bias of different polarities applied across a nanochannel, along with the concentration gradient in the channel can extend or

shrink the proportion of EDL overlap in the nanochannel and, therefore, cause the asymmetric ionic conductance. Theoretical calculation by using 2-dimensional Poisson-Nernst-Planck (PNP) model agrees qualitatively with the experimental results. We also provide a simplified analysis to elucidate the common mechanism that applies to all of the ionic rectifying effects reported to date. The purpose of this work is to demonstrate and analyze one of the fundamental issues encountered in the design of nanofluidic devices.

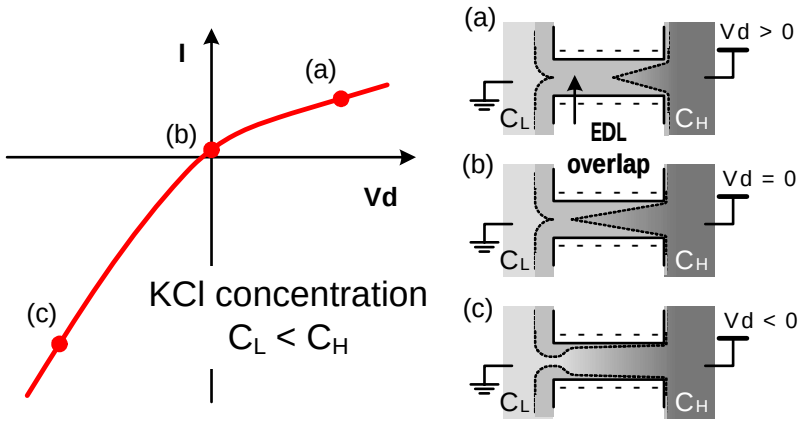

Figure 3.1 Rectifying effect due to the disparate ion distribution along the nanochannel having negative surface charge and under different polarities of applied potential. The gray scale plots show the relative ionic concentration in different regions of the channel. (a) High concentration C_H side is positively biased relative to the low concentration side C_L. (b) Zero bias. (c) C_H is negatively biased. The gray region within the nanochannel that is bound by the dashed lines represents the electric double layers (EDL).

3.2 Characterization of nanochannels with concentration gradients

3.2.1 Fabrication of nanochannel

In our experiment, two different sizes of nanochannel were studied. They are both 60 μm long and equivalently 12.5 μm wide by design and fabrication. The thicknesses of the two nanochannels, determined by the experiment, are ~19 nm and ~4 nm respectively. Figure 3.2 shows the microscopic images of the device. The 20-nm thick nanochannels were fabricated by removing a 20-nm thick sputtered a-Si sacrificial layer by gaseous XeF_2. The channel thickness, however, can be reduced further if Cr sacrificial layers and a wet-etch process was applied. After etching away the 20nm-thick Cr sacrificial layer, DI rinsing and drying the structure, the nanochannels collapsed due to capillary force. Because the e-beam evaporated Cr layer has relatively rough surface, instead of pinching completely the nanochannels shrank in the vertical dimension and left a small gap between top and bottom silica surfaces. This provides an opportunity to produce nanochannels with exceedingly small channel height that is very difficult to create otherwise. The nanochannels made by Si sacrificial layer do not collapse during the dry process but the channels do pinch if they are filled with water and then dried out. However, it was found that the residual gap could not be obtained as the device made by

Cr sacrificial layer does. This is because the channel made from sputtered a-Si sacrificial layers has relatively smooth surfaces. The channels sealed completely after they dried out.

3.2.2 Characterization of homogeneous nanochannel

By measuring the current-voltage (I-V) characteristics of the nanochannels and fitting the experimental ion conductance at varied KCl concentrations, the thicknesses of the two nanochannels were extracted to be ca. 18.7 nm and 4 nm, respectively (see previous chapter).[11] Their surface charge densities were very close and were about 4.5 mC/m^2. The extracted surface charge density is in the range of the reported data on silica surface[12] but lower than those acquired in the prior works.[6,11,13] The discrepancy may result from the different oxide materials that are produced by different processes. Apart from the surface charge, it is worth emphasizing that the predicted height of the thin channel, 4 nm, is calculated by using the ion mobilities in the bulk.[14] The real ion mobilities can be lower in sub-5nm geometry due to the fixed charge and the ion proximity to the channel walls.[15] If the reduction of ion mobilities is considered, we should obtain a higher surface charge density as well as a channel height greater than 4 nm.

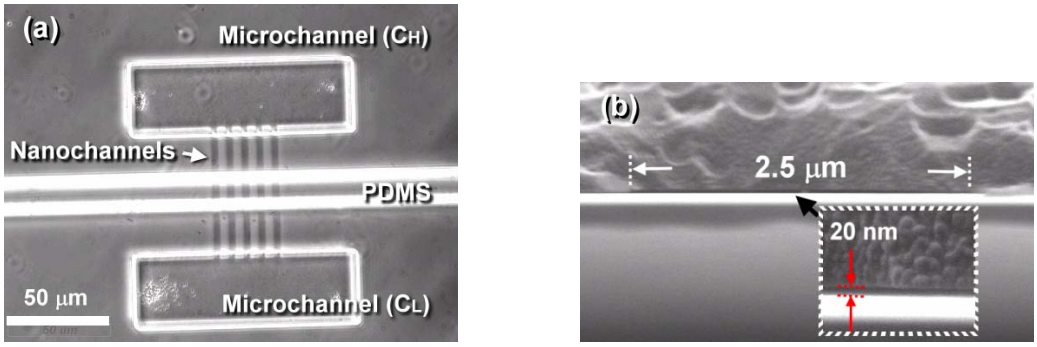

Figure 3.2 (a) Phase-contrast microscopic top-view image of the device. Five 60 μm-long nanochannels connect between two microfluidic channels. The two rectangles are the contact holes connecting the nanochannels and microchannels. The transparent bar lying across the nanochannels is a PDMS wall separating two microchannels. (b) Cross-section SEM image shows that each nanochannel is 2.5 μm wide and ~ 20 nm thick. The bright line in the SEM is the bottom surface extending out of the nanochannel.

3.2.3 Characterization of homogeneous nanochannel with concentration gradients

Three regimes in I-V characteristics were observed when the nanochannel connects between different bath concentrations: one side with lower concentration was termed C_L, and was fixed at 0.1 mM while the other side with high concentration was termed C_H, and varied from 0.1 mM to 1 M. The three regimes are symmetric regime (i.e. ohmic behavior), rectifying regime, and weakened rectifying regime. The I-V characteristics corresponding to different C_H and with fixed C_L = 0.1 mM are plotted in Figure 3.3(I.a-e) and 3(II.a-e). The zero-current potentials in the I-V curves were mostly due to the offset electrode potentials which were produced by the unequal voltage drops at the

electrode-electrolyte interface in different electrolyte concentrations (see 3.2.5). The forward-bias conductance, reverse-bias conductance, and the rectifying factor I_F/I_R, are summarized in Figure 3.3(I.f) and 3(II.f). I_F and I_R were the currents measured at -5 V and 5 V, respectively. In the symmetric regime, when C_H is lower than 10 mM (for 4-nm channel) or 1 mM (for 20-nm channel), both I_F and I_R are almost identical and the nanochannels showed the anticipated ohmic behavior in conducting ionic currents. Although the reservoir concentration is asymmetric, the current level is comparable to the results obtained in the case of symmetric concentration (i.e. $C_L = C_H = 0.1$ mM). In the second regime, the current becomes asymmetric with respect to forward and reverse voltage bias. As shown in Figure 3.3(I.f) and 3(II.f), the rectifying effect is maximized at $C_H = 0.1$ M with $I_F/I_R \sim 3.5$. However, in the third regime when the C_H was increased to 1 M, both I_F and I_R increased yielding weaker asymmetric I-V characteristics. In comparison, the rectifying behavior cannot be observed in microfluidic channels.

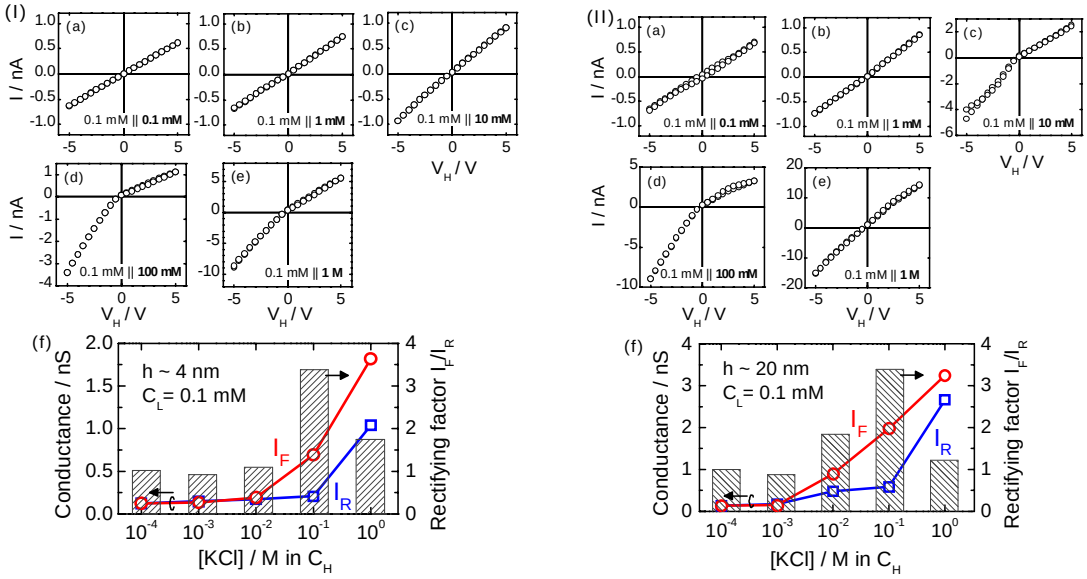

Figure 3.3 The measured I-V characteristics of 4-nm thick nanochannels (I-a to e), and 20-nm thick nanochannels (II-a to e) under various asymmetric concentrations ($C_L||C_H$). The forward-biased and reverse-biased conductances and the rectifying factor I_F/I_R are summarized in (I-f) and (II-f) for 4-nm and 20-nm thick nanochannel, respectively. The concentration in left side (C_L) is fixed at 0.1 mM while the right side (C_H) varies from 0.1 mM to 1 M. The channel width is 2.5 μm × 5 and length, 60 μm.

3.2.4 Ion rectification in homogeneous nanochannel with concentration gradients

The asymmetric ion conduction behaviors under different concentration gradients were qualitatively investigated by calculating the ion distribution profiles in the nanochannel using 2-dimensional Poisson-Nernst-Planck (PNP) and continuity equations. [16] Electroneutrality is maintained in the entire system. Because the phenomenon takes place under an applied potential, it represents a nonequilibrium

problem. With the channel length much longer than the Debye length, the phenomena cannot be explained with the approximation of constant-field and constant-concentration gradient.[17] The system used for simulation is a 10 μm long, 20 nm thick nanochannel straddled by two 2 μm size square reservoirs. The length of 10 μm which is shorter than the real device was used to reduce simulation time. The surface charge density on the channel walls is assumed 3.5 mC/m^2 which corresponds to the experimental data. Boundary conditions are set such that the bulk concentration and potential for each reservoir are located 2 μm away from the entrances of the nanochannel. The concentration and potential of the left boundary are fixed to 0.1 mM and 0 V, respectively. The calculated electric potential and profiles of ion concentration averaged across the thickness of the nanochannel are plotted in Figure 3.4.

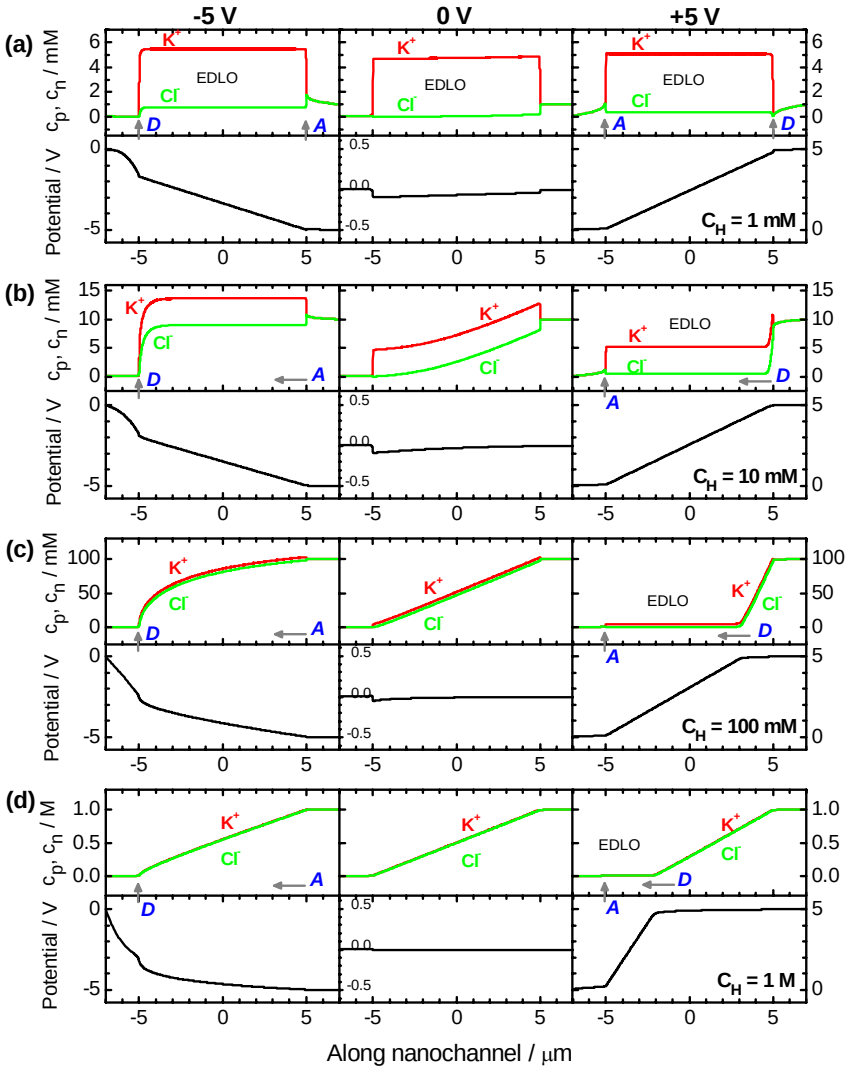

Figure 3.4 Calculated ion concentration (c_p and c_n) and potential profiles along a 20 nm thick, 10 μm long nanochannel (from x = -5 μm to 5 μm) placed between two KCl reservoirs containing different concentrations C_L (left) and C_H (right). In this system, C_L is set at ground potential and the concentration fixed to 0.1 mM while C_H is set at (a) 1 mM, (b) 10 mM, (c) 0.1 M or (d) 1 M, and is biased at -5 V, 0 V or 5 V shown in the columns from left to right. The results represent the averaged values taken across the height of the nanochannel as well as the areas with 20 nm high in the two reservoirs extending laterally from the nanochannel. The potential profiles at zero bias are plotted with an exaggerated scale. EDLO stands for EDL overlap. The *A* or *D* with indications denotes the locations of the accumulation or depletion of ions.

At low C_H concentration, i.e. 1 mM at which λ_D~10 nm, the EDLs overlap along the entire channel. As a result, the concentration of K ions is enhanced while that of Cl ions suppressed comparing with bath concentrations (Figure 3.4(a)). When the C_H reservoir is biased, both K and Cl ion concentrations slightly increase but the profiles remain flat in the channel. With such low ion concentrations in both sides, c.f. Figure 3.1(a), the EDL (the region inside the dashed boundary) overlap occurs despite of the asymmetry in the reservoir concentrations. Because the diffusive fluxes of both K and Cl ions are toward the same direction resulting to a negligible net diffusion current, we can envisage that the ionic conductance in nanochannel is mostly contributed by ion drift current driven by electric-field. Thus the amount of ion residing in nanochannel mirrors its conductance. Here, the ion concentrations in the nanochannel are controlled by the surface charge; hence, the applied potentials in the baths have marginal influence on the ion concentration inside the channel although they induce accumulation or depletion of ions near the channel entrance on either side. As a result, either positive or negative bias leads to almost the same ion concentration level and potential gradient, which explains the measured symmetric I-V characteristics. The rectifying factor I_F/I_R acquired from 4-nm and 20-nm thick nanochannels share a similar trend except that the 4-nm channel can maintain symmetric behavior up to 10 mM concentration while the 20-nm channel cannot.

This is simply because the Debye length at 10 mM concentration ($\lambda_D \sim 3$nm) is still larger than half of the channel size inducing a complete EDL overlap in the 4-nm channel.

As the C_H bath increases to 10 mM or 100 mM, the ion concentration profile, as shown in Figure 3.4(b) and (c), either buckles up or slumps depending on the polarities of the applied voltage. At zero bias, ion concentration gradients form along the nanochannel due to diffusion. However, when C_H is negatively biased, large amount of K and Cl ions accumulate from the C_H side, leaving upraised concentration gradients in the C_L side. The elevated cation and anion concentrations in the nanochannel lead to high channel conductance. On the other hand, when C_H is positively biased, both cations and anions are depleted to a low concentration resulting in extension of EDL-overlap along the nanochannel and hence low channel conductance. It is this different ion distribution that produced the rectifying effect observed in this regime.

With high concentration in C_H, 1 M for example, the amount of ions is large enough to shield the surface charges in nanochannels. In this case, almost no EDL overlap occurs throughout the entire channel except its very left end. As can be seen in Figure 3.4(d), the accumulation or depletion of both K and Cl ions are relatively less manifested and

produce a large, constant ion gradient along the channel. The reason for the weakened accumulation when C_H is negatively biased is that the potential drop in the nanochannel is reduced due to the access resistance produced by the depletion of ions around the channel access in the C_L bath. The higher the C_H, the greater the voltage drops across the access resistance in the C_L bath. In this case, the measured conductance is no longer the intrinsic property of the nanochannel. On the other hand, at positive bias, the amount of ion depletion remains comparably small as the background ion concentration in the nanochannel increases with high C_H. Voltage biases of different polarities show less influence on ion distribution; therefore, the asymmetric I-V characteristic is not observable.

3.2.5 Zero-current potentials in asymmetric ion concentration

Zero-current potentials were observed in the nanochannel devices containing asymmetric ion concentration. The potential is due to the combination of the offset voltage, ΔE, resulted from the different reference electrode potentials, and the reversal potential, E_r, across the channel that brings the total channel electric current to zero. Since the electrolyte concentrations in the two sides are different, the voltage drops at the two electrode-electrolyte interfaces will not be the same. The difference of the reference

electrode potentials, $\Delta E = \Delta E_H - \Delta E_L$, is expressed as $\Delta E = -kT/q \ln([Cl^-]_H/[Cl^-]_L)$. On the other hand, the reversal potential depends on nanochannel surface charge density and channel size. The reversal potential, which is contributed by the Donnan potential, E_{Donnan}, at the channel boundaries and the diffusion potential, E_{Diff} of the mobile ions in the nanochannel, can be approximately expressed by Teorell's theory [18] as $E_r = E_{\text{Donnan}} + E_{\text{diff}} = \frac{kT}{q} \ln\left(\frac{R_H}{R_L}\right) + \frac{kT}{q}\omega \ln\left(\frac{c_L}{c_H}\frac{R_L D_K + R_L^{-1} D_{Cl}}{R_H D_K + R_H^{-1} D_{Cl}}\right)$ for 1:1 electrolyte solutions, where R_x is the Donnan ratio on the x side, $R_x = -f/2c_x + \sqrt{1 + (f/2c_x)^2}$, f and c_x is the fixed charge concentration in the nanochannel and the bath concentration on the x side. D_i is the diffusivity of ion species i, and $\omega = (D_K - D_{Cl}) / (D_K + D_{Cl})$. The reversal potential increases with concentration ratio but saturates roughly after $C_H > f/2$. Both offset electrode potential and reversal potential are plotted in Figure 3.5.

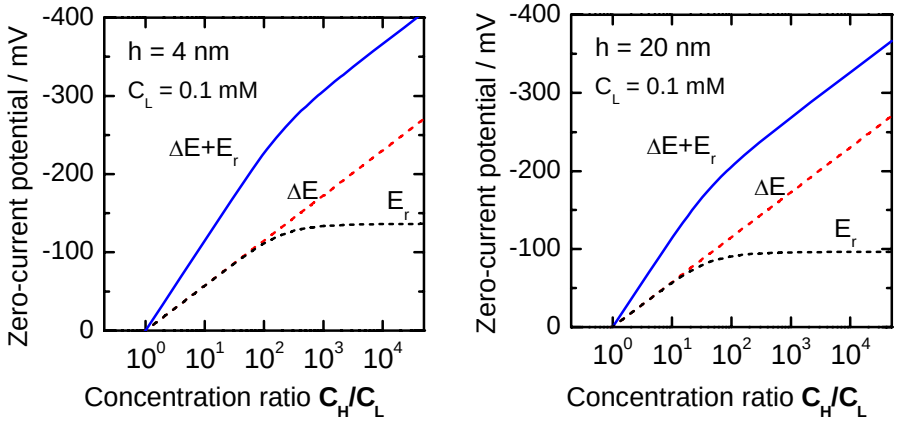

Figure 3.5 Calculated zero-current potentials (solid blue line) contributed by the reversal potential of nanochannels, E_r, (black dashes) and the offset electrode potential, ΔE, (red dashes) in 4 nm and 20 nm thick nanochannels at different concentration ratios.

The experimental data (Figure 3.6) extracted from the I-V curves for both 4 nm and 20 nm nanochannel increase about 74 mV/dec with the concentration ratio. They generally agree with the trend of the calculated results. The linear increase of potential without saturation indicates that the zero-current potential is dominated by the offset electrode potential, especially at high concentration ratio. More investigation is required by direct measurement of the reversal potentials across nanochannels. In that case, Ag/AgCl reference electrodes with saturated KCl bridges should be used to eliminate the offset electrode potentials.

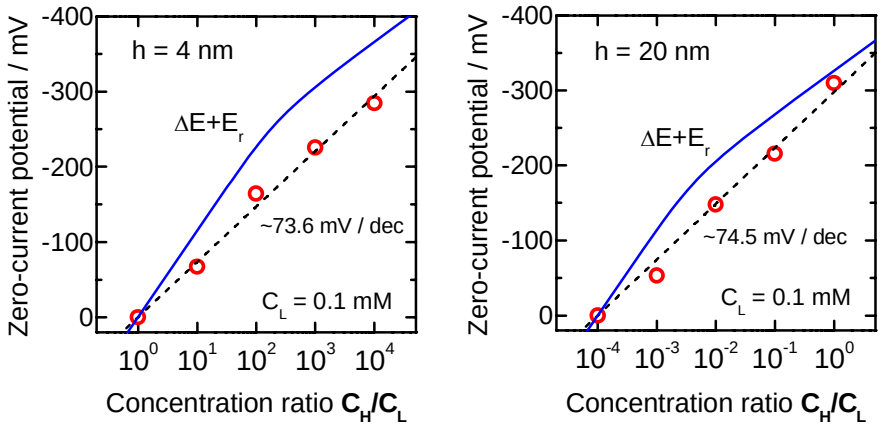

Figure 3.6 Measured zero-current potentials (red, empty circles) in 4 nm and 20 nm thick nanochannels at different concentration ratios. The experimental data increase proportionally with $\log C_H/C_L$ without saturation. The solid blue curves are calculated results.

3.3 Unified model for explanation of ion rectification in nanofluidic devices

3.3.1 Ion rectification in homogeneous nanochannels with asymmetric ion concentrations

While the calculated potential and concentration profiles obtained by solving PNP equations account for the asymmetric channel conductance, it brings up an interesting question: Why do the ions in nanochannels accumulate or deplete in the response to different bias polarities? The phenomenon can be explained by simply analyzing the drift current of K and Cl ions near the entrances at both sides of the nanochannel at the starting point of the transition right after the voltage is applied and the space charge that causes non-uniform electric potential has built up. In this moment, ionic concentrations are still nearly identical to that at equilibrium state and diffusion fluxes are negligible. Electroneutrality is assumed in the transient phase when ionic concentrations change over time and reach steady-state values. This method is an extension of Pu's analysis in explaining a similar effect at nanochannel-microchannel interface.[19] In their work, the ion-enrichment and ion-depletion effect was observed at low concentration by fluorescent microscopy. The effect also appears in our calculated result by PNP theory in the case of low concentrations shown in Figure 3.4(a) at which the EDLs overlap throughout the

channel. However, what is interesting is that when the bath concentration rises on one side, the ion accumulation and depletion develop inside the nanochannel. The resulting enhanced and lessened channel conductance hence becomes observable via electrical measurement.

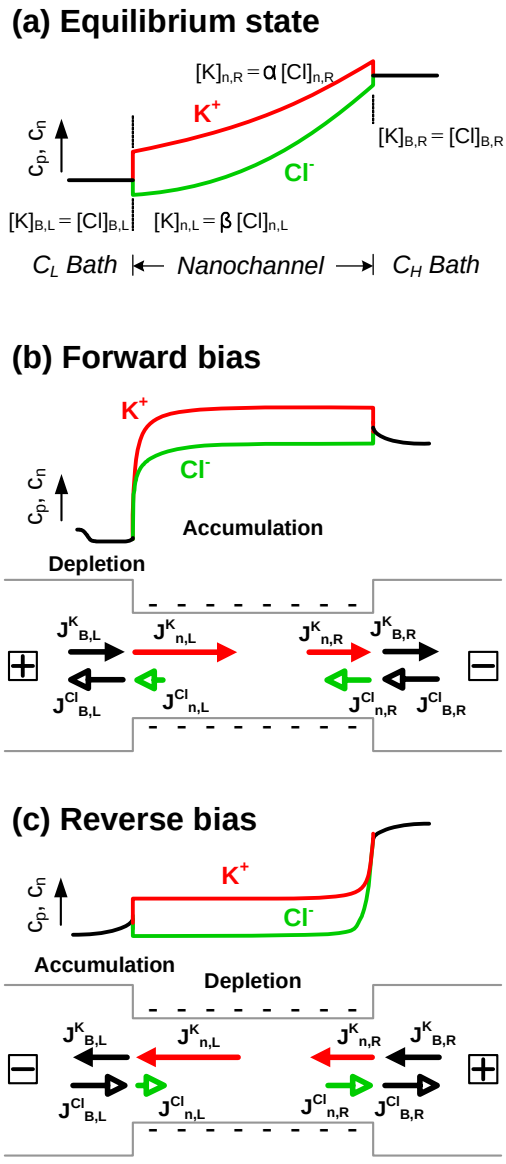

Figure 3.7 (a) Schematics of the simple model for the interpretation of the ionic rectifying behavior in a charged nanochannel with concentration gradient. The information of the

two bath concentrations are coupled to cation/anion ratios, α and β. (b) When the device is forward biased at which the applied electric field is against the concentration gradient, both K and Cl ions accumulate in the nanochannel but deplete at the channel entrance in C_L bath. (c) When a reverse bias is applied such that the electric filed directs along the concentration gradient, the ions are depleted in the nanochannel and accumulate at the channel entrance in C_L bath. The unbalanced ion currents produced under different bias polarities result in accumulation or depletion of ions in the nanochannel and hence asymmetric channel conductance.

Referring to Figure 3.7(a), consider the average K^+ and Cl^- ion concentrations outside and adjacent to the right entrance of the nanochannel. At equilibrium the concentrations of both ions are equal in the bath but are unequal in the charged nanochannel, yielding the relationships of $[K]_{B,R} = [Cl]_{B,R}$ in the bath and $[K]_{n,R} = \alpha [Cl]_{n,R}$ in the nanochannel, where α is the cation/anion ratio; B and n in the subscripts denote the bath and the nanochannel regions, respectively, and R, the right hand side. In a negatively charged nanochannel, α is greater than 1; and in a positively charged nanochannel, α less than 1. Likewise, a similar relation $[K]_{n,L} = \beta [Cl]_{n,L}$ can be set up for the left entrance of the nanochannel. In Donnan equilibrium, the averaged cation concentration ($\overline{c}_+$) and anion concentration ($\overline{c}_-$) can be calculated by solving the equation of electroneutrality $\overline{c}_+ - \overline{c}_- + f = 0$ combing with the law of mass action $\overline{c}_+ \cdot \overline{c}_- = c_b^2$, where c_b represents the bulk ion concentration outside, and f the nanochannel fixed charge concentration. The sign of f depends on the polarity of the fixed surface charge in

the nanochannels. The results give $\overline{c}_+ = -f/2 + \sqrt{(f/2)^2 + c_b^2}$ and $\overline{c}_- = f/2 + \sqrt{(f/2)^2 + c_b^2}$. Thus, the cation/anion ratio, which is equal to $\overline{c}_+/\overline{c}_-$, can be expressed as

$$\alpha \text{ or } \beta = \left(\frac{-f + \sqrt{f^2 + 4\ c_b^2}}{2c_b} \right)^2, \text{ where } f = \frac{2\sigma_s 10^{-3}}{qN_A h} \tag{3.1}$$

The fixed charge concentration *f* is a function of surface charge density σ_s (C/m^2), and channel height *h*. Equation 4 indicates that the lower the c_b, or the larger the *f*, the greater the cation/anion ratio α (or β) builds up. A unipolar solution of counter-ions is created in the nanochannel because the surface charge of nanochannels governs the ion concentrations. When $c_b > f/2$, the cation/anion ratio decreases as the surface charge has less influence on the ions in nanochannels. It should be notified that the proposed equation for cation/anion ratio is only an approximation for the case of high bath concentration at which nanochannels contain non-uniform potential across the cross section.

When a negative bias is applied to the right bath, for example, both K^+ and Cl^- ions migrate toward the opposite directions contributing to a drift current. By considering the current of ion *i* (*i* = K or Cl) developed in the nanochannel ($J^i_{n,x}$) and in the bath ($J^i_{B,x}$) on the x side (x = L or R for left or right, respectively), and combining with Kirchoff's

current law (i.e. conservation of currents at a node), we obtain the relations between the drift current in the nanochannel and the bath near the right entrance for K or Cl ions. The current relations are given by [19]

$$\begin{aligned} J_{B,R}^{K} &= \frac{\alpha^{-1} + \mu_k/\mu_{Cl}}{1 + \mu_k/\mu_{Cl}} J_{n,R}^{K} \\ J_{B,R}^{Cl} &= \frac{1 + \alpha\ \mu_k/\mu_{Cl}}{1 + \mu_k/\mu_{Cl}} J_{n,R}^{Cl} \end{aligned} \tag{3.2}$$

The subscript B, R represents the bath and the right side. By imposing an approximation that the electrophoretic mobilities μ_K and μ_{Cl} are very close,[14] equation (3.2) is reduced to:

$$\begin{aligned} J_{n,R}^{K}/J_{B,R}^{K} &= 2/\left(1 + \alpha^{-1}\right) \\ J_{n,R}^{Cl}/J_{B,R}^{Cl} &= 2/\left(1 + \alpha\right) \end{aligned} \tag{3.3}$$

On the basis of the derivation, likewise, we can describe the ratios of the current in the channel to that in the bath for each ion species at the left channel-bath interface, inside the nanochannel and the right channel-bath interface as following

$$\begin{array}{lll} \overbrace{\dfrac{J_{n,L}^{K}}{J_{B,L}^{K}} = \dfrac{2}{1+\beta^{-1}}}^{Left\ entrance} & \overbrace{\dfrac{J_{n,L}^{K}}{J_{n,R}^{K}} = \dfrac{1+\alpha^{-1}}{1+\beta^{-1}}}^{Nanochannel} & \overbrace{\dfrac{J_{n,R}^{K}}{J_{B,R}^{K}} = \dfrac{2}{1+\alpha^{-1}}}^{Right\ entrance} \\ \dfrac{J_{n,L}^{Cl}}{J_{B,L}^{Cl}} = \dfrac{2}{1+\beta} & \dfrac{J_{n,L}^{Cl}}{J_{n,R}^{Cl}} = \dfrac{1+\alpha}{1+\beta} & \dfrac{J_{n,R}^{Cl}}{J_{B,R}^{Cl}} = \dfrac{2}{1+\alpha} \end{array} \tag{3.4}$$

Each current ratio listed above can be used to predict if the ion species in that position will accumulate or deplete after an electric field is applied.

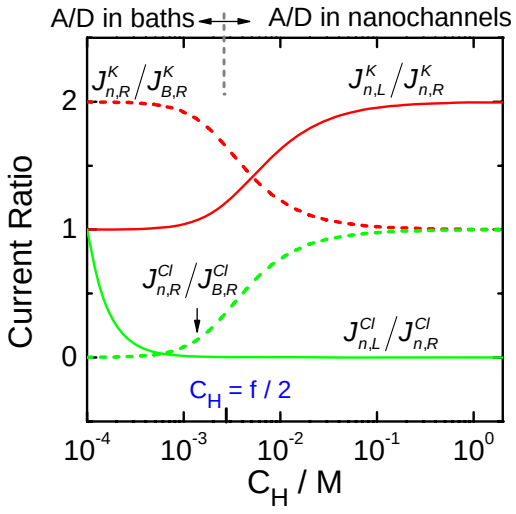

Figure 3.8 The plot of current ratios vs. C_H with $C_L = 10^{-4}$ M. The ratios of the currents developed in the left-hand and right-hand sides of the nanochannel $J_{n,L}/J_{n,R}$ (solid lines) for K and Cl ions approach unity when $C_H < f/2$ but diverge when $C_H > f/2$. The ratios of the currents developed inside and outside the nanochannel $J_{n,R}/J_{B,R}$ (broken lines) for K and Cl ions converge to unity when $C_H > f/2$ but diverge when $C_H < f/2$. The results represent the accumulation- depletion (A/D) of ions takes place in the bath at low C_H but in the nanochannel at high C_H.

Take the case of a negatively charged nanochannel with asymmetric bath concentrations for instance. The left bath contains $C_L = 10^{-4}$ M, the cation/anion ratio at the left entrance, β, is calculated to be ca. 2185, with given h = 20 nm and σ_s = 4.5 mC/m^2. The current ratios for left-entrance and nanochannel in (3.4) are plotted with respect to C_H in Figure 3.8. When $C_H < f/2$, both the counter-ion and co-ion currents in both ends of the nanochannel are very close ($J_{n,L} = J_{n,R}$) while those inside and outside the nanochannel are very different ($J^K_{n,R} > J^K_{B,R}$ and $J^{Cl}_{n,R} < J^{Cl}_{B,R}$). Similar result can be obtained in C_L bath. In this case, depending on the bias polarity, the accumulation or

depletion of both types of ion take place outside the nanochannel. Because the ion concentration in the nanochannel are predominately controlled by the surface charge of the channel and do not alter with the bias polarity, the ion conductance is symmetric. On the contrary, when $C_H > f/2$, as depicted in Figure 3.7(b) the ion currents in the left and right ends of nanochannel are asymmetric ($J^K_{n,L} > J^K_{n,R}$ and $J^{Cl}_{n,L} < J^{Cl}_{n,R}$) while at the right entrance the ion currents developed inside and outside the nanochannel are very close ($J_{n,R} = J_{B,R}$). As the device is forward biased as shown in Figure 3.7(b), i.e. the applied electric field is opposite to the concentration gradient, more ions are driven into the channel while less taken out. These uneven fluxes induce accumulation of both K^+ and Cl^- ions within the nanochannel and depletion of both near the channel entrance in C_L bath. Opposite results can be obtained at a reverse bias if the electric field is applied along the concentration gradient. In this condition, as illustrated in Figure 3.7(c), more ions are taken out of the channel than being injected into the channel, resulting in the depletion of ions in the nanochannel. The results explain why the ion concentration profiles buckle up at V_H = -5V but sinks at V_H = 5V as shown in Figure 3.4. In addition to the ion behavior in the nanochannel, the accumulation and depletion of ions at the regions adjacent to the channel (i.e. the channel access region), can affect the channel conductance. The depletion of ions, especially at the channel access in the

low-concentration C_L bath, increases the electrical resistance to the ion flux, and therefore generates an access resistance that is connected in series with the nanochannel. The effect of access resistance was observed when C_H increases to 1 M. The resistance reduces the amount of ions to be accumulated or depleted in the nanochannels due to the weakened electric field inside the nanochannel and, hence, less rectifying effect. The analysis can be applied to a positively charged nanochannel as well. In this case, the relation of the cation/anion ratios changes to $1 > \alpha > \beta > 0$. The rectifying effect will respond to opposite bias polarities. This result implies that the polarity of surface charge can be probed electrically by measuring the asymmetric I-V characteristics under a concentrations gradient besides its reversal potential which requires Ag/AgCl reference electrodes with saturated KCl bridges.

3.3.2 Ion rectification in conical nanopores

The function of conical nanopores can be explained by the same way. A conical nanopore has different pore sizes r, which is equivalent to different fixed charge concentrations, f ($= 2\sigma_s 10^{-3}/(qN_A r)$ approximately), on the two ends of nanopore. Because of the small opening, the nanopore's tip side has equivalently higher fixed

charge concentration, *f*, than its base, and therefore holds larger cation/anion ratio than the base side (Figure 3.9(a)). The cation/anion ratios at the two ends of the device has the relation of $\beta > \alpha \geq 1$. The relation results in the asymmetric ion currents in the nanopore-- $J_{n,L}^{K} > J_{n,R}^{K}$ and $J_{n,L}^{Cl} < J_{n,R}^{Cl}$. Similar to the previous conditions, at forward bias, the amount of K^+ ions driven into the nanopore from left entrance is more than those taken out through the right entrance. The Cl^- currents have like behavior except they go through the opposite direction. As illustrated in Figure 3.9(b), the unbalanced flow of ions result in the accumulation of both K+ and Cl- in the nanopore and consequently increase the conductance. By the same token, the reverse bias depletes both types of ions out of the nanopore (Figure 3.9(c)), yielding a low conductance.

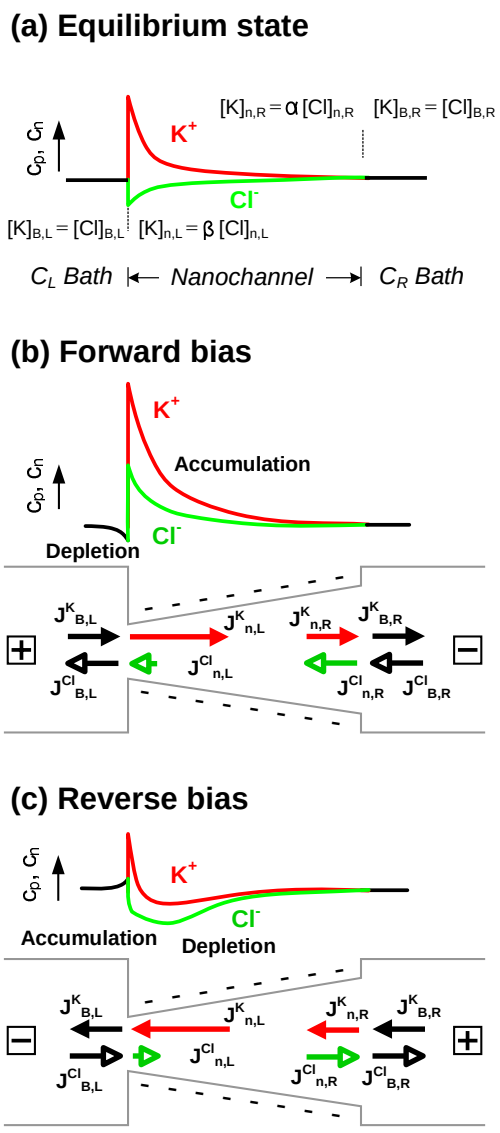

Figure 3.9 Interpretation of ionic rectification in conical nanopore based on the analysis of asymmetric ion currents building up right after the external electric fields are applied.

3.3.3 Ion rectification in nanofluidic diodes

In the case of nanofluidic diode, a p-i nanofluidic diode, which contains negative and neutral surface charges at the two sides of the nanochannel, has the condition of β

> $\alpha = 1$; while a p-n nanofluidic diode having negative and positive surface charges on the two sides or a bipolar membrane has $\beta > 1 > \alpha > 0$. As illustrated in Figure 3.10, when an electric field is applied to the device, the current in the negatively charged nanochannel is primarily carried by cations while the positive nanochannel by anions. As the electric field is applied from the negative nanochannel (p-type) to the positive nanochannel (n-type), the counter-ions in the both sides of nanochannel, $J_{n,L}^{K}$ and $J_{n,R}^{Cl}$, flow toward the junction. However, the minority anions in the negative channel, $J_{n,L}^{Cl}$, and the minority cations in the positive channel, $J_{n,R}^{K}$, flow outward from the junction with smaller magnitudes (Figure 3.10(b)). As a result, both types of ions accumulate in the nanochannel and will continue until it reaches a steady state value. The accumulation of ions makes the ion concentration in the nanochannel higher than that in the baths and, therefore, increases the conductance of the ions. On the contrary, if the electric field is applied in the opposite direction, ions will deplete from the junction. The depletion of ions in the nanochannel reduces its ionic conductance. As illustrated in Figure 3.10, it can be seen that with opposite polarity of counter-ions, a biased nanofluidic diode accumulates or depletes ions in nanochannel much more efficiently than the other two types of nanochannel. Therefore we anticipate that the nanofluidic diodes can have higher rectifying factor than conical nanopores or nanochannel with asymmetric ion

concentrations. The experimental demonstration of nanofluidic diode will be presented in the next chapter.

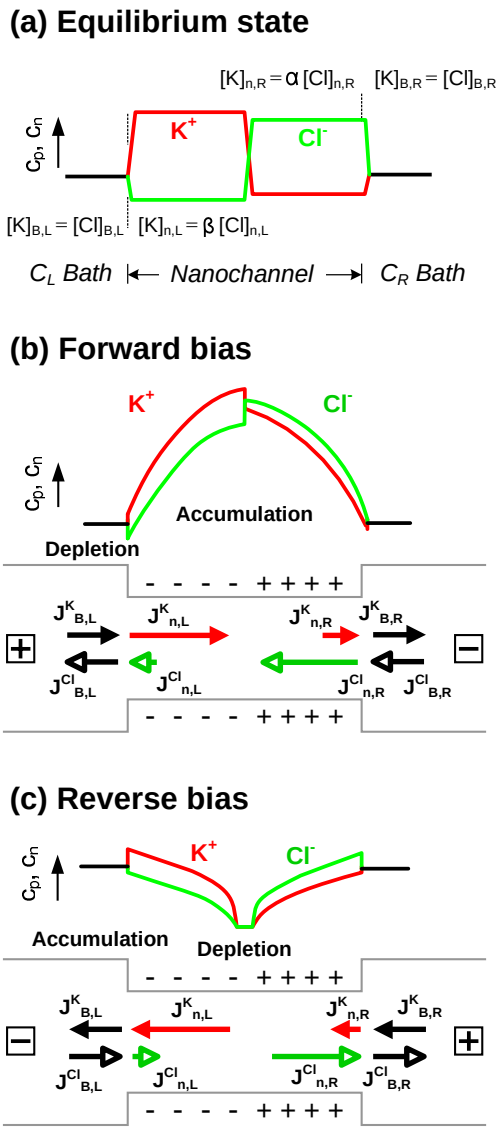

Figure 3.10 Interpretation of ionic rectification in conical nanofluidic diode on the analysis of asymmetric ion currents building up right after the external electric fields are applied.

3.4 Conclusion

In conclusion, the ionic rectifying effect was experimentally and theoretically investigated in 4 nm and 20 nm thick silica nanochannels under various concentration gradients. When the bath concentrations were set up to induce EDL overlap at single side of the nanochannel the rectifying effect appears. Based on the calculated ion profiles and the simplified model, we attribute the phenomenon to the accumulation or depletion of both cations and anions in nanochannels in response to different bias polarities. The model indicates that the basis of the ionic rectifying effect in the nanofluidic devices reported so far is to produce asymmetric cation/anion ratios or, equivalently, asymmetric build-in potentials at the two entrances of the nanochannels. The condition, therefore, allows the accumulation and depletion of ions in nanochannels to be controllable by the applied potential. The analysis also interprets the electrokinetic behavior at the junction of nanochannels and baths at low ionic concentrations. The result implies that the physics of nanofluidics may not be singled out without considering the nanofluidic-microfluidic interface. We will provide the experimental study of the effect of the microfluidic surface charge on nanofluidic ion transport in Chapter 5. The study improved our understanding of electrokinetic ion transport through nanochannels and will benefit the design of nanofluidic devices for attoliter to zeptoliter-scale chemical delivery.

REFERENCES

[1] Kasianowicz, J. J.; Brandin, E.; Branton, D.; Deamer, D. W. *Proc. Nat. Acad. Sci. U. S. A.* **1996,** 93, 13770-13773.

[2] Kuo, T. C.; Cannon, D. M.; Chen, Y. N.; Tulock, J. J.; Shannon, M. A.; Sweedler, J. V.; Bohn, P. W. *Anal. Chem.* **2003,** 75, 1861-1867.

[3] Karnik, R.; Castelino, K.; Fan, R.; Yang, P.; Majumdar, A. *Nano Lett.* **2005,** 5, 1638-1642.

[4] Dekker, C. *Nature Nanotechnology* **2007**, 2, 209-215

[5] Israelachvili J. *Intermolecular and surface forces*, 2nd ed; Academic Press: London, **2003**.

[6] Stein, D.; Kruithof, M.; Dekker, C. *Phys. Rev. Lett.* **2004,** 93, 4.

[7] Kovarik, M. L.; Jacobson, S. C. *Analytical Chemistry* **2007**, 79, 1655-1660.

[8] Siwy, Z. S. *Adv. Funct. Mater*. **2006**, 16, 735-746.

[9] Karnik, R.; Duan, C. H.; Castelino, K.; Daiguji, H.; Majumdar, A. *Nano Lett.* **2007,** 7, 547-551.

[10] Vlassiouk, I.; Siwy, Z. S. *Nano Lett.* **2007,** 7, 552-556.

[11] Schoch, R. B.; Renaud, P. *Appl. Phys. Lett.* **2005,** 86, 3.

[12] Behrens, S. H.; Grier, D. G. *J. Chem. Phys.* **2001,** 115, 6716-6721.

[13] Karnik, R.; Fan, R.; Yue, M.; Li, D. Y.; Yang, P. D.; Majumdar, A. *Nano Lett.* **2005,** 5, 943-948.

[14] The ion mobilities: $\mu_K = 7.619\times10^{-8}$ m^2/V s, $\mu_{Cl} = 7.912\times10^{-8}$ m^2/V s.

[15] Ho, C.; Qiao, R.; Heng, J. B.; Chatterjee, A.; Timp, R. J.; Aluru, N. R.; Timp, G. *Proc. Nat. Acad. Sci. U. S. A.* **2005,** 102, (30), 10445-10450.

[16] Eisenberg, R. S. *J. Membr. Biol.* **1999,** 171, 1-24.

[17] Chen, D. P.; Barcilon, V.; Eisenberg, R. S. *Biophys. J.* **1992,** 61, 1372-1393.

[18] Zambrowicz, E. B.; Colombini, M. *Biophysical Journal* **1993,** 65, 1093-1100.

[19] Pu, Q. S.; Yun, J. S.; Temkin, H.; Liu, S. R. *Nano Lett.* **2004,** 4, 1099-1103.

Chapter 4

Ion Transport in Heterogeneous Nanochannels – Nanofluidic Diodes

4.1 Introduction

Ionic current rectification can be generated in a nanochannel with asymmetric ion distributions in nanochannels. A more direct way to control and produce an asymmetric ion distribution along a nanochannel is by creating asymmetric surface charge itself. The idea of nanofluidic diode consisting of opposite surface charges on either half of the nanochannel was proposed by Daiguji and his coworkers to give rectification of ion current.[1] The fundamental of this device structure is essentially the same as the widely-studied bipolar membranes in electrochemistry. It is know that bipolar membranes, composed of a negatively charged cation exchange membrane and a positively charged anion exchange membrane, presents ion rectification[2] and has been used for decades in many applications such as electrodialysis and chemical separation.[3,4]

Possessing similar properties but much smaller size, nanofluidic diodes may be integrated on a fluidic chip to perform pH control and chemical separation process.

4.2 Mechanism of current rectification in nanofluidic diodes

Similar to bipolar membranes, the function of the device is based on the opposite surface charge distributing asymmetrically along the nanochannel: one half of the channel has positively-charged surface while the other half negative in aqueous solutions. The mechanism of the ion transport in this system is illustrated in Figure 4.1 and is described as following. It is known that the charged surface in a nanochannel can enhance the counter-ion concentration inside and hence produces a unipolar ion solution. The positively-charged nanochannel contains more anions while the negatively-charged one has more cations. When a forward bias is applied on the device, i.e. a positive voltage applied to the side of the negatively charged nanochannel with the other side grounded, both the majority cations in the negative channel and the majority anions in the positive channel migrate toward the junction driven by the electric field. As a result, at steady state, both types of ions pile up around the nanochannel junction. Thus, the high ion concentration leads to large channel conductance. At reverse bias, i.e. a negative bias applied to the negatively charged nanochannel with the other side grounded, both the

majority cations and anions are extracted out of the channel creating a depletion zone at the junction. As a result of the ion depletion, channel conductance is reduced significantly. It is the depletion and accumulation of ions in the nanochannel that produce the rectifying effect.

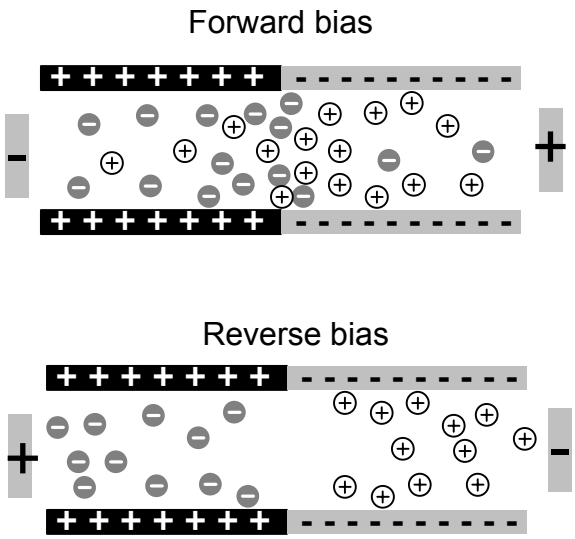

Figure 4.1 Mechanism of rectifying effect in a nanochannel with opposite surface charge on either side.

4.3 Current technologies for nanofluidic diodes

The key challenge to creating nanofluidic diodes is to obtain different surface charges on a nanochannel. Karnik and his coworkers developed diffusion-limited patterning (DLP) to pattern the cationic protein avidin inside biotinylated nanofluidic

channels.[5] The nanofluidic channels were fabricated by removing 30 nm thick silicon sacrificial channel patterns in a silica layer. The process procedures are similar to those described in the previous section. To form asymmetric surface charge distribution, the whole surfaces of the 30 nm thick nanofluidic channel was first covered by biotin. Avidin was then introduced from one of the channel openings until half of the nanochannel length was covered with the avidin protein molecules.[6] Since the avidin coated and biotinylated surfaces contain positive and neutral surface charges, respectively, the surface charge discontinuity is created in the nanochannels. Vlassiouk et al. reported a nanofluidic diode created by modifying the surface chemistry of the conical nanopores in PET membranes.[7] The surface of the nanopore was modified to have one half of the nanopore covered by carboxyl groups and the other half amino groups. The dependence of rectifying behavior on the pH values and electrolyte concentrations were studied. It was found that the maximum rectifying factor occurs at pH ranging from 4 to 7 at which the surface charge densities were maximized. Furthermore, the rectifying factor achieves about 120 at 10 mM KCl but decreases by 2 orders of magnitude when the concentration increases from 10 mM to 1 M.[7] Because the weakened rectifications at higher concentration results from the change of ion transport behavior from electrophoresis to

electroosmosis, the authors conclude that it is electrophoresis that depletes the ions from the nanofluidic diode at reversed bias. [7]

The drawbacks of the above surface chemical modification approach are two folds: 1) the proteins used have finite sizes and could change the nanochannel dimension and may interfere with other molecular transport; and 2) such surface charge preparation is time consuming and not robust enough such that it can only be used at close to the ambient temperature environment. We introduced a technique to create asymmetric surface charge distributions by using different solid state oxide materials of different isoelectric points (pI). We fabricated bipolar nanochannels which have negatively-charged silicon dioxide nanochannels and positively-charged Al_2O_3 nanochannels connected in series. The oxide nanofluidic diode relies on the arrangement of these oxide materials using microfabrication technology without chemical treatments.

4.4 Materials selection for heterogeneous nanochannels

4.4.1 Physical and chemical properties of solid oxide surfaces

A material possessing hydrophilic surface and electrically insulating property is considered to be our candidate materials for solid state nanofluidic channels. Solid oxides

in aqueous suspension are generally electrically charged. The charge-dipole interaction between oxide surfaces and water molecules makes oxide surfaces hydrophilic. Positive or negative surface sites can be developed on the surface of solids in contact with aqueous solutions. In the case of oxide or hydroxide surfaces, these sites are protonated or deprotonated following the equilibrium $-\mathrm{MO} + \mathrm{H}^+ \rightleftharpoons -\mathrm{MOH}^+$ or $-\mathrm{MO}^- + \mathrm{H}^+ \rightleftharpoons -\mathrm{MOH}$, where –MO denotes a surface solid oxide group.[8] The surface charge changes with the pH. As the pH increases, the equilibrium shifts to the left resulting in less positive charges or more negative charges. At a certain pH value, the charge becomes zero, and at lower pH values it becomes positive. The pH value at which the surface carries no net charge is defined as isoelectric point (pI). At this pH, the amount of positive surface charge equals to that of negative charge. For instance, MgO can become hydroxylated upon exposure to H_2O. The adsorption of water results in the formation of $MgOH^+$ or $Mg(OH)_2$ which yields an isoelectric point (pI) of about 12 for a MgO surface. Other metal oxides such as NiO and Al_2O_3 surfaces also produce positive charge in water suspension and have pI about 10 and 8, respectively. Silica SiO_2 surfaces acquire negatively charged SiO^- in contact with water by dissociation of silanol groups and its pI is about 2 to 3. Similar to the electrostatic interaction in the acid dissociation process, the strength of the oxyacids in the surface -MOH groups depends on cationic

size and charge. It was found pI roughly varies linearly with the ratio of ionic charge (Z) to solid oxide ionic radius ($R = 2\ r_o + r_+$), Z/R, where r_o and r_+ are oxygen and cation radius, respectively. Isoelectric point increases as Z/R decreases.[8] A surface –MO group with shorter radius R tends to deprotonate, leaving negative charges and therefore has lower pI. Take MgO, Al_2O_3 and SiO_2 for exam, in terms of the solid oxide radii, R, they have the relationship of $SiO_2 < Al_2O_3 < MgO$. Likewise, their pIs show a similar relationship (Figure 4.2). On the other hand, NiO has a similar high pI to MgO because the lattice constant of NiO (4.18 Å in (100)) is very close to that of MgO (4.21 Å in (100)).[9]

Apart from surface charge, the solid oxides for nanochannel should be electrically insulating. Otherwise, additional current shunt path through the conductive channel walls would develop under an applied voltage bias. The data of isoelectric point (pI) and energy bandgap for various oxide materials collected from reference 8 and 9 are summarized in Figure 4.2. The values of each material may vary depending on their preparation methods. Among these solid oxides, non-transitional-metal oxides such as SiO_2, Al_2O_3 and MgO are preferred because they have larger energy bandgaps and therefore are good insulating materials. Most transition-metal oxides are relatively easily reduced to form semiconducting or metallic phases because their lower part of the

conduction band originates from the d rather than s orbital, resulting in lower energy bandgap. NiO was selected for study in solid oxide nanochannels because of its positive surface charge, relative high band-gap (about 3.9 eV) and the compatibility to the standard microfabrication process. Other than oxides, silicon nitride is one of the widely used insulating materials in microfabrication. However, its hydrophobic surface makes it not suitable for nanofluidic applications. An additional oxidation is required to wet a silicon nitride surface. By applying different solid oxides having distinct pIs in a nanofluidic device, we can tailor surface charge distributions in the nanochannel and hence produce nonlinear ion transport behavior such as ionic rectification.

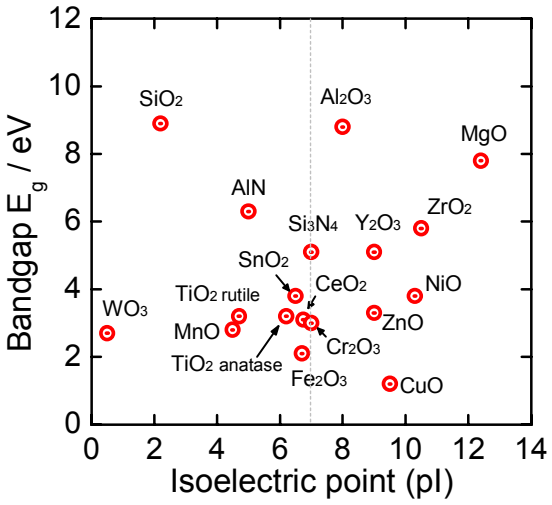

Figure 4.2. Summarized isoelectric point (pI) vs. energy bandgap (Eg) data of different metal oxides. The data may vary depending on the preparation methods.

4.4.2 Surface charge characterization of solid oxide surfaces

The isoelectric points of the oxide surface tell the polarity of surface charge at a certain pH but do not give any information about their surface charge densities. To estimate the surface charge density of each material surface that will be used for heterogeneous nanochannels, we extracted the data by measuring the electroosmotic flow (EOF). The EOF experiments were performed in a 80 μm thick, 0.5 cm wide and 1 cm long microfluidic chambers formed by two pieces of glass slides coated by the thin oxide films of interest. The channel is straight and homogeneous with a uniform surface charge density. The Al_2O_3 and MgO thin films, about 50 nm thick, were deposited directly from Al_2O_3 and MgO sources by e-beam evaporation at the pressure of about 7×10^{-6} Torr. The NiO was formed by oxidizing a 10 nm thick e-beam evaporated Ni thin film. Oxidation was performed at 400^{o}C on a hotplate in the air. In the electroosmosis experiment, The EOF velocity was coarsely measured by observing the speed of the 1-μm diameter polystyrene beads carried by the flow in a 0.1 mM KCl solution. The dimensions of the microflow chamber are much larger than the Debye length. Under the assumptions that the fluidic properties are uniform and with no-slip boundary condition, EOF velocity v_{EOF} is given by Smoluchowski equation which is proportional to the electric-field, E, applied along the chamber and is expressed as $v_{\mathrm{EOF}} = -(\epsilon_0\epsilon_r\zeta/\eta)\,E$, where $\epsilon_0\epsilon_r$ is the

electrical permittivity, ζ the zeta-potential and η the viscosity of the solution. From the EOF mobility measurement, we deduce the ζ-potential of the four different oxide surfaces. Although ζ-potential is defined as the electrical potential at which the flow is zero rather than the surface potential of the chamber wall, these two boundaries are very close, therefore, we can still estimate the effective surface charge density σ_{eff} by the Grahame equation $\sigma_s = \sqrt{8\epsilon_0\epsilon_r kT\, n_b}\,\sinh(q\,\psi_s/2kT)$, where n_b is the number density of ions in the bath and the surface potential ψ_s is assumed to be ζ-potential. (See appendix B for more detail)

Figure 4.3 shows that the measured EOF velocities v_{EOF} change almost linearly with applied electric-field. It was observed that in the silica microfluidic chambers the fluid flows against the applied electric field, while those in MgO, Al_2O_3 and NiO chambers flow along the electric field direction. The flow directions imply that silica has negative surface charge and the other three metal oxide surfaces are all positively charged. This is anticipated results according to Fig. 4.2. The slope of the data is the electroosmotic mobility $\mu_{eo} = -\epsilon_0\epsilon_r\zeta/\eta$. Table 1 summarized the electroosmotic mobility μ_{eo}, ζ-potentials and the effective surface charges σ_{eff} of these four different oxides extracted from the electroosmotic flow experiment. The resulting effective surface charge of silica (-4.24 mC/m^2) is very close to the result obtained by measuring the ionic conductance in

silica nanochannels which is about -4.5 mC/m^2. To examine the influence of the process in nanochannel fabrication on the oxide surface property, the same experiments were performed in the oxides exposed to gaseous XeF_2 for half an hour followed by O_2 plasma treatment. No discernible difference in surface charge densities was observed comparing to the untreated surfaces. The surface charge density of each oxide materials would vary with preparation method. In our case, the Al_2O_3 and MgO thin films were prepared by e-beam evaporation with no oxygen ambient. The lack of O_2 compensation may lead to the shortage of oxygen bond on the surface and result in lower density of surface charge.

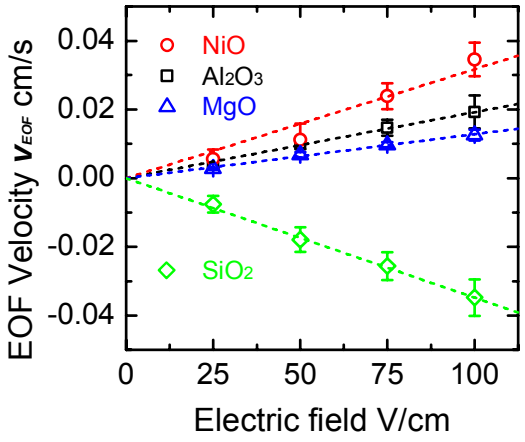

Figure 4.3 Electroosmosis flow velocity as a function of the apply electric field in the microfluidic chambers made of different oxide surfaces.

Table 4.1 Summarized electroosmotic mobility μ_{eo}, ζ-potentials, and effective surface charges σ_{eff} deduced from EOF experiment

	SiO_2	Al_2O_3	MgO	NiO
μ_{eo} (cm^2/V s)	-0.0348	0.0192	0.0128	0.0317
ζ (mV)	-49.1	27.1	18.0	44.8
σ_{eff} (mC/m^2)	-4.24	2.10	1.36	3.77

4.5 Solid oxide nanofluidic diodes

The heterogeneous oxide nanochannels are composed of negatively charge silica nanochannel and positively charged metal oxide nanochannel. NiO and Al_2O_3 were used to make positively charged channels. However, Al_2O_3 is preferred in the process, since after nanochannels are formed, an additional oxidation of Ni is required to obtain NiO and, besides, the oxidation process thickens the original Ni layers and hence shrinks the size of nanochannel, making the dimension control difficult.

4.5.1 Fabrication of solid oxide nanofluidic diode

Similar to the fabrication method for homogeneous nanochannels described in chapter 2, the solid oxide nanofluidic diode was fabricated in the same way except that two additional thin metal oxide or metal patterns were deposited before and after forming

the a-Si sacrificial structures, as illustrated in Figure 4.4. If metal thin films are used in this step instead of direct deposit of metal oxide, an additional oxidation will be performed after sacrificial layer is removed either in furnace or by O_2 plasma.

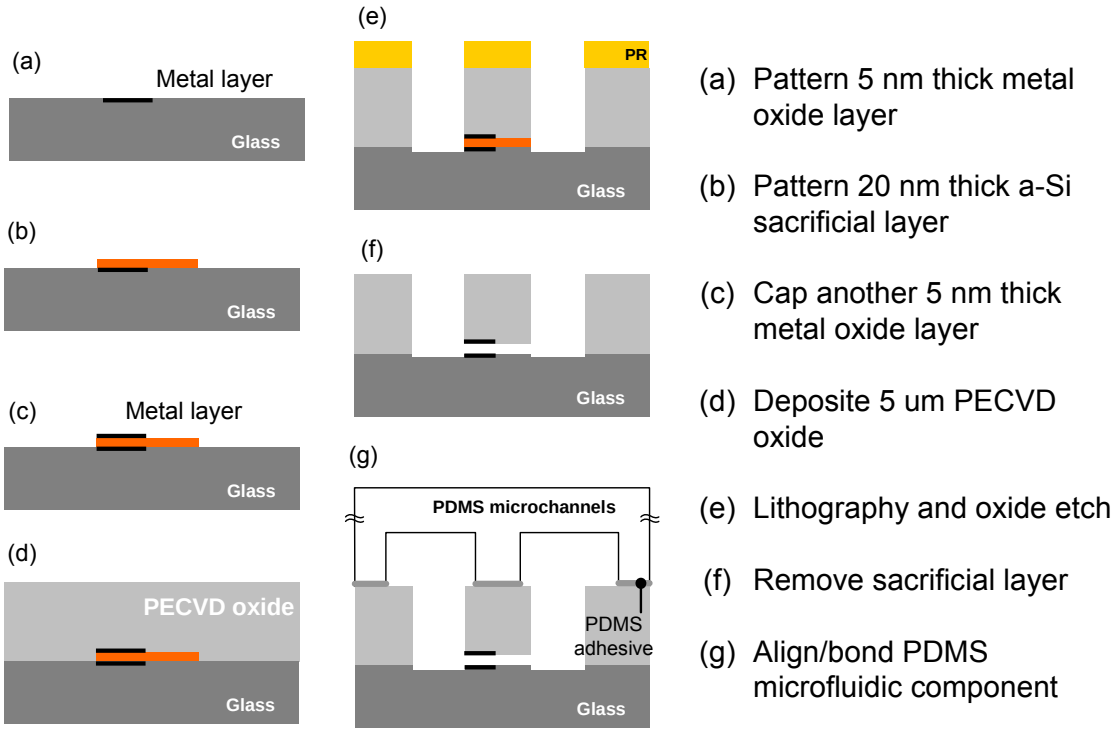

Figure 4.4 Fabrication sequence of a heterogeneous nanochannel

After the removal of sacrificial layer, the nanofluidic device has half of the channels made of silica surface and the other half Al_2O_3. The Al_2O_3 parts can be replaced by NiO as well because both of these two oxide surfaces have their pIs greater than 7. Figure 4.5

shows a microscopic image and a schematic of a 60 μm long nanofluidic diode which consists of one half of nanochannels covered with Ni surfaces (bright parts on the bottom) and the other half of silica nanochannels. The image was taken before thermal oxidation. After oxidation, the nickel thin films were oxidized to form NiO and became as transparent as Al_2O_3. Note that since the NiO thin films require additional thermal oxidation step, to facilitate the fabrication process, Al_2O_3 is preferred and used in most of our device fabrication. Taking the advantage of the surface property of the solid state oxides and their high stability, positively and negatively charged surfaces can be generated in aqueous solution within a range of pH values.

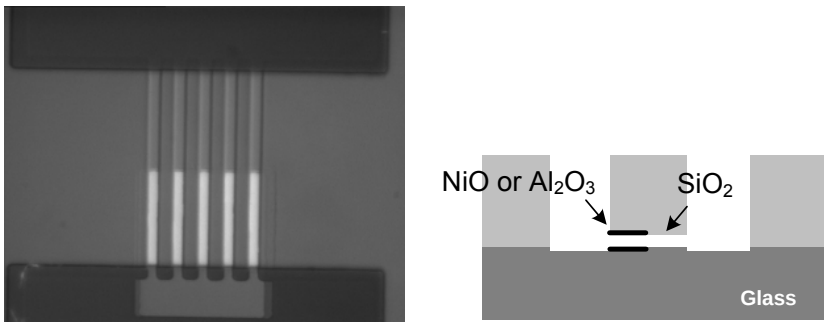

(a) (b)

Figure 4.5 Microscopic image (a) and schematic (b) of a nanofluidic diode

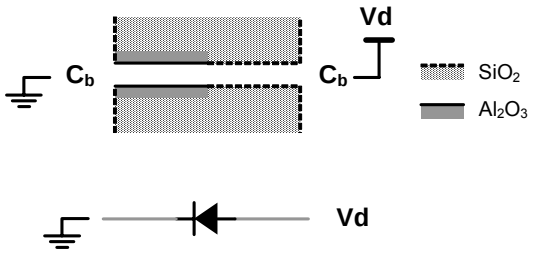

Figure 4.6 Schematic of the nanofluidic diode measurement setup and its equivalent circuit.

4.5.2 Characterization of nanofluidic diode and comparison with theoretical calculation

The current-voltage characteristics of the SiO_2-Al_2O_3 nanofluidic diode was measured at varied bath KCl concentrations ranging from 10 μM to 1 M. In the measurement, as illustrated in Figure 4.6, a voltage bias V_d was assigned to the bath that connects to SiO_2 nanochannel while the Al_2O_3 side was grounded. As shown in Figure 4.7(a)-(f), the I-V curves display strong rectification effect at every concentration except 1 M. To show a clear view of the reverse-bias currents, all the I-V curves are summarized in a semi-log graph in Figure 4.8(a). It can be found that both reverse-bias currents and forward-bias currents increase with bath concentrations. The rectifying factor defined as the ratio of forward-bias conductance to reverse-bias conductance (Figure 4.8(b)) reaches its maximum (330) when the bath KCl concentration is 1 mM; but degrades significantly

with the increase of concentration above 1 mM. Below 1 mM, the rectifying factors are still relatively high: about 200 for 0.1 mM and 30 for 0.01 mM. Such high rectification behavior was not observed in the prior works. By plotting the data in a log-log graph (Figure 4.9), we found that the conductance of the nanofluidic diode shows an interesting relationship with the bath ion concentrations. When the bath concentration is below 1 mM, both the forward-bias and reverse-bias conductances do not change too much with concentrations. However, as the bath concentration c_b increases above 1 mM, both conductances increase and show a power law dependence on c_b: the forward-bias conductance G_F with a power factor of ~ 0.62 while the reverse-bias conductance G_R with ~ 1.47, i.e. $G_F \propto c_b^{0.62}$ and $G_R \propto c_b^{1.47}$. Note that the geometric average of these two conductances is proportional to c_b with a unity power factor, i.e. $\sqrt{G_F G_R} \propto c_b$. Such effect is similar to the ion transport behavior in a homogeneous nanochannel. At low c_b the channel conductance is governed by the surface charge in the nanochannel and independent of c_b. When c_b is high enough and the Debye length is short compared to the channel size, the channel conductance increases linearly with c_b.

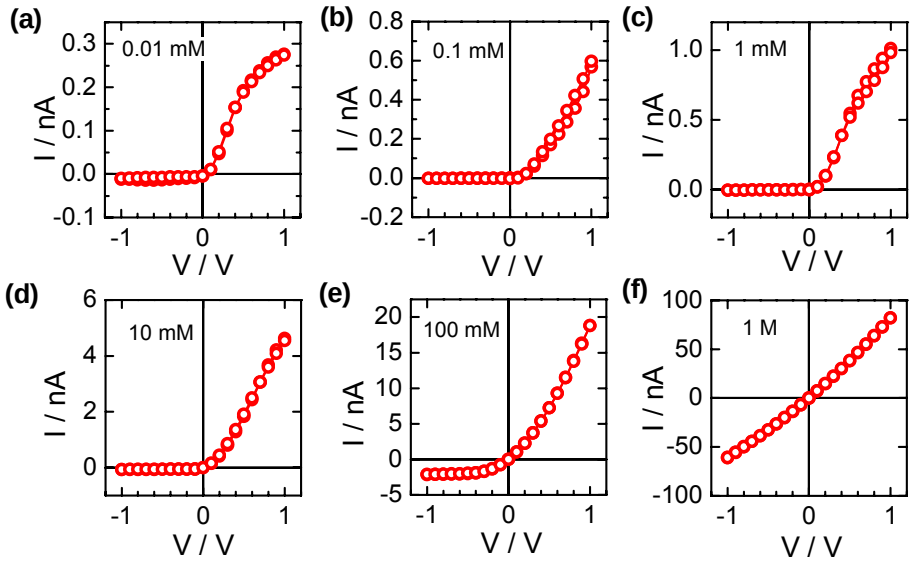

Figure 4.7 I-V characteristics of nanofluidic diode measured at different bath KCl concentrations, (a) 0.01 mM, (b) 0.1 mM, (c) 1 mM, (d) 10 mM, (e) 100 mM and (f) 1 M. The equivalent channel width is 2.5 μm×10.

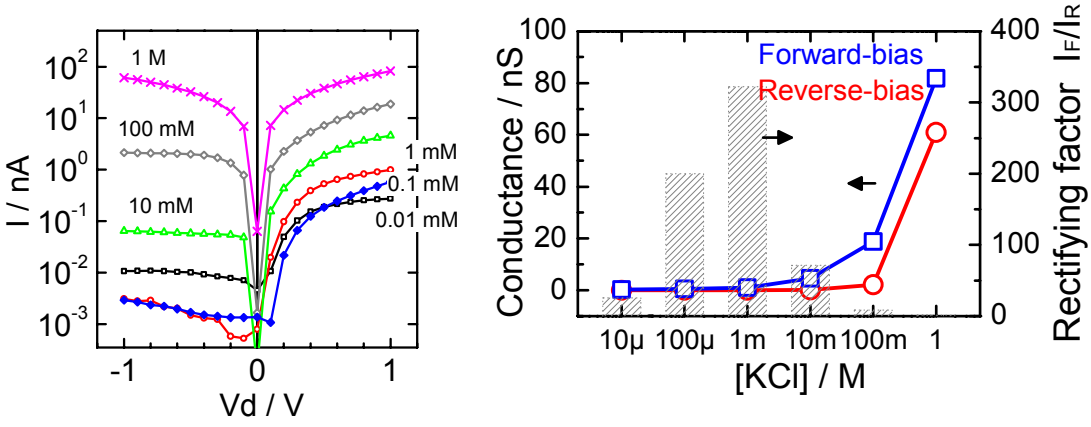

(a) (b)

Figure 4.8 (a) Summarized I-V characteristics of nanofluidic diode in a semi-log graph to show the reverse currents in more detail. (b) Summarized forward-bias conductances G_F, reverse-bias conductances G_R and the rectifying factors at different bath concentrations.

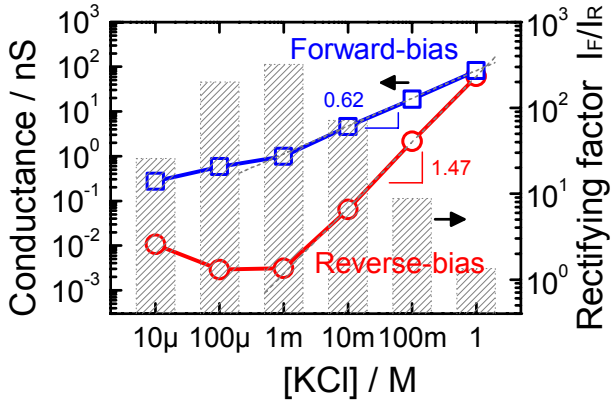

Figure 4.9 Log-log plot of the forward-bias conductances G_F, reverse-bias conductances G_R and the rectifying factors at different bath concentrations.

To compare the experimental results with theory, we calculated the ion concentration distributions and potential profiles in a nanofluidic diode under the biases of -1 and 1 V to study how the bath ion concentrations affect the channel conductances. As plotted in Figure 4.10, it is shown that a forward bias (Vd = 1 V in the right column) can accumulate both cations and anions inside the nanochannel, whereas a negative bias (Vd = -1 V in the left column) can deplete ions at the junction in the center. When the bath concentration is below 10 mM, the ions at the channel junction (x = 0) are depleted resulting in a low ion conductance. Because the ion concentration is very low in this depletion region, a high voltage drop is induced at the junction. This effect is very similar to that in a reverse-biased semiconductor p-n diode where the mobile charges are depleted and a large electric field is created at the junction region. When the bath

concentration is above 10 mM, the channel surface charge has less impact on the ion conductance and consequently a reverse bias cannot completely deplete the ions at the channel junction. Although the total amount of ions is reduced in the channel, the ion concentration at the channel junction is much higher than the previous case. Therefore, the reverse-bias conductance increases with bath concentrations. It is also found that at every concentration above 10 mM, the amount of ions in the channel being accumulated or depleted is about the same. Higher bath concentrations do not induce or repel more ions. That is why the rectifying effect of nanofluidic diodes is degraded at high bath concentrations.

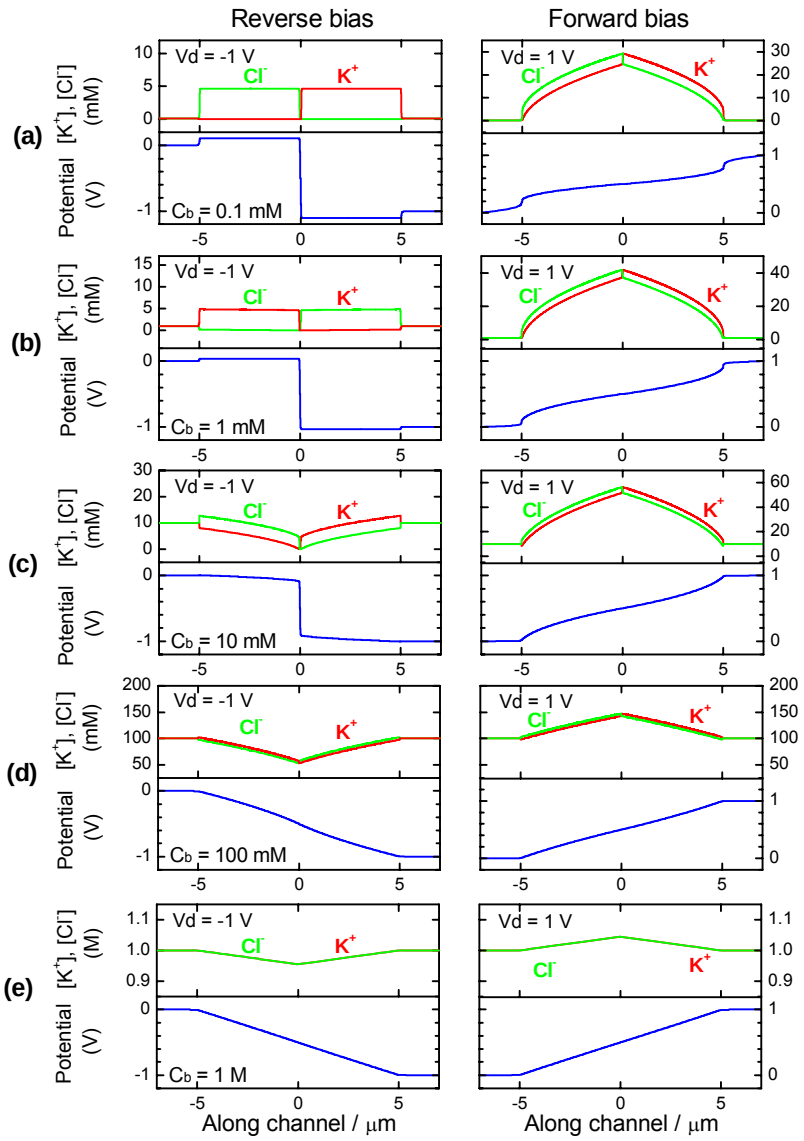

Figure 4.10 Calculated ion concentration distributions and potential profiles of a nanofluidic diode biased at -1 V (reverse bias) and 1 V (forward bias) and at various bath concentrations: (a) 0.1 mM, (b) 1 mM, (c) 10 mM, (d) 100 mM and (e) 1 M.

The ion conductance of the nanofluidic diode at different bath concentration is calculated and plotted in Figure 4.11. It shows that the forward-bias conductance does not change too much at low bath concentrations but increases more rapidly as bath

concentrations exceed 10 mM. The reverse-bias conductance basically matches the experimental results except at low bath concentrations. Note that the power law factors in the calculated results also match very well with the experimental data. The calculated result suggests that the reverse-bias conductance should decrease continuously with reducing bath concentrations, which deviates from the experimental observation. We think there may be other effects not considered in the calculation that generate additional currents at low concentration regime. One of the possibilities is the enhanced water dissociation rate under large electric field could cause additional currents carried by the H^+ and OH^- ions that are not considered in our current model.

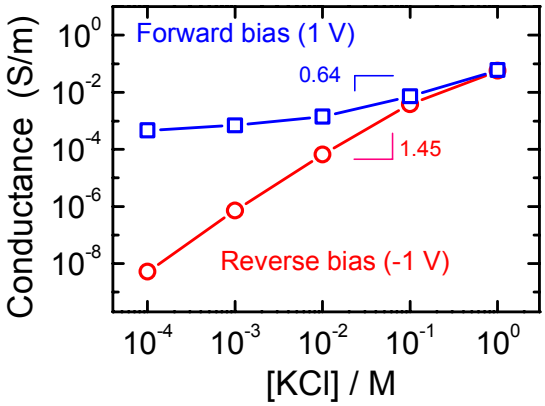

Figure 4.11 Calculated nanofluidic diode conductances under forward and reverse biases.

It worthwhile to point out that at low concentration the current can saturate under a high forward bias. For example, the I-V curve in Figure 4.7(a) starts saturating at 1 V. As will be described in the next chapter, the current saturation can result from the surface

charge on the bath side-wall which creates a parasitic nanofluidic access diode connecting back-to-back with the nanofluidic channel diode as illustrated in Figure 4.12(a). Figure 4.12(b) shows the current saturation in a nanofluidic diode with 0.01 mM bath concentration. The I-V curve was obtained by sweeping current and probing voltage. The forward current saturates at high voltage because as the voltage bias increases (Vd > 0) although the channel diode (solid diode in the equivalent circuit) is forward biased, the parasitic access diode (empty diode) becomes reverse-biased. The calculated potential profile in Figure 4.13 also demonstrates that under a large forward bias (Vd = 5V), a big voltage drop takes place at the left channel access which is a Al_2O_3 nanochannel connecting to the SiO_2 bath side-walls. The ion concentration there is depleted. As a result the ion conductance is restricted with increasing Vd. More details about the parasitic nanofluidic access diode will be discussed in the next chapter.

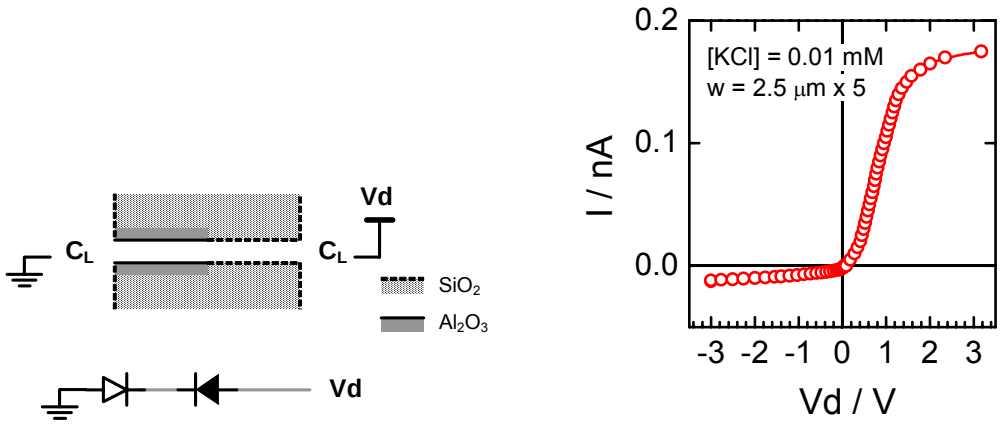

(a) (b)

Figure 4.12 (a) Parasitic nanofluidic access diode (empty diode in the equivalent circuit) appears in the nanofluidic diode device at low bath concentrations and high applied

forward bias. (b) Measured I-V curve of the nanofluidic diode showing the effect of parasitic nanofluidic access diode.

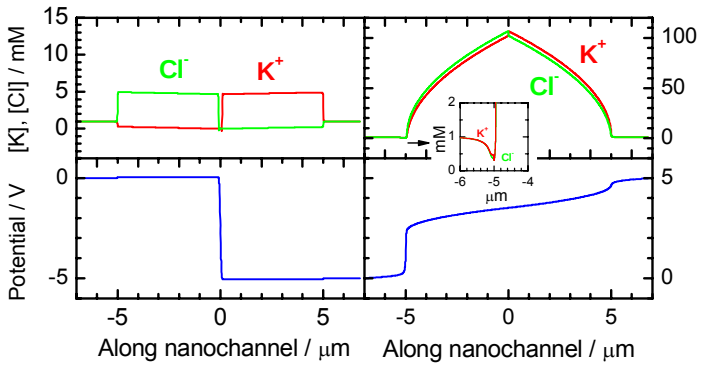

Figure 4.13 Calculated ion concentration distributions and potential profiles in the nanofluidic diode containing a parasitic nanofluidic access diode.

4.6 Comparison of rectifying effects in nanofluidic diodes and semiconductor diodes

As mentioned in the beginning of the chapter that the ionic and electronic systems share many similarities, it would be interesting to compare the physics behind the current rectification in a nanofluidic and a semiconductor diode. When a n-type and a p-type semiconductor is put together, a positive and a negative space charge region is established at the junction, and the mobile charges are depleted. The resultant built-in potential due to the formation of space charge impedes the diffusion of majority carriers from both types of semiconductor to cross the junction. In a nanochannel p-n diode similar situation takes place as discussed earlier.

While both nanofluidic diodes and semiconductor diodes exhibit similar rectifying

I-V characteristics, they work differently in some ways. For instance, the forward-bias current in semiconductor diodes is dominated by the diffusion of charge carriers having enough energy to overcome the built-in potential in the space-charge region. Once across the junction, these charge carriers becomes the minority carriers, which will recombine with the majority carriers within about a diffusion length from the edge of depletion or space-charge region. The result limits the potential drop in the depletion region, shielding the rest of the device from the effect of an electric field. But in a nanofluidic diode, there is no combination of a cation and an anion in the solution. Therefore, when the majority cations flow from the negative channel across the junction driven by a forward bias, they will keep flowing through the positive channel. Meanwhile, the majority-anion concentrations in the positive channel must have a corresponding change in their distributions throughout the entire channel to maintain electroneutrality. In this case, the applied electric field affects the entire device, and drift current dominates the forward-bias ion flow.

4.7 Conclusion

Nanochannels containing asymmetric surface charge distribution can produce rectification of ion transport. The phenomena can also be found in a bipolar membrane

which contains a cation-exchange membrane on one side and an anion-exchange membrane on the other side. Bipolar membranes are widely used in industry for chemical separation and production of acids and bases. Prior works have shown the rectification effect in nanofluidic diodes fabricated by modifying the surface chemistries of conical nanopores and nanochannels. In this work, we have presented a new method to create nanofluidic diode using different solid oxide materials. Standard semiconductor processing methods allow the oxide regions to be well defined and physically robust. The device exhibits rectifying factor as high as 330 within small voltage biases. The ion transport behavior at different bath concentrations has been investigated and qualitatively matches with the theoretical calculations. We suggest that with the solid oxide nanofluidic diodes, one can integrate them with microfluidic devices to perform chemical separation processes or electrolyte pH control in a microscale system.

REFERENCES

[1] H. Daiguji, Y. Oka and K. Shirono, *Nano Letters*, 2005, **5**, 2274-2280.

[2] B. Lovrecek, A. Despic and J. O. M. Bockris, *Journal of Physical Chemistry*, 1959, **63**, 750-751.

[3] K. N. Mani, *Journal of Membrane Science*, 1991, **58**, 117-138.

[4] R. Simons and G. Khanarian, *Journal of Membrane Biology*, 1978, **38**, 11-30.

[5] R. Karnik, K. Castelino, C. H. Duan and A. Majumdar, *Nano Letters*, 2006, **6**, 1735-1740.

[6] R. Karnik, C. H. Duan, K. Castelino, H. Daiguji and A. Majumdar, *Nano Letters*, 2007, **7**, 547-551.

[7] I. Vlassiouk and Z. S. Siwy, *Nano Letters*, 2007, **7**, 552-556.

[8] Parks, G. A., ISOELECTRIC POINTS OF SOLID OXIDES SOLID HYDROXIDES AND AQUEOUS HYDROXO COMPLEX SYSTEMS. *Chemical Reviews* 1965, 65, (2), 177-&.

[9] Henrich, V. E.; Cox, P. A., *The surface science of metal oxides*. Cambridge University Press: Cambridge ; New York, 1994; p xiv, 464 p.

Chapter 5

Ion Transport in Heterogeneous Nanochannels – Bath Sidewall Effect

5.1 Introduction

Ion transport phenomena in nanofluidic devices reported to date focus on the effect of the channel surface charge. It is found that when the channel size is comparable to the Debye length or the bath ion concentration is smaller than the nanochannel's fixed charge density, the ion conductance of nanochannels is governed by the channel surface charge and independent of bath ion concentrations. However, the effect of the surface charge outside nanochannels on ion transport has been overlooked.

The issue of nanochannel entrances has rarely been discussed. It was reported that the surface charge density outside the nanochannel at the bath surface can affect the ion conductance at the channel access.[1] Higher bath surface charge outside the nanochannel gives lower access resistance. The physics behind it can be explained by applying the

simplified model introduced in the previous chapter. In brief, basically the access resistance is induced by the depletion of ions at a nonequilibrium state.

Depending on the bias polarity applied to the nanochannel, the unbalanced cation-anion ratios of the ionic solutions in the bath and the nanochannel induce accumulation or depletion of ions at the entrance of nanochannel. The depletion of ions at the channel access produces an additional series resistance therefore reduces the total ion conductance. The so-called channel polarization is manifested at low ion concentrations. This is because at low concentration, a charged nanochannel can induce much higher cation-anion ratio comparing to that in the bath, which is close to unity. If the cation-anion ratios in both sides are very different, the polarization effect gets more severe from the discussion in Chapter 3. Hence, more ions can be depleted in one side of nanochannel access, resulting in high access resistance.

The cation-anion ratio in the bath area is approximately unity because there is no fixed charge in it. At the bath boundary, however, the fixed charges at the boundary induce more counter-ions and the cation-anion ratio nearby is no longer unity. The charges on bath surfaces should be taken into account because it is the cation-anion ratios near the bath-nanochannel boundary that involves in the nanochannel polarization.

Greater bath surface charge density reduces the difference of the cation-anion ratios inside and outside the nanochannel and hence alleviates the extent of ion accumulation and depletion. As a result, the access resistance decreases.

In this chapter, we investigate the nonlinear ion transport in heterogeneous oxide nanofluidic devices which contains opposite surface charge polarities outside the nanochannel with respect to that inside the nanochannel. Such surface charge near the entrance forms a parasitic fluidic diode at each channel access. For convenience, we name it a parasitic or access diode to distinguish it from the intrinsic nanofluidic channel diode which is formed by heterogeneous surface charge polarities inside the nanochannel. With two parasitic access diodes located at the two channels entrances connecting back to back, the nanofluidic device forms an equivalent pnp or npn diode. The I-V characteristics show that such access effect is observable at low ion concentrations at which the Debye length is comparable to the channel size, but weakened with increased concentrations.

5.2 Fabrication of Al_2O_3 nanochannels

As described in the previous chapter, aluminum oxide (Al_2O_3) is the oxide material chosen to provide the positively charged surfaces in heterogeneous nanofluidic devices.

To make an Al_2O_3 nanochannel, a 5 nm thick Al_2O_3 thin film was first patterned on a glass substrate to function as the bottom surface of the nanochannel. The Al_2O_3 thin film was formed by photolithography, e-beam evaporation using an Al_2O_3 source at about 7×10^{-6} Torr and followed by a lift-off. An amorphous silicon sacrificial layer was than deposited on top by sputtering and patterned into 3 μm wide and 60 μm long channels. The thickness of the a-Si layer determines the height of nanochannels. Here the thickness of the a-Si was targeted at 20 nm. To form the Al_2O_3 ceiling on the nanochannel, the same process was used to cover the top of the a-Si channel patterns. The Al_2O_3 patterns on the bottom and top had the same geometry and were well aligned. A 5 μm thick PECVD oxide was deposited at 200^{o}C on top of the sample to form the SiO2 channel surface as well as the physical structure of the device. To form contact holes, we etched several holes through the PECVD oxide layer and the top Al_2O_3 layer by high density plasma etch until the a-Si sacrificial layer was exposed. XeF_2 etch was performed to remove a-Si sacrificial layers, resulting in open nanochannel structures. After this, a PDMS microfluidic channels cast from predefined SU-8 patterns was aligned and bonded on the nanofluidic device with the thin PDMS glue layer introduced in the previous chapters. After cured at 65^{o}C for 4 hours and an O_2 plasma treatment, the device is ready for test.

5.3 Bath side-wall effect in heterogeneous nanochannels

5.3.1 Characterization of heterogeneous Al_2O_3 nanochannels

To characterize the surface charge density of Al_2O_3 surfaces, the ion conductance of Al_2O_3 nanochannels were measured under varied KCl concentrations. However, it was found that the I-V curves of the Al_2O_3 nanochannels are nonlinear except at high concentrations. They are symmetric but the currents saturate at high voltages. The result was not expected because the Al_2O_3 thin films were uniformly deposited around the nanochannel. The nanochannel having uniform fixed charge distribution should give a linear I-V characteristic as it occurs in a homogeneous silica nanochannel. Figure 5.1(a) shows the I-V characteristics measured at low KCl concentrations of 0.01 mM, 0.1 mM and 1 mM. The current levels for 0.1 mM and 0.01 mM KCl concentrations are very alike. Similar to the case of homogeneous silica nanochannels, this is because in this concentration regime in which the bath concentrate is less than the channel fixed charge density ($c_b < f/2$) or the Debye length is comparable or greater than the channel size ($\lambda_D \geq h/2$), the ion conductance is governed by the surface charges in the nanochannel instead of the bath concentrations. The currents saturate when the applied voltage biases exceed a certain level. Higher concentrations need higher voltage biases to reach current

saturation. Based on the observation, we reasoned the cause of the phenomena as following.

1. The current saturation depends on the voltage biases and the ion concentrations so it should be related to the ion depletion in the device.
2. Since the current is symmetric, the phenomena must be due to the symmetric surface charge distribution in the device.

Although the Al_2O_3 nanochannel we fabricated has homogeneous surface charge polarity and density inside the nanochannel, in reality, the surfaces outside the nanochannel are all silica as illustrated in Figure 4.3(b). The heterogeneous surfaces near the entrance of nanochannel may affect the ion transport.

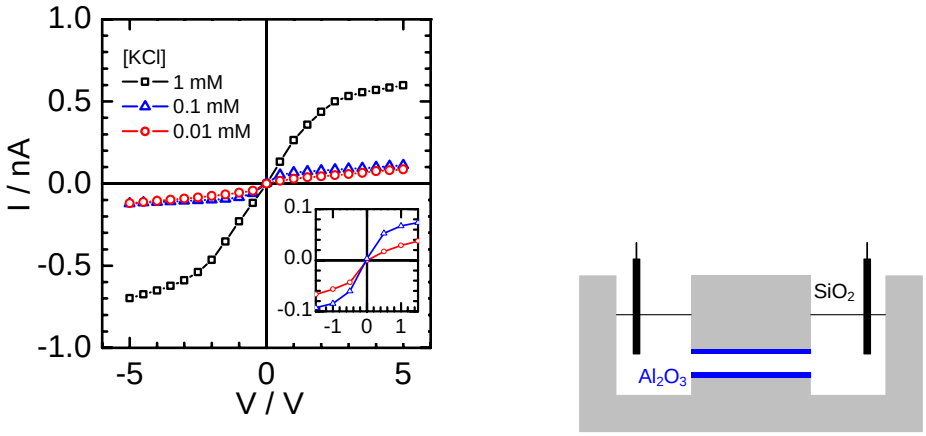

(a) (b)

Figure 5.1 (a) Experimental I-V characteristics of an Al_2O_3 nanochannel measured at 1 mM, 0.1 mM and 0.01 mM KCl concentrations. (b) The Al_2O_3 nanochannel device has homogeneous Al_2O_3 surfaces inside the nanochannel and silica surfaces outside the nanochannel.

To investigate if the surface charge immediately outside the nanochannel entrances can cause the nonlinear ion transport, we coated the silica sidewall right outside the two entrances of the nanochannel by using an angled (about 70^{o}) e-beam evaporation of a 4 nm thick Al_2O_3 thin film twice as depicted in Figure 5.2. The resulting I-V curves show that the coverage of Al_2O_3 surface outside the nanochannel makes the ion transport become linear as shown in Figure 5.3(c) and (d). The significant change in the ion transport behavior implies that the surface charge outside nanochannel does play an important role in the ion conductance of nanochannels.

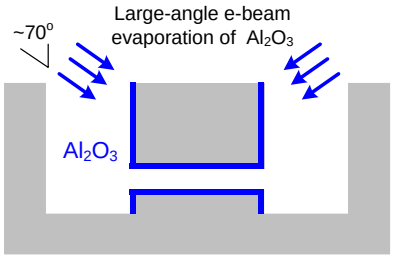

Figure 5.2 The silica surfaces outside the nanochannel are covered by a thin Al_2O_3 layer by large-angle e-beam evaporation of Al_2O_3 to form a complete homogeneous Al_2O_3 nanochannel. Note that the schematic is not drawn to scale. In the real device the two baths are much longer than the nanochannel.

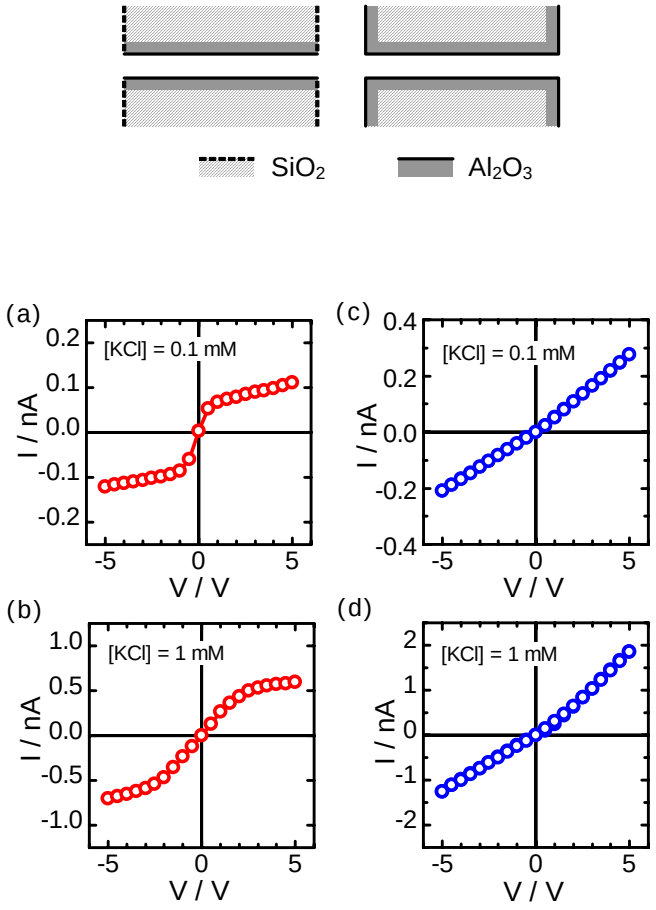

Figure 5.3 Experimental I-V characteristics of the original Al_2O_3 device with silica bath side-wall measured at (a) 0.1 mM and (b) 1 mM KCl concentrations; and the modified device that has both nanochannel and bath side-walls made of same Al_2O_3 and measured at (c) 0.1 mM and (d) 1 mM.

Now that a complete homogeneous Al_2O_3 nanochannel can be achieved by covering the silica bath side-wall with Al_2O_3, we can avoid the nonlinear transport effect and measure the surface charge density of Al_2O_3 surface in the nanochannel. Figure 5.4 summarized the ion conductance of a homogeneous Al_2O_3 nanochannel obtained at

varied KCl concentrations ranging from 10^{-5} M to 1 M. By fitting the experimental data, the channel height *h* is estimated to be about 19 nm which is very close to the targeted 20-nm. The surface charge density is evaluated to be about 1.27 mC/m^2 which is the same order of magnitude as the effective surface charge (2.10 mC/m^2) deduced from the electroosmotic mobility.

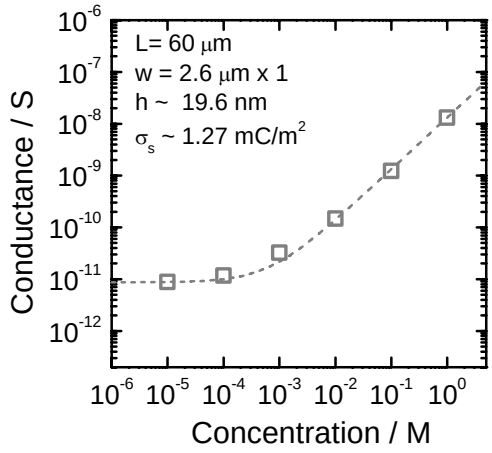

Figure 5.4 Measured ionic conductance of homogeneous Al_2O_3 nanochannel at varied KCl concentrations. By fitting the data with theoretical calculation, the channel height is estimated to be 19 nm and surface charge density about 1.27 mC/m^2.

5.3.2 Effect of bath sidewall surface charge on the ion transport

The previous experiment corroborate that it is the opposite surface charge polarities outside the nanochannels with respect to that inside the nanochannel induce the nonlinear ion transport phenomena. But why does it behave like that? To explain it, we can treat the heterogeneous structure that consists of a positively charged Al_2O_3 nanochannel and a

nearby negatively charged SiO_2 bath surface as special kind of nanofluidic diode. As described before, similar to a bipolar membrane which is composed of a positively charged cation-exchange membrane and a negatively charged anion-exchange membrane, the nanofluidic device containing two different surface charge polarities can form a nanofluidic diode (Figure 5.5(a)). Now imagine the boundaries of the negatively charged silica channel start to open up till they orient 90^o with respect to the fixed positive-charged Al_2O_3 channel, they form the entrance to the positively charged Al_2O_3 nanochannel (Figure 5.5(b)). The property of the heterogeneous nanofluidic diode should be preserved in this transformation. We name this kind of nanofluidic structure as a nanofluidic access diode, which is symbolized by an empty diode to distinguish it from the nanofluidic channel diode symbolized by a solid diode in Figure 5.5(a). As described before, depending on the applied bias polarities along such an heterogeneous nanochannel, ions in the device can be accumulated or depleted resulting in distinct ion conductances. The ion rectifying effect relies on the heterogeneous surface charge distribution. It is known that the electrostatic interaction between surface charges and mobile ions decays with the increase of distance. In the case of heterogeneous channel access, however, the surface charges on the bath side-wall can still affect the ions nearby the channel entrance as long as the Debye screening length from the side-wall is long

enough to reach the channel entrance. But because of the increased distance, the electrostatic force induced by the side-wall surface charges will not be as strong as that by the channel surface charges.

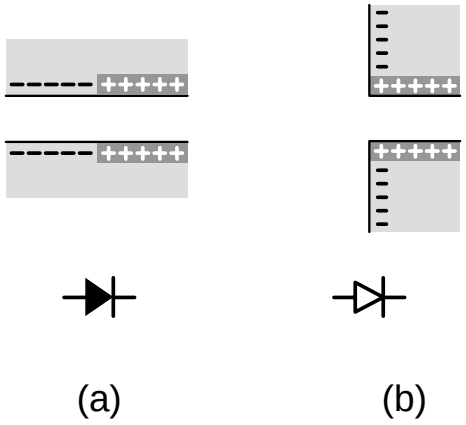

Figure 5.5 Heterogeneous surface charge distributed in a nanochannel can form (a) a nanofluidic channel diode symbolized by a solid diode or (b) a nanofluidic access diode at the channel entrance which is symbolized by an empty diode

At low ion concentrations, the Al_2O_3 nanochannel with silica bath side-walls can be treated as an equivalent circuit with two nanofluidic access diodes, D1 and D2, connecting back to back (Figure 5.6). When a large positive voltage (Vd > 0) is applied to the right side with the left side grounded, D1 is forward biased and has high ionic conductance while D2 becomes reversed biased and has low ionic conductance. In this case the ionic current passing through nanochannel is restricted by the highly-resistive D2,

so the increase of Vd will not induce more ionic current. As a result, the current saturates. Since the device is symmetric, a large negative Vd yields a symmetric result. At small Vd, D1 and D2 do not reach forward or reverse bias regime so the ion current still responses linearly to Vd.

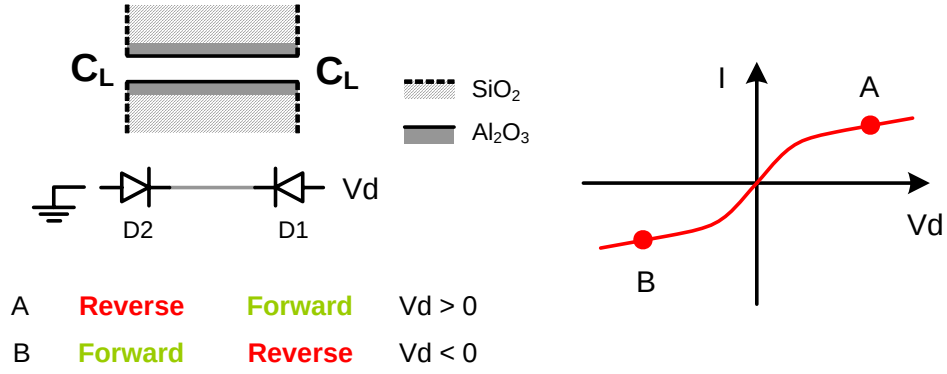

Figure 5.6 Al_2O_3 nanochannels with SiO2 bath side-wall functions as two nanofluidic access diodes, D1 and D2, connecting back-to-back. The current saturates at large |Vd| because one of D1 and D2 will be reversed biased and make the current path resistive.

To better understand the nonlinear ion transport effect, we calculated the potential profiles and the current density by solving the Poisson-Nernst-Planck (PNP) equations of the system shown schematically in Figure 5.7(a). The same device geometry (channel height = 20 nm, channel length = 10 μm, and reservoir size = 2μm × 2μm) and boundary conditions were used as before except that the charge densities of the nanochannel

surfaces and the bath sidewalls were set to be 4.5 mC/m^2 but with opposite charge polarity, i.e. $\sigma_{ch} = - \sigma_w$. Figure 5.7(b) and (c) are the calculated ion concentration profiles in the nanochannel devices containing 0.1 mM and 1 mM KCl concentrations under a bias of 5 V to the right bath (Vd = 5V). Note that the concentration-axis is in log scale. The profiles show that under such voltage bias, both cations and anions are depleted at the left entrance but accumulated at the right entrance. The depletion of ions at the left entrance increases the resistance of the ion current path. This result agrees with our access diode model described previously: when Vd is positive, the left access diode is reverse biased (turned-off) while the right forward biased (turned-on).

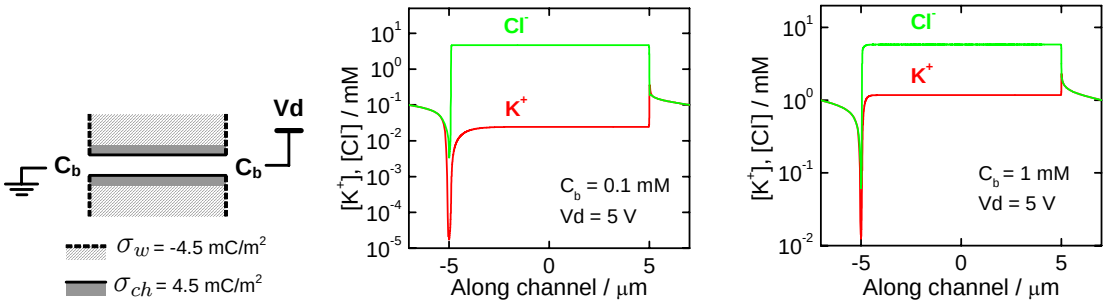

(a) (b) (c)

Figure 5.7 (a) Schematic of the device structure and bias arrangement. (b) and (c) are calculated ion concentration profile along an Al_2O_3 nanochannel (between -5 and 5 μm) with SiO_2 bath side-wall for different bath concentrations c_b = 0.1 mM and 1mM. The concentration-axis is plotted in log scale.

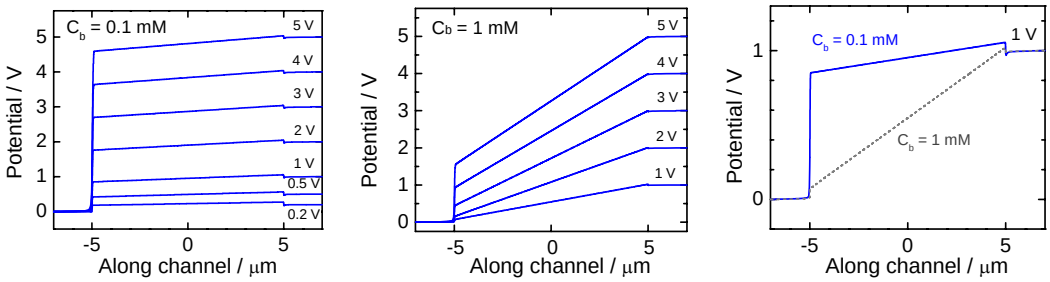

(a) (b) (c)

Figure 5.8 Calculated potential profile along an Al_2O_3 nanochannel (between -5 and 5 μm) with SiO_2 bath sidewall under varied applied voltage at different bath KCl concentrations (a) 0.1 mM and (b) 1 mM. Two potential profiles from different bath concentrations with the same 1 V bias are compared in (c).

The reduction of the ion concentration at the channel entrance reflects that there should be a big voltage drop across the channel entrance. Figure 5.8 shows the calculated potential profiles under varied applied voltage biases with 0.1 mM and 1 mM bath ion concentrations. It can be seen in Figure 5.8(a) that at c_b = 0.1 mM most of the applied voltage drops at the left channel access under every applied bias. The access voltage drop rises with applied voltage. But the potential gradients in the nanochannel region only slightly respond to the applied bias. However, when the bath concentration increases to 1 mM shown in Figure 5.8(b), the access voltage drops are significantly reduced resulting in higher potential gradient in the channel region. By comparing the two potential profiles containing different bath concentrations at the same bias, we can see that the access

voltage drop is much higher at low bath concentration. The effect stems from the fact that at low ion concentrations, the Debye length is large enough such that the electrostatic effect from the sidewall surface charges can cover the channel entrance. The theoretical I-V curves for two different bath concentrations are plotted in Figure 5.9(a) and (b). The current densities were calculated from $I = q(\mu_{\mathrm{K}}\, n_{\mathrm{K}} + \mu_{\mathrm{Cl}}\, n_{\mathrm{Cl}})\Delta V/L \cdot h$, where ΔV is the voltage drop in the nanochannel and h, the channel height, is 20 nm. Although the geometric size and the value of surface charge density are different from the real device, the calculated and experimental results show the same trend of current saturation at high voltage bias and the weaker saturation effect for the case of 1 mM bath concentration.

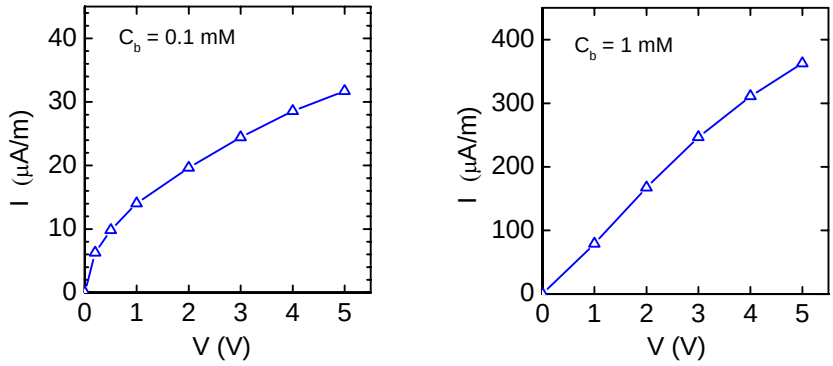

(a) (b)

Figure 5.9 Calculated I-V curves of an Al_2O_3 nanochannel with SiO_2 bath side-wall at different bath concentrations, (a) 0.1 mM and (b) 1 mM.

To figure out how the sidewall surface charge σ_w affects the ion conductance in the nanochannel, we did calculation for the device with varied σ_w with channel surface

charge σ_{ch} fixed at 4.5 mC/m^2. Figure 5.10(a) and (b) summarize the calculated potential profiles and ion concentration distributions near the left channel entrance for different surface charge ratios σ_w/σ_{ch} at bath concentration of 0.1 mM under the bias of 5 V. The potential profile in Figure 5.10(a) shows that when the surface charge polarity of the bath sidewall is opposite to that in nanochannel (i.e. $\sigma_w/\sigma_{ch} < 0$), most of the applied voltage drops across the channel entrance and the electric field in nanochannel is relatively weak. In the case of $\sigma_w/\sigma_{ch} > 0$, the voltage drops are drastically lowered at the channel entrance. Part of the voltage drop extends into the bath region implying that the bath region becomes more resistive. More positive or negative σ_w does not give much more difference. Figure 5.10(b) shows the ion concentration distributions in more detail near the channel entrance (x = -5.0 μm) for different surface charge density ratios σ_w/σ_{ch}. It is found that when surface charge polarities of bath sidewall and that of nanochannel are opposite ($\sigma_w/\sigma_{ch} < 0$), the ion depletion takes place inside the nanochannel (x > -5 μm) and the concentrations in the bath region reach C_b in a short distance from the channel entrance. This kind of ion distribution can be observed as well in a reverse-biased nanofluidic channel diode which has a depletion region at the boundary of the positive-charged and negative-charged regions. However, for the device having $\sigma_w/\sigma_{ch} > 0$, the ions deplete in the bath region rather than in the nanochannel region. It is the ion

depletion in bath region produces the so-called access resistance. The access resistance is the series resistance connecting to nanochannel in series and cannot be neglected in the experiment as long as the probing electrodes are placed some distance away from the channel entrances. It is also interesting to know that when the side-wall charge is neutral ($\sigma_w = 0$), the ion depletion effect is as obvious as the case of $\sigma_w/\sigma_{ch} < 0$. The results suggest that the side-wall surface charge must be the same polarity as the channel surface charge to obtain a high ion conductance. The ion current densities are calculated for different σ_w/σ_{ch} ratios in Figure 5.11. Because the nanochannel is positively charged, the total ion currents are mostly contributed by the anion (Cl^-) currents. The ion current increase significantly when the polarity of side-wall surface charge switches from negative to positive. The effect inspires us to think that it may be possible to create an ion switch device to control ion flows by switching the polarity of the side-wall surface charge, e.g. in an electrical manner. However, the device will only function well at the relatively low ion concentrations such that the Debye length is comparable to the channel size.

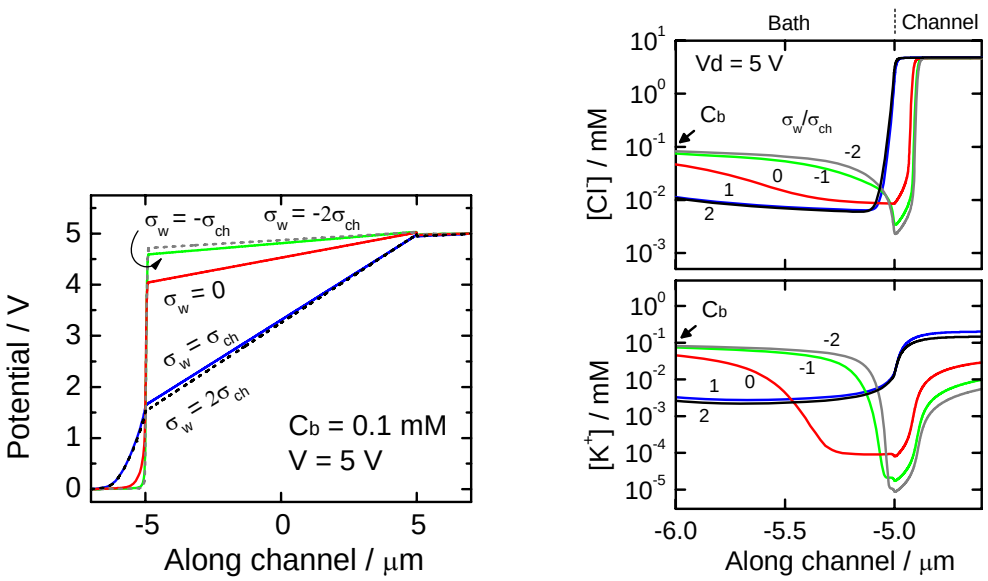

Figure 5.10 Calculated (a) potential profile and (b) zoom-in ion concentration distributions of a nanochannel device containing different sidewall to channel surface charge ratios, σ_w/σ_{ch} = -2, -1, 0, 1, 2. σ_{ch} is fixed at 4.5 mC/m^2.

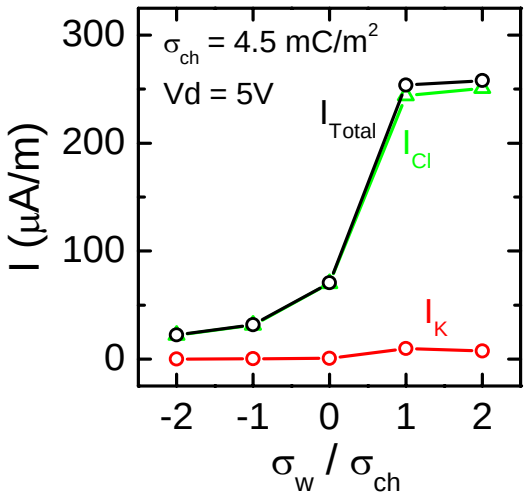

Figure 5.11 Calculated ion current densities of a nanochannel device containing different sidewall to channel surface charge ratios, σ_w/σ_{ch} = -2, -1, 0, 1, 2. σ_{ch} is fixed at 4.5 mC/m^2.

5.3.3 Effect of bath sidewall surface charge on ion transport through concentration gradients

It is known that the access diode formed by the heterogeneous surface charge on the bath sidewalls and nanochannel surface can work at low ion concentration. It would be interesting to observe the ion transport behavior in the device containing asymmetric bath concentrations. Figure 5.12(a) schematically presents the device structure and the measurement setup. Voltage bias Vd is applied in the right bath (C_H) which contains 100 mM KCl solution while the 0.1 mM KCl in the left bath (C_L) is grounded. This kind of ion concentration setup gives a different equivalent circuit from the previous case shown in Figure 5.6. Because the 100 mM ion concentration in the C_H side is high enough to shield the surface charges on the bath side-wall and the nanochannel, the parasitic nanofluidic access diode D1 used to be in the right channel entrance disappears. However, the left C_L side has low ion concentration which allows the surface charges on the bath side-wall and nanochannel to have enough impact on the mobile ions at the channel entrance. Therefore, the diode D2 still exists. As a result, the property of the nanochannel device can be equivalently treated as a single nanofluidic access diode D2 located on the C_L side. The equivalent circuit model was proved to be right by the experimental I-V characteristics displayed in Figure 5.12. A strong rectification effect

was observed in the I-V curve. The rectifying factor (I_{on}/I_{off} at -3 and 3 V) is about 18. When the Vd is positive, the access diode D2 is reversed biased leading to a lower ion conductance. On the contrary, when the Vd is negative, D2 is forward biased and the nanochannel has higher conductance.

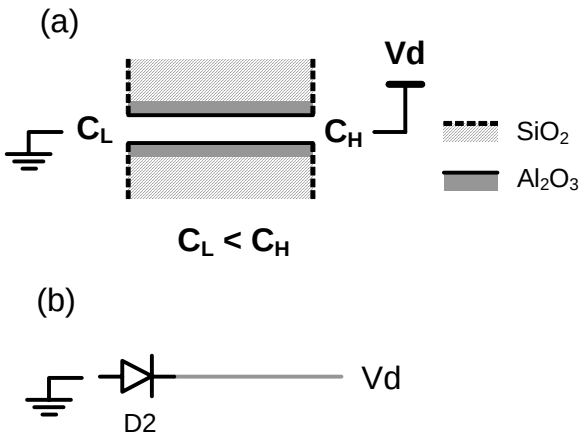

Figure 5.12 (a) Schematic of a heterogeneous Al_2O_3 nanochannel and the measurement setup. The bath concentration in the left side C_L is smaller than C_H in the right side. (b) Equivalent circuit of the nanofluidic device.

The mechanism of the rectifying effect here is different from the case of homogeneous nanochannels containing concentration gradient. To compare them, a complete homogeneous Al_2O_3 nanochannel, which was made by large-angle side-wall evaporation to cover the silica bath side-walls, containing asymmetric bath concentrations was measured. Similar to the previous measurement setup, the bias Vd is applied on the C_H side (100 mM KCl) with the C_L side (0.1 mM KCl) grounded (Figure

5.14(a)). As shown in Figure 5.14(b) the I-V curve displays rectifying effect with the rectifying factor of about 7 but has opposite rectification polarity to the heterogeneous Al_2O_3 nanochannel—in the heterogeneous nanochannel, the forward bias takes place at Vd < 0 while in the homogeneous nanochannel it happens at Vd > 0. Apart from the difference in rectification polarity, the reverse-bias current in the heterogeneous nanochannel is smaller than the homogeneous counterpart. These evidences suggest the surface charges on the bath side-walls affect the ion transport through the concentration gradient in nanochannels.

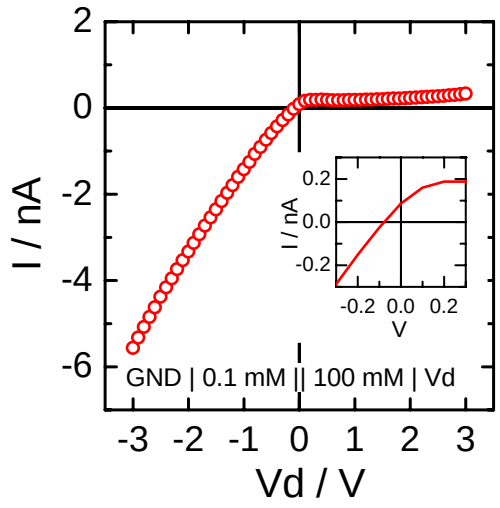

Figure 5.13 Measured I-V characteristic of the nanochannel device which contains Al_2O_3 nanochannels and SiO_2 bath sidewalls and was placed in asymmetric bath concentrations. Voltage bias Vd was applied on the bath containing 100 mM KCl solution while the bath with 0.1 mM KCl was grounded.

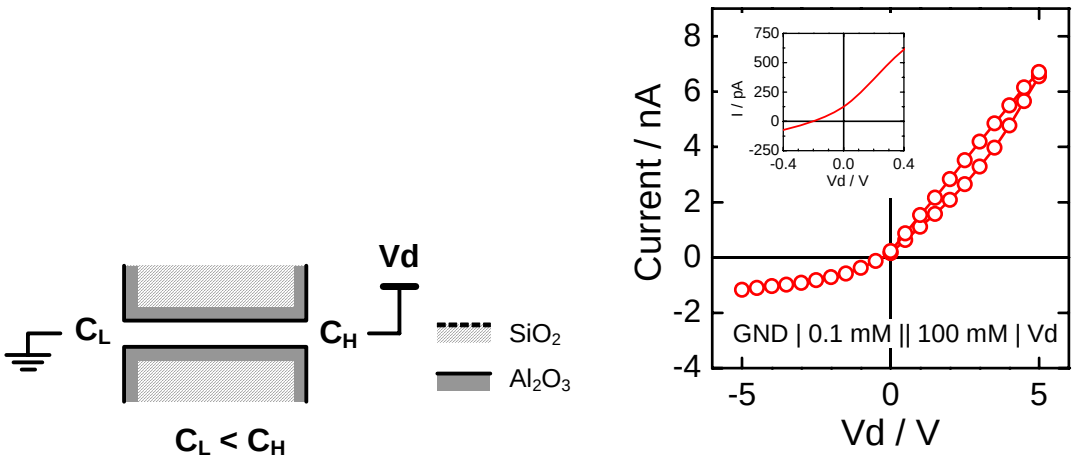

(a) (b)

Figure 5.14 (a) Schematic of a homogeneous Al_2O_3 nanochannel and the measurement setup. The bath concentration in the left side C_L is greater than C_H in the right side. (b) Measured I-V curve of the homogeneous Al_2O_3 nanochannel.

To better understand the different ionic rectification effects shown in Figure 5.13 and 16, we calculated the ion concentration distributions and potential profiles in both heterogeneous and homogeneous Al_2O_3 nanochannels placed between 0.1 mM and 100 mM KCl solutions in each bath. The rectification effect of the homogeneous nanochannels with concentration gradient has been treated in detail in the previous chapter. Basically, ionic rectification can be observed when the nanochannel has charged surfaces and contains a concentration gradient along it to produce asymmetric cation-anion ratios at the two channel ends. The uneven cation-anion ratios can induce ion depletion or accumulation inside the nanochannel corresponding to the applied

electric fields. Take the homogeneous Al_2O_3 nanochannel shown in Figure 5.15(a) for instance, in this positively charged nanochannel, the ions are depleted when the electric field is applied along the concentration gradient (Vd = -5 V) but accumulated at the opposite bias polarity (Vd = 5V). The strength of the electric field at positive Vd is smaller than that at negative Vd. However, much more ions are accumulated at positive Vd. As a consequence, the homogeneous Al_2O_3 nanochannel has higher ion conductance at positive Vd at which the electric field is applied against the concentration gradient.

A reverse result can be obtained when the nanochannel has opposite surface charge polarity, because the kind of counter-ions in the nanochannel is different. Therefore, as shown in Figure 5.15(b) the rectification polarity of a homogeneous silica nanochannel will be opposite to that of a homogeneous Al_2O_3 nanochannel. The experimental result of the rectifying effect in silica nanochannels has been reported in the previous chapter. The result proves that the polarity of nanochannel surface charge can be examined by measuring the rectification polarity in the nanochannel device with concentration gradient.

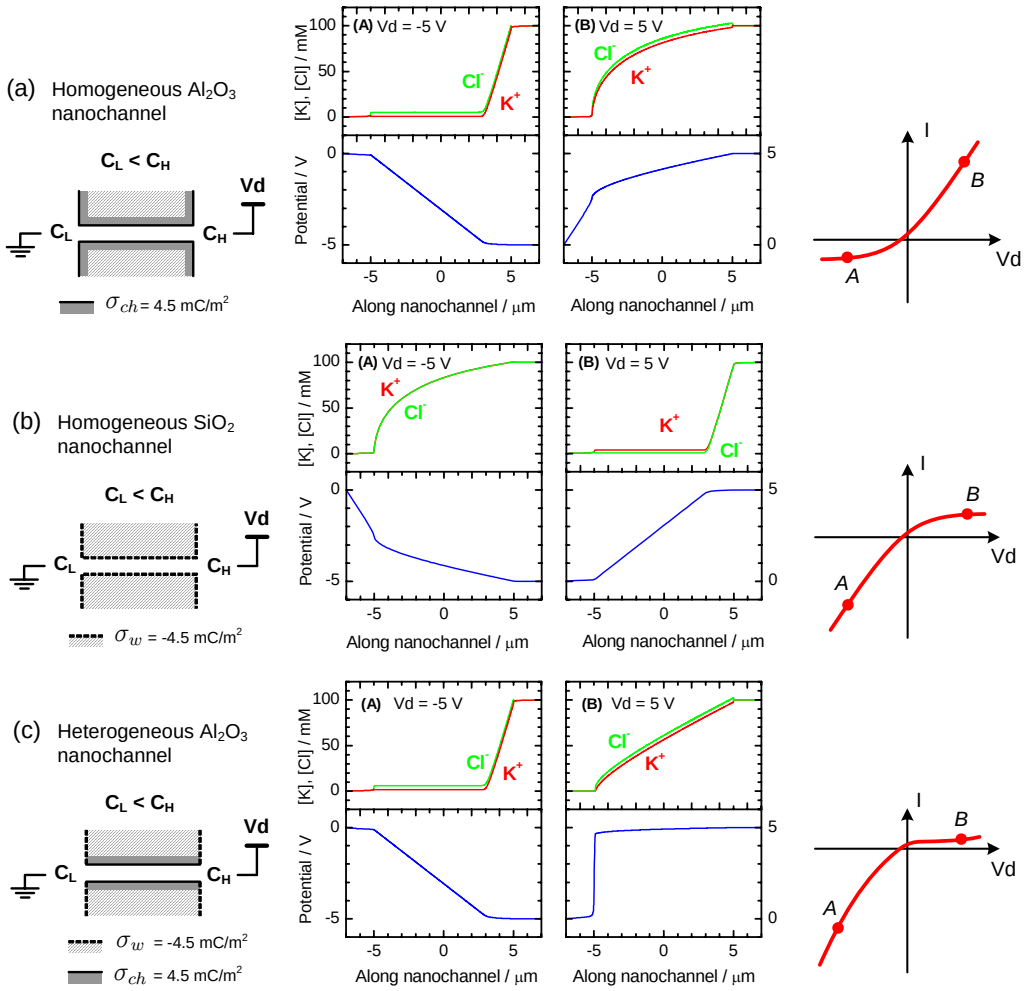

Figure 5.15 Calculated ion concentration distribution and potential profiles along three different nanochannel devices with concentration gradient under the bias of Vd = -5 V and 5 V. The types of nanochannel device are (a) homogeneous, positively charged Al_2O_3 nanochannel, (b) homogeneous, negatively charged SiO_2 nanochannel, and (c) heterogeneous Al_2O_3 nanochannel with SiO_2 bath sidewalls. The bias Vd is applied at the high concentration C_H side (100 mM KCl) while the C_L side (0.1 mM) is grounded.

Although a heterogeneous and a homogeneous Al_2O_3 nanochannel have the same surface charge polarity in the nanochannel region, they exhibit very different I-V characteristics. Figure 5.15(c) is the case of heterogeneous nanochannel with positively

charged nanochannel and negatively charged bath sidewalls. It shows that at Vd = 5 V, most of the applied voltage drops across the channel entrance in the C_L side, resulting in a weak electric field in the nanochannel. Because of the weak electric field, the ion concentrations in the nanochannel do not change too much from those at the equilibrium state. As a result, the drift ion current turns out to be very small. However, when Vd = -5 V, the electric field inside the nanochannel is significantly increased. Although the ions inside the nanochannel are depleted, the concentrations are still kept at a certain level. The total migration current is relatively large.

5.4 Conclusion

We have introduced solid oxides as the material for heterogeneous nanochannels and studied the nonlinear ion transport behavior in the device. The surface of different solid oxides exhibits distinct pI and can produce different surface charge polarities. By using them, we can create a well defined surface charge distribution in nanochannels and hence produce functional surface-charge governed ion transport. In this chapter, we have investigated the effect of the surface charge at the bath sidewalls on the ion transport in nanochannels which has not been treated before. It has been proved that the effect cannot

be ignored at low bath concentrations and under high applied voltage biases. When the bath side-wall and nanochannel have different surface charge polarities, the channel access works as a parasitic nanofluidic diode and can cause a huge series resistance under a certain bias polarity. Through theoretical calculation, it has been found that the nanochannel conductance is sensitive to the surface charge polarity of bath side-wall. The result implies that the physics of nanofluidic devices cannot be singled out without considering the effect from the nanofluidic–microfluidic interface.

REFERENCES

[1] Aguilella-Arzo, M.; Aguilella, V. M.; Eisenberg, R. S. *European Biophysics Journal with Biophysics Letters* **2005,** 34, (4), 314-322.

Chapter 6
Active Transport of Biomolecules in Open Nanochannels Powered by Motor Proteins

6.1 Introduction

There has been increasing interests among the scientific community to explore natural biomaterials and biomolecules for engineering applications. Kinesins, a family of biomolecular motor proteins, are nanoscopic engines that utilize the free energy from the hydrolysis of ATP molecules to move along microtubules (MTs).[1] Within cells, the kinesin-microtubule system is responsible for intracellular transport of proteins, organelles and vesicles throughout the cytosol.[2] This system can also be exploited in *in vitro* environments to achieve certain useful functionalities, which may pave the way for complex artificial micro- and nanosystems. One of the important examples is nanoscale transport in which microtubules carrying designated target molecules glide along kinesin-coated tracks towards a destination, [3] which can form the basis of novel chemical transport and separation systems. To produce controlled microtubule transport,

it is necessary to confine their motion along pre-defined protein tracks by, for instance, selective patterning of kinesin motor proteins, physical confinement structures, or a combination of both. In this regard, a recently developed nanoscale protein patterning technique offers great potential.[4] Several previous studies proposed to control microtubule transport in microscale tracks made of or generated by lithographically patterned photoresist barriers.[5,6,7] However, high guiding efficiency has not been achieved. The mechanisms of microtubule guiding in such artificial tracks have been analyzed in several papers.[8,9] The reason for the observed low guiding efficiency and high MT detaching rate can be explained by the fact that in microscale tracks, the microtubules tend to reach the track barriers at large approaching angle, which often leads to MT escaping from kinesin tracks or permanently stalled at the site of contact with the barrier. These results imply that decreasing track width should significantly enhance the efficiency of microtubule guidance. Prior work by Dennis *et al.* has demonstrated that the motion of microtubules can be directed in oriented nanoscale protein tracks formed by rubbing a poly(tetrafluoroethylene) (PTFE)-coated glass substrate.[10] However, rubbed topographies lack micro- or nanoscale design and the barrier height, typically less than 30nm, was too small to prevent kinesin proteins from projecting out over the barriers and frequently switching to adjacent tracks. Also, the low

barrier height provides poor physical confinement for the gliding MTs. As a result, MTs continue to move randomly on the substrate.

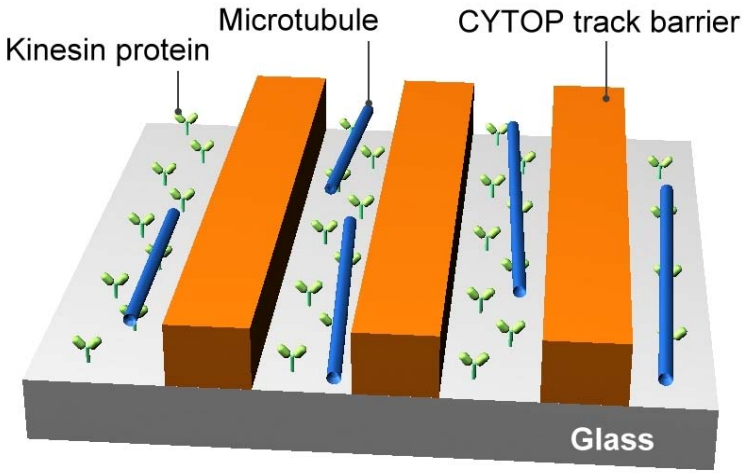

Figure 6.1 Kinesin motor proteins immobilized within CYTOP nanotracks on a glass coverslip. Microtubules propelled by the kinesin motors are physically confined by the CYTOP track barriers, leading to precision guided transport along the nanotracks.

To solve all these problems, we have developed a very effective method to achieve highly efficient guiding of MT transported by kinesin motors that are immobilized within polymer nanotracks created by nanoimprint lithography (NIL). As illustrated in Figure 6.1, nanoscale protein tracks constrained by polymer barriers prevent the gliding microtubules from swaying and compel the microtubules to approach the track edge at glancing angles, thus restraining them from moving out of the tracks. Furthermore, the barriers are chemically modified to have protein-nonadhesive properties, which

effectively prevent microtubules from either climbing up the barriers or randomly gliding over the top surface of the barriers. By combining these two strategies, we have obtained high-efficiency and high-density of controlled microtubule transport. Microtubule motility assays examined by fluorescence microscopy showed that high densities of microtubules glide exclusively (close to 100%) along the imprinted nanotracks. The average gliding distance of microtubule before detaching from the surface is about 2.5 mm.

We developed several novel techniques for forming the polymer nanotracks to guide the motion of kinesin-propelled microtubules. For our experiments we used a bacterially expressed kinesin motor, NKHK560cys. Details on the biochemical techniques used for kinesin and MT preparation can be found in the experimental section. The nanotracks on glass substrates were fabricated through direct nanoimprinting of a cyclized perfluoropolymer called CYTOP^{TM} (**Asahi Glass Co., Tokyo, Japan**), followed by CYTOP surface hydrophobicity enhancement using sulphur hexafluoride (SF_6) plasma etching. The CYTOP track barriers are further treated with a Pluronic® triblock copolymer that forms a Poly(ethylene oxide) (PEO) monolayer on its surface, which dramatically reduces protein adsorption. Then a simple flow cell is constructed and filled with kinesin proteins. Kinesin protein is preferentially adsorbed on the glass surface, but

not on modified CYTOP barriers, and therefore forms nanotracks that propel microtubules exclusively along the patterned direction.

6.2 Materials and fabrication of nanotracks

As illustrated in Figure 6.2(a), CYTOP gratings were created using nanoimprint lithography (NIL). NIL provides the capability of creating large-area nanoscale patterns with high yield, high throughput and high reproducibility.[11] CYTOP thin films are especially suitable as an imprinting material: the glass transition temperature (T_g) of CYTOP (105 ^{o}C) is well suited for the imprinting process and CYTOP has very low surface energy which greatly facilitates the demolding process after NIL. These key material properties lead to very low defects in the imprinted CYTOP nanostructures. Low defect density is important to obtain controlled MT transport over long distances. For NIL fabrication, a large area grating made of Si with 350nm line-width-and-spacing and 500nm in depth was used as a mold. The mold was treated with a surfactant, perfluorodecyltrichlorosilane **(Lancaster Synthesis, Windham, NH)** to provide a low energy surface to facilitate the demolding process. The substrate we used, Corning coverslip (**Corning, NY**), was cleaned by our "standard clean" process, involving a

10-minute dip in Piranha solution (H_2SO_4 : H_2O_2 = 2 : 1), a 10-minute rinse in deionized water, a 20-second dip in dilute HF (HF : H_2O = 1 : 20) and another 10-minute rinse in deionized water. After dehydration of the coverslip, the material to be imprinted, 370nm thick CYTOP, was spun onto a coverslip followed by a 10 minute of baking at 50 ^oC and 30 minutes of curing at 180^oC. The mold and substrate were then brought into physical contact at 150^oC, and a pressure of 35 Kg/cm^2 was applied for 5 minutes followed by subsequent cooling. After mold separation, SF_6 reactive ion etching (RIE) (SF_6 gas flow = 20 sccm, pressure = 20 mTorr, power = 120W, self DC bias = 275V) was applied to remove the CYTOP residuals in the trench regions to expose the glass surface. The CYTOP etching rate is about 130 nm/min. Finally, the whole CYTOP grating chip is dipped in ammonia hydrogen peroxide mixtures (NH_4OH : H_2O_2 = 1 : 1) for 5 minutes and then rinsed in deionized water for 10 minutes.

The scanning electron microscope (SEM) image of the CYTOP grating in Figure 6.3 shows the uniform 350 nm-wide tracks with very straight side walls. Tracks with smaller width can also be easily fabricated using NIL. We found that the imprinted CYTOP gratings of such quality performed extremely well, and that 350nm track width was adequate for physically confining and guiding the motion of microtubules.

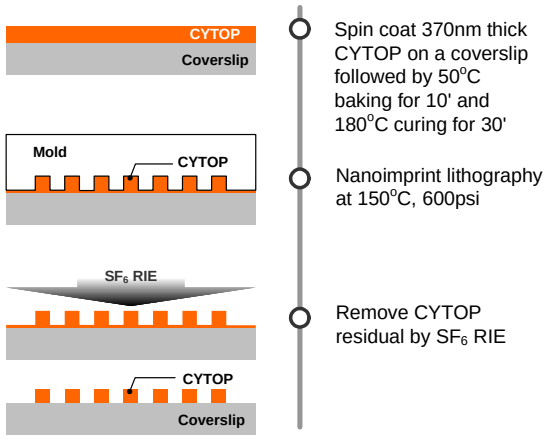

(a)

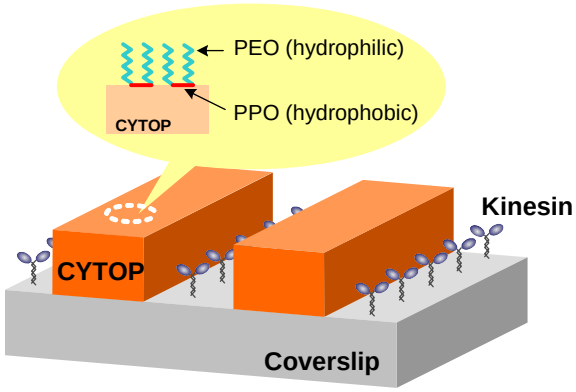

(b)

Figure 6.2 (a) Process flow of creating CYTOP nanotracks by NIL. (b) Schematic of Pluronic treatment of CYTOP surface to prevent adsorption of kinesin proteins on track barriers.

CYTOP has previously been shown to significantly reduce nonspecific binding of certain types of proteins (such as BSA) at low concentration (< 1μg/ml).[12] Nevertheless, we found that untreated CYTOP surfaces were not effective in preventing the kinesin binding that leads to undesirable motility on the surface of the grating. This was partly due to the much higher kinesin concentration (1.4 μM) we used in the experiment. To

solve this problem, we chemically treated the hydrophobic CYTOP surfaces to further reduce protein adsorption so that kinesins only selectively immobilize on the exposed glass surface. We used Pluronic® F-108 (PEO129-PPO56-PEO129 triblock copolymer) to coat the CYTOP surface, where PPO stands for poly(propylene oxide). The hydrophobic PPO domains bind with high affinity on the hydrophobic CYTOP surface while leaving the hydrophilic PEO domain extending out into the aqueous environment in the assay experiment (Fig. 2b). PEO is known to have protein repelling properties. After the Pluronic treatment, CYTOP surfaces can effectively suppress the binding of kinesin motors. We found that the Pluronic treatment works well on the as-deposited and imprinted CYTOP surface, but the dry etching process necessary for removing the residual CYTOP layer after NIL unavoidably degrade the hydrophobicity of the imprinted CYTOP surface. Typically in NIL oxygen plasma RIE is used to remove the residual layers after nanoimprint.[13] But O_2 plasma etching turns CYTOP surface hydrophilic, which significantly hinders the Pluronic treatment. We found that baking at an elevated temperature can help to partially recover the hydrophobicity of etched CYTOP surface. However, since a temperature over the T_g of CYTOP is necessary to obtain sufficient hydrophobicity, such baking temperature can cause reflow of CYTOP material or even destroy the imprinted CYTOP nanostructures.

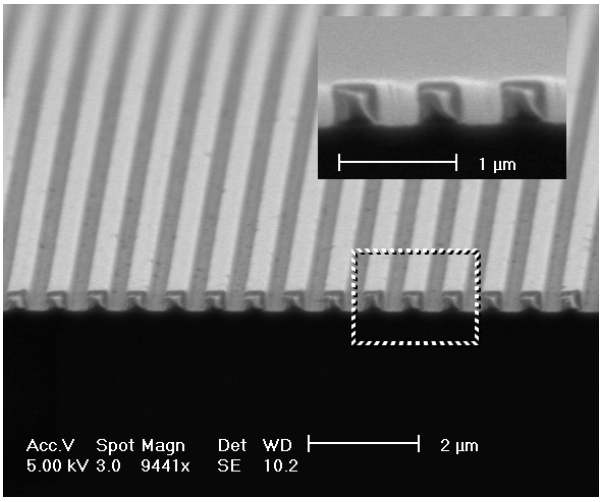

Figure 6.3 SEM image of nanoimprinted CYTOP grating.

To overcome this problem, we replaced the oxygen RIE with a sulphur hexafluoride (SF_6) RIE process. It was reported previously that the surface fluorination by SF_6 plasma can significantly enhance the hydrophobicity of certain polymers, such as polyurethane, silicone and poly(tetrafluoroethylene) (PTFE).[14] The phenomenon of hydrophobicity enhancement was also observed in our experiment on the SF_6 RIE etched CYTOP surface. Figure 6.4 compares the results of water contact angle measurements performed on different RIE etched and/or chemically treated CYTOP. Clearly Oxygen RIE reduces the hydrophobicity of CYTOP, and baking (120^oC) can partially recover the hydrophobicity. In contrast, SF_6 RIE actually improves the contact angle of CYTOP surfaces. In addition, the MT motility assay showed that the etching process does not affect the binding of kinesin to glass surfaces as compared with the samples cleaned by our standard process.

Based on these observations, we conclude that using CYTOP as track barriers, and employing SF_6 RIE to remove CYTOP residuals to expose glass surface for protein binding is an effective combination to achieve high contrast in kinesin binding.

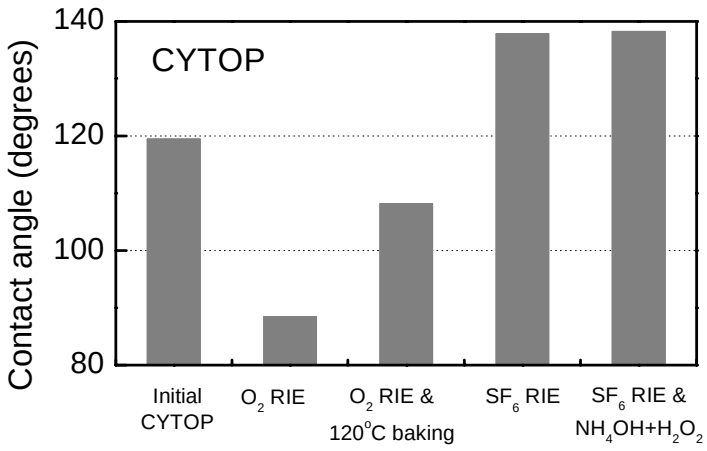

Figure 6.4 Water contact angle measurements on CYTOP substrates etched under different plasmas etching conditions and/or treated with different chemicals.

6.3 Guided microtubule gliding assay

We performed microtubule motility assays that were evaluated by fluorescent microscopy. Flow chambers were constructed from microscope slides and CYTOP nanotracks sample separated by 100 μm thick spacers. Samples were observed with an inverted fluorescence microscope (ZEISS Axiovert 200, 40x/ 1.3 NA Plan-Neofluar objective) and images were recorded with a digital CCD camera (**Orca II, Hamamatsu, Japan**). The statistical results of MT density obtained on microtubule gliding assay in the

presence of ATP shown in Figure 6.5 agree with our expectations. Pluronic treatment works very effectively on SF_6 RIE etched CYTOP samples and significantly reduces the binding of kinesin and hence the density of microtubules. The result indicates that the PEO coated CYTOP surface provides almost no kinesin adsorption, and therefore no microtubule gliding on it. Besides SF_6 RIE, chemical treatment in ammonia hydrogen peroxide mixtures was applied for 5 minutes and was observed to improve kinesin binding on glass surface. The reason of the improvement is not entirely clear at this moment. Further work is currently underway to understand the effect of chemical treatment on both glass and CYTOP surface. Figure 6.5(c) summarizes these results: SF_6 RIE enhances the Pluronic treatment and produces 100% contrast of kinesin patterning between glass and CYTOP surfaces. Because hydrophilic PEO has protein repelling characteristic, the experimental approach developed here can potentially be applied for patterning other protein molecules.

In our experiments we used a bacterially expressed kinesin motor, NKHK560cys. This motor consists of the head of *Neurospora crassa* kinesin (amino sequence to 433) and neck and stalk of *Homo sapiens* kinesin (amino sequence from 430 to 560) and a reactive cysteine at C-terminal end.[15] The NKHK560cys gene was ligated into the pT77 plasmid and transformed to Escherichia Coli BL21 cell. Cells were incubated in TPM medium

with 50μM ampicillin at 37°C. Expression was induced by adding 0.1 mM IPTG at a cell density corresponding to an OD of 0.6-0.8 and continued over night at 22°C. Cells were centrifuged and re-suspended in lysis buffer containing protease inhibitors, DNAse and lysozyme followed by sonification. The supernatant of this was loaded on SPFF ion exchanger (SP Fast Flow, **Amersham Biosciences, Piscataway, NJ, USA**) and kinesin was eluted by a step gradient to protocol.

Tubulin and TMR-labelled tubulin were obtained by standard procedures (see for example, Weingarten et. al., 1974: Hyman et al., 1991).[16] Briefly, tubulin was purified from cow brain by three cycles of microtubule polymerization and depolymerization followed by phosphocellulose ion exchange chromatography (P11, Whatman, UK) to eliminate microtubule associate protein. Tubulin was labeled with TMR (5-6carboxytetramethylrhodamine (**Molecular probes, Eugene, OR, USA**) by reacting polymerized microtubules with a 20 folds excess of dye at room temperature for 30 minutes. Competent, labeled tubulin was purified from this mixture by repeated depolymerization and polymerization.

For experiments, microtubules were polymerized by incubating 2 mg/ml tubulin (app. equal ratios of TMR-labeled and unlabeled tubulin) 1mM GTP and 4 mM $MgCl_2$ in BRB80 buffer at 37°C for 20 minutes. Microtubules were stabilized by the addition of

10μM taxol **(Paclitaxel, Calbiochem, USA).**

Flow chambers were constructed from microscope slides and CYTOP nanotracks sample separated by 100 μm spacers. The chambers were pretreated with 100 μl of a 2mg/ml aqueous solution of Pluronic **(Pluronic® F108 Prill, BASF, NJ, USA)** and then washed with 200 μl de-ionized water followed by 100 μl BRB80 buffer. Protein loading procedure was identical to that for standard kinesin gliding assays: Chambers were loaded with kinesin (47 μg/ml casein and 1.4 μM kinesin in BRB80 buffer) and incubated for 5 minutes. Subsequently, microtubules in a BRB80 buffer containing ATP and oxygen scavenger system (4 μg/ml microtubules, 2mM $MgCl_2$, 10mM glucose, 100 μg/ml glucose oxidase, 80 μg /ml catalase, 10 mM DTT, 1 mM ATP and 47 μg/ml casein) were loaded.

When the track width is reduced to nanoscale dimensions, PEO treatment of CYTOP surfaces is of vital importance. Without Pluronic treatment, CYTOP nanotracks have poor control over MT guiding. Figure 6.6 (a) shows a large number of microtubules gliding across nanotracks that were not chemically treated with Pluronic copolymer. Since the closely-spaced CYTOP grating surface is not kinesin free, a large number of microtubules glide randomly on the top surface of CYTOP barriers. Also, those traveling in the track frequently climb over the track barriers to either switch between different tracks or detach

and diffuse into the solution. Conversely, for the sample that has been treated with Pluronic F-108, high densities of microtubules are exclusively guided along the PEO-coated CYTOP grating shown in Figure 6.6 (b). In this image, the few microtubules oriented at an angle relative to the grating actually were not gliding on the surface but on their way diffusing onto surface searching for available kinesin proteins to bind.

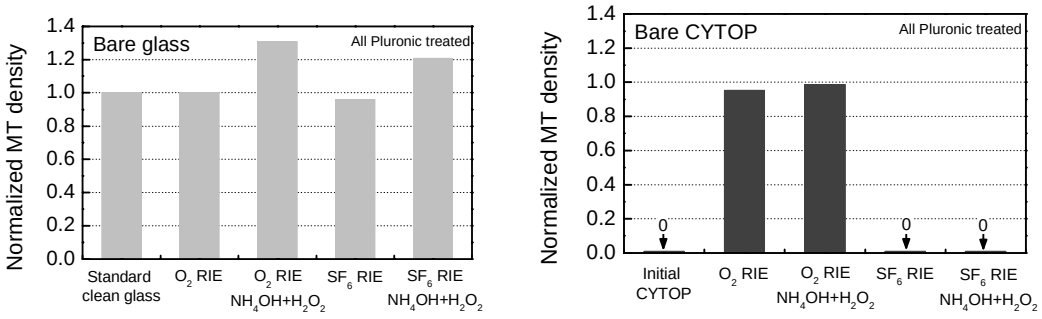

(a) (b)

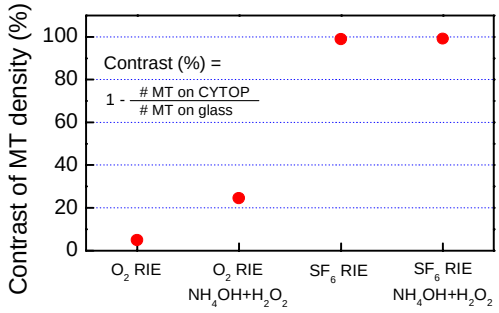

(c)

Figure 6.5 (a), (b) Effect of various plasma etching and chemical conditions on MT motility on both bare glass and CYTOP after Pluronic treatment. The MT density of each sample is normalized to that of standard process-cleaned glass; (c) The contrast of MT density between CYTOP and glass surfaces. The contrast is defined by 1- (number of MTs on CYTOP)/(number of MTs on glass).

Because of the physical confinement and chemical treatment, microtubules can glide in nanoscale tracks for a long distance before they detach. To estimate the average length MTs can glide in nanotracks before detaching, we collected time-sequence data of microtubule bindings on CYTOP grating after MTs were loaded (time = 0), which can be used to determine the dissociation rate of microtubules from the nanotracks. The number of microtubules gliding on the CYTOP nanotracks is plotted as a function of time in Figure 6.7. For each data point, the numbers of MTs were retrieved from the fluorescent images obtained from four different areas of 160μm×160μm in size. Since almost 100% of microtubules are guided in the nanotracks we conclude that there is little kinesin available on the PEO-coated CYTOP surface to support microtubule motility.

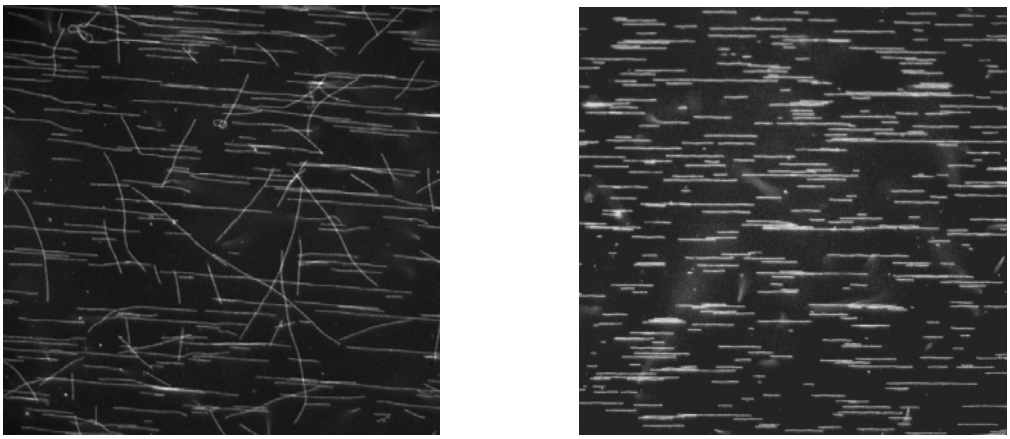

(a) (b)

Figure 6.6 The influence of Pluronic treatment on guiding microtubule becomes significant for CYTOP nanotracks. Gliding assays were performed on the CYTOP grating without (a) and with (b) Pluronic treatment. Each image is 160μm×160μm in size.

A simple MT binding kinetics model was developed to estimate the dissociation rate, which can be used to infer the average distance that microtubules can travel before they detach from the nanotracks. Detailed analysis can be found in the Appendix C. We first confirmed that, under our experimental conditions, the microtubule binding rate to the kinesin coated surface is much smaller than the diffusive flux, and therefore the diffusion process can be neglected when considering the MT surface binding kinetics. Under this condition, the transient MT concentration on a kinesin coated surface, *Ms*, can be shown to have a simple form:

$$Ms(t) = \frac{k_{\text{on}}}{k_{\text{off}}} M_b(1 - e^{-k_{\text{off}} \cdot t}),$$

where k_{on} and k_{off} are binding and dissociation rate constants, respectively, and M_{b}, is the constant concentration of freely diffusing MTs in the buffer solution. This equation is used in fitting the experimental data presented in Fig. 7 to obtain the MT dissociation rate. The fitting curve yields $1/(k_{\text{off}})$ to be ~ 21 minutes. Since the average MT gliding speed is ~ 2μm/sec, this implies that MTs translocate within the nanotracks an average distance of about 2.5 mm before detaching from the surface. In comparison, the average run-length of MTs traveling in microscale tracks defined by photoresist barriers was only a few tens of μm.[9] The 100-fold increase highlights the effectiveness of our method of combining nanoscale physical confinement with highly selectively patterning of kinesin within the

CYTOP channels. The long average distance of translocation of microtubules achieved in this study has important implications for the development of biomolecular motor-based nanotechnology, because the combined speed and travel distance make it now possible to transport target molecules over significant distances and overcome the normal diffusive motion.

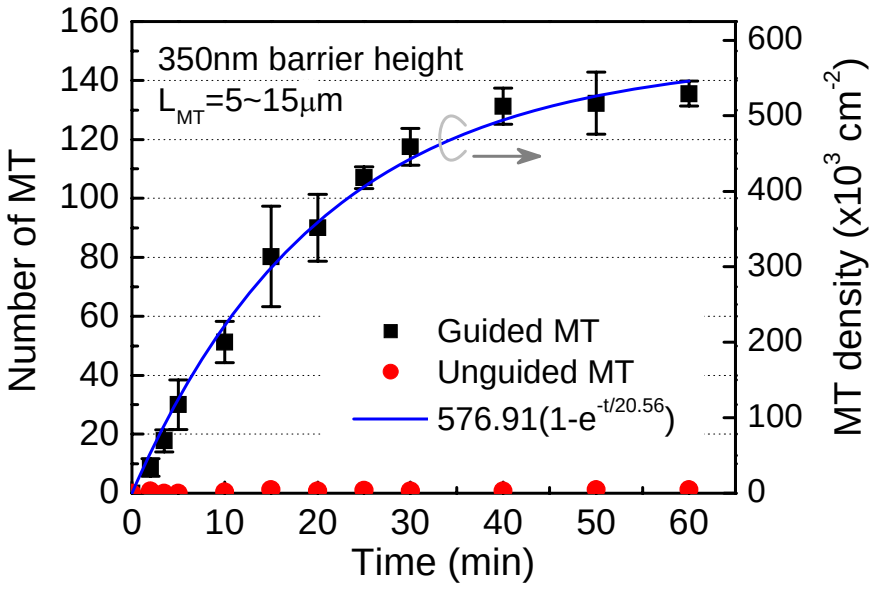

Figure 6.7 Time-sequence data of MT binding on the kinesin-covered nanotracks.

6.4 Conclusion

In conclusion, highly efficient guiding of MT transport propelled by immobilized kinesin motor molecules has been achieved in PEO coated polymer nanotracks on a glass substrate. This technique significantly improves both the resolution and the contrast of

motor protein patterning and physical confinement for guided MT transport. With this technology, we can apply CYTOP nanotracks to a variety of device applications. For example, CYTOP nanotracks can be integrated to microscale fluidic channels [17] to construct a hybrid micro-/nanoscale system with useful functionalities. The integration makes it possible to precisely locate and efficiently utilize nanoscale motor proteins to achieve more complex functions, including conveyance of molecules between different chemical reservoirs, or sorting and separation of specific molecules from chemical flow streams. Based on the versatility of nanoimprinting, the configuration of CYTOP nanotracks can be custom-designed to guide single microtubule transport along complex paths. The technology may pave the way to novel nanosystems for single molecule manipulation or detection that are powered by biomolecular motors.

REFERENCES

[1] R. D. Vale, T. S. Reese and M. P. Sheetz, *Cell* **1985**, 42, 39-50.

[2] N. Hirokawa, *Science* **1998**, 79, 519-526.

[3] H. Hess and V. Vogel, *Review in Molecular Biotechnology* **2001**, 82, 67-85.

[4] J. D. Hoff, L. J Cheng, E. Meyhöfer, L. J. Guo and A. J. Hunt, *Nano Letters* **2004**, 4, 953-857.

[5] H. Hess, J. Clemmens, D. Qin, J. Howard and V. Vogel, *Nano Letters* **2001**, 1, 235-239.

[6] Y.Hiratsuka, T. Tada, K. Oiwa, T. Kanayama and T. Q. Uyeda, *Biophysics J.* **2001**, 81, 1555-1561.

[7] S. G. Moorjani, L. Jia, T. N. Jacksonand W. O. Hancock, *Nano Letters* **2003**, 5, 633-637.

[8] J. Clemmens, H. Hess, R. Lipscomb, Y. Hanein, K. Bőhringer, C. M. Matzke, G. D. Bachand, B. C. Bunker and V. Vogel, *Langmuir* **2003**, 19, 10967-10974.

[9] J.Clemmens, H. Hess, J. Howard and V. Vogel, *Langmuir* **2003**, 19, 1738-1744.

[10] J. R. Dennis, J. Howard and V. Vogel, *Nanotechnology* **1999**, 10, 232-236.

[11] S.Y. Chou, P. R. Krauss, W. Zhang, L.J. Guo and L. Zhuang, *J. Vac. Sci. Technol. B.* **1997**, 15, 2897-2904.

[12] C.-S Lee, S. -H. Lee, S.-S. Park, Y.-K. Kim and P.-G. Kim, *Biosensors & Bioelectronics* **2003**, 18, 437-444.

[13] L. J. Guo, *J. Phys. D: Appl. Phys.* **2004**, 37, 123-141.

[14] E. C. Rangel, W. C. A. Bento, M. E. Kayama, W. H. Schreiner, and N. C. Cruz, *Surface and Interface Analysis* **2003**, 35, 179-183.

[15] (a) T. Funatsu, Y. Harada, H. Higuchi, M. Tokunaga, K. Saito, Y. Ishii, R. D. Vale and T. Yanagida, *Biophisical Chemistry* **1997** 68, 63-72; (b) A. Kallipolitou, D. Deluca, U. Majdic, S. Lakamper, R. Cross, E. Meyhofer, L. Moroder, M. Schliwa, and G. Woehlke, *EMBO J.* **2001** 20:6226–6235; (c) S. Lakämper, A. Kallipolitou, G. Woehlke, M. Schliwa and E. Meyhöfer, *Biophysical Journal* **2003** 84, 1833-1843.

[16] (a) A. Hyman, D. Drechsel, D. Kellog, S. Salser, K. Sawin, P. Steffen, L. Wordeman, and T. Mitchison, *Methods of Enzymology* (R.B. Vallee ed.) **1991** 196, 478-485; (b) D. Weingarten, M. M. Suter, D. R. Littmann, and M. W. Kirchner, *Biochemistry* **1974** 13, 5529-5537.

[17] L.-J. Cheng, H. Nanjundaswamy, E. Meyhöfer and L. J. Guo, *Conference Digest: EIPBN* **2004**, 411-412.

Chapter 7

Conclusion and Outlook

7.1 Conclusion

In summary, this work has focused on the investigation of ion transport phenomena in nanochannels induced by electrostatic interaction and the development of nanofluidic devices with well-defined surface charge to perform the control of ion flow. Although nanofluidic devices share common physicochemistry with ion-exchange membranes, nanochannels' precise-defined geometry and surface charge distribution allows us to perform well-controlled species transport and to integrate with microfluidic device on a large scale. Through experimental observations and theoretical calculation, this thesis aimed to advance our understanding of the ion transport behavior in precisely fabricated nanochannels.

At low ion concentrations, the surface charge on nanochannels has longer range of electrostatic interactions with ions; hence, it affects the ion concentration and ion

transport behavior in nanochannels. The surface-charge governed ion transport was substantiated by measuring the ion conductance in sub 20 nm thick nanochannels fabricated by standard semiconductor processes. The measurement results match the theoretical calculation and enable us to estimate surface charge densities and the nanochannel geometry.

Investigating asymmetric ion transport behavior in nanochannels is one of the focuses in the thesis. It was observed that the homogeneous silica nanochannel with ion concentration gradient can produce asymmetric ion current. This is because that the channel surface charges at the two channel ends have asymmetric electrostatic impact on the ion concentrations in the nanochannel due to the different bath concentrations. Depending on the polarity of the applied electric field, the uneven ion flow from the two ends can result in accumulation or depletion of ions in the nanochannel and therefore increase or decrease the ionic conductance. The effect has been elucidated by calculating the ion concentration and potential profiles in the device. A unified model was developed to qualitatively explain this kind of ion rectification phenomenon. It suggests that as long as an imbalance of cation-anion ratios are established at the two channel ends by any means, the nanofluidic device will exhibit rectification effect. For example, conical nanopores use asymmetric geometry to produce asymmetric electrostatic impact on the

ions at the two channel ends. Nanofluidic diodes utilize the asymmetric surface charge polarity to achieve the same effect.

The nanochannel with heterogeneous surface charge has been demonstrated to have nonlinear ion transport characteristics. To create such function, we developed the technology to precisely define the surface charge polarity in nanochannels by applying different solid oxide materials in the fabrication of nanochannels. Because each kind of solid oxide has its own distinct pI, by patterning the carefully selected solid oxide material to build nanochannels by means of standard photolithography, we can obtain well-defined, combined positively and negatively charged surfaces in single nanochannels. Our devices use Al_2O_3 and SiO_2 to produce the positive and the negative surface charge, respectively in heterogeneous nanochannels and benefit from their robustness and the ease of processing.

Several nonlinear ion transport behaviors were observed in the heterogeneous nanochannels. When a device has opposite surface charge polarity in the nanochannel with respect to that outside on the bath side-walls, a nonlinear transport effect at low ion concentrations was observed due to the parasitic diodes located at the channel entrances which were named nanofluidic access diode. The access diodes at the two channel

entrances connect back-to-back and can lead to current saturation under high voltage biases. The effect of the bath surface charge is a 2-dimensional effect and has not been treated before. By theoretical calculation, it is found the ion transport is significantly influenced by the polarity of the surface charge on the bath-side-walls. The result implies that the physics of ion transport in nanofluidic devices cannot be singled out from the influence of the nano-/microfluidic interface.

By defining the heterogeneous oxide surface on the right positions in a nanochannel, we can produce nanofluidic diode and other more sophisticated devices. The nanofluidic diode consisting of Al_2O_3 surface on one-half of the channel and SiO_2 surface on the other half displays very high rectifying factor at a certain range of bath concentrations. The trend of the ion conductance changing with the bath concentrations agrees with the theoretical calculation. Similar to bipolar membranes, the nanofluidic diode may find applications in chemical separation and flow control in microscale integrated systems, such as lab-on-a-chip devices.

Apart from the electrostatic interaction with charged species, nanochannels possess steric confinement to big molecules. By taking the advantage of the physical restriction, we can direct their movement. We demonstrated an active molecule transport platform by

using kinesin microtubule system and 300 nm size open nanochannels. With the energy provided by the hydrolysis of ATP, the kinesin motor proteins selectively immobilized in opened nanochannels propel microtubules along the direction of the nanochannels. Due to the physical confinement of nanochannel, microtubule can glide over a long distance without detaching from the channel surface. The device has implications in chemical delivery or molecule concentration.

7.2 Outlook

In this work, we focused on the ion transport behavior in nanochannels based on electrostatic interaction between charged surfaces and ions. The results of study can also be applied to the transport of charged molecules that is of more interest in the applications of chemical delivery, molecular detection and separation. However, more in-depth transport behaviors of molecules in nanochannels need to be investigated because apart from electrostatic effect studied in this thesis there are steric interactions or chemical reactions between molecules and chemically modified channel surface. The interaction can reduce the diffusivity of molecules inside nanochannels and results in so-called hindered transport. Large molecules with respect to the channel size or the molecules with high affinity to the channel surfaces get more restriction and have lower

diffusivity. The phenomena can be implemented for molecule sieving and chromatography. Some of these applications have been carried out in gel or membranes systems in the past. However, since nanofluidic channels fabricated by semiconductor process methods have well defined geometry and are amenable to integration and scaling, these applications can be implemented in a small scale and integrated with other devices of different functionalities. The development of the functional nanofluidic devices will improve the capabilities of the current chemical or biological analysis technologies.

Appendices

Appendix A: Debye length

We consider a simple fully dissociated symmetrical salt in solutions for those the numbers of positive and negative ions are equal, i.e. $z_+ = -z_- = z$. At equilibrium, the concentration of ions has the Boltzmann distribution

$$c_\pm = c_b\, e^{\mp zF\phi/RT} \tag{A.1}$$

where the concentration far from the surface $c \to c_b$ as potential $\psi \to 0$. The charge density from $\rho_e = F\,\Sigma z_i c_i$ is therefore

$$\begin{aligned} \rho_e &= zFc_b\left(e^{-zF\psi/RT} - e^{zF\psi/RT}\right) \\ &= -2Fzc_b \sinh\left(\frac{zF\psi}{RT}\right) \end{aligned} \tag{A.2}$$

Poisson's equation $d^2\psi/dx^2 = \rho_e/\epsilon_0\epsilon_r$ becomes

$$\frac{d^2\psi}{dx^2} = \frac{2zFc_b}{\epsilon_0\epsilon_r} \sinh\left(\frac{zF\psi}{RT}\right) \tag{A.3}$$

With Debye-Hückel approximation, i.e. for small potentials $zF\psi \ll RT$, we can expand $\sinh(zF\psi/RT)$ with the result

$$\frac{d^2\psi}{dx^2} = \frac{2z^2F^2c_b}{\epsilon_0\epsilon_r RT}\,\psi \tag{A.4}$$

Integrating Eq. (2.13) subject to the conditions that $\psi = \psi_w$ at $x = 0$ and $\psi = 0$, and $d\psi/dx = 0$ as $x \to \infty$ gives

$$\psi = \psi_w e^{-x/\lambda_D} \tag{A.5}$$

where λ_D is Debye length and is given by

$$\lambda_D = \sqrt{\frac{\epsilon_0 \epsilon_r RT}{2F^2 z^2 c_b}} \tag{A.6}$$

The Debye length is seen to be the 1/*e* decay distance for the potential and electric field at low potentials. Close to the charged surface where the value of the potential is relatively high and the Debye-Hückel approximation inapplicable, the potential decreases faster than the exponential fall-off indicated by Eq. (A.5).

Appendix B: Electroosmotic flow velocity and zeta-potential

The velocity profile of electroosmotic flow can be derived from a simplified form of Navier-Stokes equations in which the flow is presumed steady:

$$\nabla p = \eta \nabla^2 \vec{v} + \rho_e \vec{E} \tag{B.1}$$

Here p is the pressure, v the stream velocity, E the electric field, and η and ρ_e are viscosity and net electric charge density, respectively. The nonlinear advective term from the Navier-Stokes equations is ignored because in virtually all electroosmotic flows, inertial forces are negligibly small compared to pressure and viscosity forces which means the Reynolds number $Re = \rho v d/\eta$ is much less than unity (ρ is the fluid mass density, and d the scale characterizing the velocity gradients). In the absence of pressure gradient, for any unidirectional flow with uniform electric field E_x, the momentum equation is reduced to

$$\eta \frac{\partial^2 v}{\partial y^2} = -\rho_e E_x \tag{B.2}$$

Substituting the electric charge density ρ_e with Poisson's equation $\epsilon_0 \epsilon_r (\partial^2 \psi / \partial y^2) = -\rho_e$, we obtain

$$\eta \frac{\partial^2 v}{\partial y^2} = \epsilon_0 \epsilon_r \frac{\partial^2 \psi}{\partial y^2} E_x \tag{B.3}$$

In the case of no slip flow, the velocity profile can be obtained by integrating equation (4.3) with the boundary conditions $v(y=0)=0$ and $\psi(y=0)=\zeta$:

$$v(y) = \frac{\epsilon_0 \epsilon_r}{\eta} \left(\psi(y) - \zeta\right) E_x \tag{B.4}$$

where ζ is the zeta-potential, the potential at the shear plate where velocity is zero. In the case of microchannel, the potential $\psi \to 0$ far from the wall and the velocity approaches

$$v = -\frac{\epsilon_0 \epsilon_r \, \zeta}{\eta} E_x \tag{B.5}$$

The factor $-\epsilon_0 \epsilon_r \, \zeta / \eta$ is known as the electroosmotic mobility, μ_{EO}.

Surface charge density

Because of the nature of electroneutrality at equilibrium, the charge density of the wall surface can be estimated by integrating the all mobile charges from the wall to the solution and substituting Poisson's equation:

$$\sigma_s = -\int_{wall}^{\infty} \rho_e \, dy = \epsilon_0 \epsilon_r \left(\frac{\partial \psi}{\partial y}\right)_{wall} \tag{B.6}$$

At equilibrium, the distribution of the mobile ions follow the Boltzmann distribution, $n^{\pm} = n_b \, e^{\mp q \, \psi / kT}$ for 1:1 electrolyte. Considering the net electric charge contributed by both cations and anions $\rho_e = q(n^+ - n^-)$, we have Poisson equation

$$\frac{d^2 \psi}{dy^2} = \frac{q \, n_b}{\epsilon_0 \epsilon_r} 2 \sinh\left(\frac{q \, \psi}{kT}\right) \tag{B.7}$$

To get the first derivative of potential in (4.6), we need to utilize the equation

$$\frac{d}{dy}\left(\frac{d\psi}{dy}\right)^2 = 2\,\frac{d\psi}{dy}\cdot\frac{d^2\psi}{d^2y} \tag{B.8}$$

By substituting equation (4.7) to (4.8) and integrating (4.8) from the wall (or outer Helmholtz layer to be more precise) with the boundary conditions $(d\psi/dy)_{y\to\infty} = 0$ and $\psi(y = wall) = \psi_s$, we obtain

$$\left(\frac{d\psi}{dy}\right)_{wall} = \sqrt{\frac{8kTn_b}{\epsilon_0\epsilon_r}}\sinh\left(\frac{q\,\psi_s}{2kT}\right) \tag{B.9}$$

Plug equation (4.9) into (4.6) and the surface charge density leads to

$$\sigma_s = \sqrt{8\epsilon_0\epsilon_r kT\,n_b}\,\sinh\left(\frac{q\,\psi_s}{2kT}\right) \tag{B.10}$$

It should be emphasized that surface potential ψ_s here is the potential at the outer Helmholtz layer while ζ-potential in equation (4.5) is the potential at which the electroosmotic flow is zero. Because these two boundaries are close, for convenience the ψ_s in equation (4.10) is replaced by ζ-potential, yielding the effective surface charge density

$$\sigma_{\text{eff}} = \sqrt{8\epsilon_0\epsilon_r kT\,n_b}\,\sinh\left(\frac{q\,\zeta}{2kT}\right) \tag{B.11}$$

Equation (4.11) will be used in our experiment to estimate surface charge densities by measuring ζ-potential through electroosmotic flow.

Appendix C: Derivation of kinesin binding kinetics

In deriving the kinesin binding kinetics, we use the fact that surface density of kinesin is very high compared to MT concentration close to the surface, and therefore can be taken as a constant. The binding rate of a single MT to the kinesin coated surface, *Ms*, is given by:

$$\frac{d}{dt}Ms(t) = k_{\text{on}}\, M(0,t) - k_{\text{off}}\, Ms(t) \tag{C.12}$$

where k_{on} and k_{off} are binding and dissociation rate constants, respectively, and *M*(0,t) the volume concentration of free MTs right next to the binding surface at time *t*. The binding surface is the kinesin-coated surface and defined as x=0 (see Figure C.1). Considering the diffusion of MTs from the solution to the kinesin binding sites with a diffusivity *D*, we can apply two boundary conditions for Fick's diffusion equation, $\dot{M}(x,t) = D \cdot M"(x,t)$. First, the diffusion flux equals to the binding rate at the surface, i.e.

$$D\frac{\partial}{\partial x}M(x,t)\bigg|_{x=0} = \frac{d}{dt}Ms(t) \tag{C.13}$$

Second, the concentration of microtubule outside the unstirred layer (a volume within a distance δ from the surface) equals to M_{b}, a constant microtubule concentration in buffer (Figure C.1):

$$M(\delta, t) = M_b \tag{C.14}$$

Since the amount of MTs in the buffer solution (with a concentration of $M_b \sim 1.5\times10^{11}$ cm^{-3})[1] is much higher than the amount diffusing to and attached to the surface, we neglect the depletion of the microtubules in the buffer. To simplify the problem, we used an approximation that the microtubule concentration decreases linearly toward the surface across the unstirred layer (as shown in Figure C.1). The boundary condition can then be recast as

$$\frac{d}{dt}Ms(t) = D\frac{\partial}{\partial x}M(x,t)\bigg|_{x=0} = D\,\frac{M_b - M(0,t)}{\delta} \tag{C.15}$$

or

$$M(0,t) = M_b - \frac{\delta}{D}\,\frac{d}{dt}Ms(t) \tag{C.16}$$

Substituting equation 5 into equation 1, we can solve for *Ms*(t)

$$Ms(t) = \frac{k_{\text{on}}}{k_{\text{off}}}M_b(1 - e^{-k_{\text{off}}\cdot t/(1+Da)}) \tag{C.17}$$

where $Da = k_{\text{on}}\delta/D$, is a dimensionless parameter, known as the second Damköhler number. It represents the ratio of surface reaction rate to the bulk diffusion rate. Prior to extracting k_{off} from the experimental data, it is appropriate to evaluate the Damköhler number and find out which process is the rate-limiting one. Typically δ, which is in the

same order of $\sqrt{D \cdot t}$, is about 10 μm. The diffusion coefficient *D* of MT is about 2×10^{-9} cm^2/s.[2] k_{on} can be estimated from the slope of the binding curve at $t = 0$, i.e. $M_b(1/k_{on} + \delta/D)^{-1}$. The slope, about 467.7$cm^{-2}\cdot s^{-1}$ obtained from the fitted curve, gives $k_{on} = 3.1\times10^{-9}$ cm/s. Substituting these values into the Damkőhler number yields $Da = 1.6\times10^{-3}$, *i.e.* $Da << 1$. This means that the microtubule binding rate is much smaller than the diffusion flux. In other word, the diffusion process can be neglected when considering the MT surface binding kinetics. Therefore, the binding kinetics can be reduced to a simple form:

$$Ms(t) = \frac{k_{on}}{k_{off}} M_b(1 - e^{-k_{off}\cdot t}) \tag{C.18}$$

This is the equation used in fitting the data presented in Figure C.1 to obtain the MT dissociate rate.

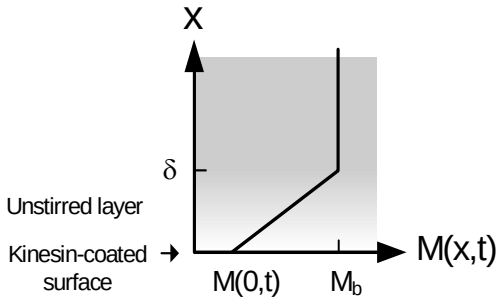

Figure C.1 Schematic plot of MT concentration in a flow cell. The kinesin are immobilized on glass surface at x=0. Due to high concentration of MT in the bulk solution, MTs in the flow cell is assumed to be a constant, and no depletion of MTs occurs because of the binding of MTs to kinesins on the glass surface.

REFERENCES

[1] Each microtubule is comprised of 13 linear protofilaments. Within each protofilament, the dimeric tubulin subunits repeat every 8 nm. Thus the concentration of microtubule (10μm long in average) polymerized from 4 μM (or 2.4×10^{15} cm^{-3}) tubulin is 2.4×10^{15} $cm^{-3}/(13\times10\mu m/8nm) \approx 1.5\times10^{11}$ cm^{-3}.

[2] R. Stracke, K. J. Bohm, L. Wollweber, J. A. Tuszynski and E. Unger *Biochem. Biophys. Res. Commun*. **2002**, 293, 602-609.